# Charge and spin injection from GaAs into metallic and magnetic layers.

Vu Duong

Thèse présentée pour obtenir le grade de

**DOCTEUR DE L'ECOLE POLYTECHNIQUE**

Spécialité : Physique

Par

**Duong VU**

# Injection de charge et de spin de GaAs vers des couches métalliques et magnétiques.

Soutenance prévue le 15 juillet 2010 devant le jury composé de:

| | | |
|---|---|---|
| Dr. Bernhard Urbaszek | INSA de Toulouse | Rapporteur |
| Prof. Philippe Dumas | Université de Marseille | Rapporteur |
| Prof. Jean-Eric Wegrowe | Ecole Polytechnique-LSI | Examinateur |
| Dr. Daniel Paget | Ecole Polytechnique-PMC | Directeur |
| Dr. Alistair Rowe | Ecole Polytechnique-PMC | Co Directeur |

Thesis presented for the degree of

**DOCTEUR DE L'ECOLE POLYTECHNIQUE**

Speciality : Physics

by

**Duong VU**

# Charge and spin injection from GaAs into metallic and magnetic layers.

Defense scheduled on July 15, 2010 in front of a jury composed of

| | | |
|---|---|---|
| Dr. Bernhard Urbaszek | INSA de Toulouse | Referee |
| Prof. Philippe Dumas | Université de Marseille | Referee |
| Prof. Jean-Eric Wegrowe | Ecole Polytechnique-LSI | Examiner |
| Dr. Daniel Paget | Ecole Polytechnique-PMC | Supervisor |
| Dr. Alistair Rowe | Ecole Polytechnique-PMC | Co Supervisor |

**Résumé**

Ce travail expérimental et théorique porte sur l'injection tunnel de photoélectrons à partir de GaAs vers des surfaces métalliques et de spin vers des surfaces magnétiques. On y présente la première mise en évidence de la dépendance en spin du courant tunnel vers une surface magnétique. Ce travail comporte deux parties distinctes :

***1ere partie :***

Cette partie est consacrée à l'étude de l'injection de charge et de spin de photoélectrons à partir de microleviers de GaAs (sans pointe) sous pompage optique, vers des surfaces nonmagnétiques d'or et magnétiques de cobalt. La dépendance du courant injecté vers une surface d'or en fonction de la tension appliquée sur le levier et de la distance levier/surface métallique est en accord avec les prédictions d'un modèle original.

A l'aide d'une cellule de Pockels, le même montage est utilisé pour moduler la polarisation de spin des électrons tunnel et pour étudier la dépendance en spin du courant tunnel dans des couches de cobalt. Ce travail conduit à la première mise en évidence de la dépendance en spin de l'effet tunnel de photoélectrons vers une couche magnétique. Le retournement de la polarisation de spin des électrons tunnel par rapport à l'aimantation de la couche magnétique induit une variation de 6% du courant tunnel, alors que la valeur maximale observée pour une couche non magnétique est de l'ordre de 0.1%. On observe une diminution de ce signal en fonction de la tension appliquée qui est attribuée à la diminution de la vitesse de recombinaison de surface. Les résultats sont en accord quantitatif avec les prédictions théoriques.

***2e partie :***

Cette partie regroupe deux études distinctes du transport de charge et de spin faisant appel à l'imagerie de luminescence polarisée pour caractériser les propriétés de spin. Cette technique nouvelle d'imagerie a été mise au point dans le cadre de ce travail.

La première étude analyse les propriétés de spin de pointes de GaAs qui pourraient être utilisées ultérieurement pour l'imagerie du nanomagnétisme, dans le but de prédire le taux de polarisation de spin des électrons injectés. En utilisant des mesures sur des couches planaires équivalentes et en modélisant la diffusion de charge et de spin dans la pointe, on montre que l'on peut s'attendre à obtenir des polarisations de spin atteignant 40%.

Par ailleurs, la microscopie de luminescence polarisée permet d'étudier le transport de charge et de spin dans des couches minces de GaAs, respectivement oxydées et passivées. On montre que la recombinaison de surface joue un rôle crucial pour la diffusion de charge et de spin, car la diminution de la vitesse de recombinaison de surface de $10^7$ cm/s à $10^3$ cm/s induite par la passivation fait passer les longueurs de diffusion de charge et de spin de 21 μm et 1.3 μm respectivement à 1.2 μm and 0.8 μm.

Mots-Clés: Spintronique, pompage optique dans GaAs, injection de charge et de spin, effet tunnel, cantilevers, diffusion de charge et de spin diffusion, recombinaison de surface, jonctions métal-isolant-semi/conducteur.

**Abstract**

This thesis describes experimental and theoretical work concerning photo-assisted tunnelling between optically pumped GaAs and metallic surfaces. In particular, the first evidence for the spin dependence of the tunnel photocurrent into a magnetic surface is presented. The thesis is made up of two separate parts:

**Part 1:**

Reports studies of charge and spin injection of photoelectrons from an optically pumped, tipless GaAs microcantilever into both (nonmagnetic) Gold and (magnetic) Cobalt surfaces. A new model, which is used to analyse the bias, tunnel distance and spin dependence of the tunnel photocurrent, correctly predicts the behaviour observed on the Gold surfaces.

With the addition of a Pockels' cell, the same experiment is used to modulate the spin polarisation of tunnelling electrons and to the spin dependence of photoelectron injection into Cobalt. A reversal of the relative spin polarisation of the photoelectrons to the magnetisation direction of the Cobalt results in a 6 % variation in the tunnel photocurrent. This compares with a value of 0.1 % observed on nonmagnetic Gold surfaces. A reduction in this variation with increasing applied bias is attributed to a reduction in the surface recombination velocity. An extension to the model developed for charge injection which accounts for the spin polarisation of the photoelectrons describes the experimental results well.

**Part 2:**

Reports studies on charge and spin transport in GaAs using an original polarised photoluminescence microscopy technique.

This technique is firstly applied to photoluminescence imaging in GaAs tips to be used in imaging studies of nanomagnetism, in order to estimate the expected electronic polarisations at the tip apex. In combination with studies on equivalent planar geometry samples and by numerically solving the charge and spin diffusion equations, polarisations approaching 40 % are predicted.

Independently, polarised luminescence microscopy is used to investigate charge and spin transport in planar oxidized and passivated thin films. Surface recombination is shown to play an important role in determining the effective charge and spin diffusion lengths. The effect of an increase in the surface recombination velocity between the passivated and oxidized sample from $10^3$ cm/s to $10^7$ cm/s reduces the charge and spin diffusion lengths from 21 μm and 1.3 μm, to 1.2 μm and 0.8 μm respectively.

Key-words: spintronics, optical pumping in GaAs, charge and spin injection, tunnel effect, cantilevers, charge and spin diffusion, surface recombination, metal-insulator-semiconductor junctions.

# Acknowledgement:

My first day working in the laboratory of Condensed Matter Physics was almost three years ago.

First of all, I would like to present my honour to have the opportunity of working with my supervisors Daniel Paget and Alistair Rowe. Whenever I have faced any difficulty in language, scientific knowledge or science study, they always stood by me and showed me the most efficient way to overcome.

To my colleagues in PMC, it is my pleasure to be a member of PMC team. I would like to thank François Ozanam, Michel Rosso and Jean-Pierre Boilot, who always attempt to give me the most comfortable working condition. Specially thank EPS group (Yves Lassailly, Jaques Peretti, Georges Lampel and the PhD students) with whom I had a chance to discuss and achieved a lot of precious scientific suggestions. One important part of my thesis was done with the help of ECM researchers (Hugo Jurca, Philippe Allongue and Fouad Maroun) who not only produced the equipments for my project but also provided me with lots of useful knowledge in the science of electrochemistry.

To my friends, I would love to express my appreciation to the technical groups (Julien, Denis, Didier), the administrative officers (Patrice Delaroque, Eve Brunswic …) and the mechanics group (Dominique Clément, Bernard Mathon …) for all of the hard work they did to help me during my thesis. They always showed me their enthusiasm and kind-hearted whenever I need a hand. And my PhD team-mates, they balanced my first abroad life time that had been expected to be very difficult. I will always recall the great moments that we shared together. Specially thank the captain Hugo and all members Aurélie, Filippo, Larbi, Magali, Matteo, Morgane, Nayely, Vincent, Xiaoxin … Another special souvenir is about my international office in which Mathis Plapp, Hugo Jurca as well as Florience Dercart generated a friendly green environment. Thanks you all, my friends.

To my co-operation groups, I would like to thank S. Bansropun of R&T group of Thales Corp., Palaiseau; Evelyn Gil of LASMEA, Clermont-Ferrand University for their work that assisted the progress of my studies.

I also want to show gratitude to my Vietnamese Prof. Nhung Tr. who kindly followed my studies since my graduation.

To my Chuoi, I am proud to be with them during my time in France.

Finally, to my family, my parents and my wife, they were not by my side geographically yet I have always felt their presence and I would love to thank for the important psychological support that they have given to me.

# Index

# Chapter 1: Introduction

This thesis describes experimental and modelling work aimed at experimentally proving that the tunnel photocurrent current from a thin, optically pumped GaAs plate or tip into a ferromagnetic surface depends on the relative spin orientation of the two sides of the tunnel junction. To our knowledge, despite being first proposed more than 20 years ago,[1] this has never been conclusively shown. This is in contrast with the inverse case; spin dependent electron tunnelling from a ferromagnet into a semiconductor, that was demonstrated by measuring the degree of circular polarisation of the luminescence emitted under excitation of GaAlAs by tunnelling electrons from a Ni ferromagnetic tip.[2,3] A tunnel current dependent spin polarisation as large as 50 % was measured. Similarly, electrical spin injection from ferromagnets into semiconductors has been studied both theoretically[4] and experimentally.[5]

Spin dependent tunnelling across solid junctions is also very well documented and, in the form of tunnelling magnetoresistance (TMR), has been proposed as the successor technology to GMR read heads.[6] Of more particular interest in the context of this thesis is that spin polarised electron tunnelling from magnetic tips has become the basis for the burgeoning field of spin polarised scanning tunnelling microscopy (SPSTM) and has been exploited to great effect in a number of stunning papers in which magnetic imaging at the atomic scale is reported.[7,8] Pierce[1] first described an alternative type of SPSTM based on optically pumped GaAs tips and foresaw two main advantages over the ferromagnetic tip method:

Independent investigation of topography and magnetism: In order to separate these two sources of tunnel current variation it is sufficient to rapidly modulate the spin polarisation of the tip since this does not change the part of the tunnel current related to the topography. In the case of ferromagnetic tips this must be done with a small coil close to the tip,[2] but modulation frequencies are limited because of the inductance of this coil and are not easily compatible with typical STM scan rates. Other techniques such as image subtraction

---

[1] *D.T. Pierce, Physica Scripta **38**, 291 (1988)*
[2] *S. F. Alvarado and P. Renaud, Phys. Rev. lett. **68**, 1387 (1992)*
[3] *S. F. Alvarado, Phys. Rev. Lett. **75**, 513 (1995)*
[4] *A. Fert and H. Jaffrès, Phys. Rev. B **64**, 184420 (2001)*
[5] *Y. Ohno, D. K. Young, B. Beschoten, F. Matsukura, H. Ohno, and D. D. Awschalom, Nature **402**, 790 (1999)*
[6] *M. N. Baibich, J. M. Broto, A.Fert, F. N. Vandau, F. Petroff, P. Etienne, G. Creuzet, A. Friederich, and J. Chazelas, Phys. Rev.Lett. **61**, 2472 (1988)*
[7] *M. Bode, Rep. Prog. Phys. **66**, 523 (2003)*
[8] *R. Wiesendanger, Rev. Mod. Phys. **81**, 1495 (2009)*

must be used to obtain magnetic information.[7] More recently an elegant but sample dependent technique has been developed that exploits known spin dependent/independent parts of the tip or sample density of states to separate topographic and magnetic information. In contrast the electronic spin polarisation in p-type GaAs is a non equilibrium phenomenon with typical spin lifetimes in the nanosecond range[9] and standard optical components (e.g. Pockels' cells) can be used to switch polarisations at frequencies in the $10^4$ Hz range. Separation of topographic and magnetic information point-by-point during acquisition is then possible.

Negligible tip-sample magnetic interaction: For typical focused optical excitation powers in the mW range, spin polarised photoelectron densities fall in the $10^{14}$ $cm^{-3}$ range, more than ten orders of magnitude smaller than the equivalent electron densities in metals. Thus the fringing fields are negligibly small compared to a ferromagnetic tip and tip/sample magnetic interactions are negligible. This is an important point for the imaging of soft magnetic materials in particular. Although this issue has recently been addressed via the use of anti-ferromagnetic tips,[7] only GaAs tip SPSTM offers a simultaneous solution to all the problems outlined here.

Throughout the 1990s several attempts were made by Dutch[10] and Japanese[11,12] groups to observe spin dependent tunnelling from GaAs tips into ferromagnets, but with little success. In particular, a relative spin orientation dependence of the tunnel current of several percent was observed not only on ferromagnetic surfaces, but also on non-magnetic surfaces such as Gold. The origin of this parasitic effect has been ascribed to the optical excitation geometry[13] and the experiments described in this thesis are conceived to avoid such effects. As described in Fig. 1.1, the Dutch group used excitation from the side of the tip while the Japanese investigators excite the tip across the semitransparent sample. These two configurations result in direct excitation of the tip apex. This poorly controlled geometry which has been found to induce a polarisation-dependent modulation of the electron concentration at the apex.[10] In the present work we have chosen to excite the tip in a

[9] *K. Zerrouati, F. Fabre, G. Bacquet, J. Bandet, J. Frandon, G. Lampel and D. Paget, Phys. Rev. B **37**, 1334 (1988)*
[10] *M.W.J. Prins, D. L. Abraham, and H. van Kempen, J. Magn. Magn. Mater. **121**, 109 (1993); Surf. Sci. **287/288**, 750 (1993); M. W. J. Prins, H. van Kempen, H. van Leuken, R. A. De Groot, W. van Roy and J. De Boeck, J. Phys. Condens. Matter **7**, 9447 (1995)*
[11] *Y. Suzuki et al., J. Mag. Mag. Mat. **198**, 540 (1999)*
[12] *W. Nabhan et al., Appl. Surf. Sci. **145**, 570 (1999)*
[13] *D. Paget, J. Peretti, A. Rowe, G. Lampel, B. Gérard, S. Bansropun, French patent # 05 05394 filed on the 27th May 2005 (Thales and Ecole Polytechnique)*

controlled way from the planar rear surface, and therefore to separate the zone of excitation, at the rear of the tip, from the zone of injection.

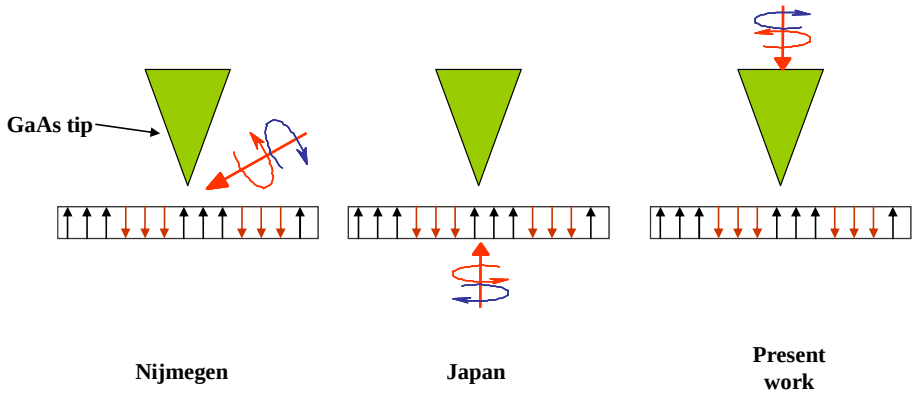


***Fig 1.1**: Injection configurations used by previous researchers, [10, 11, 12] compared with the one of the present work.*

In order to avoid direct excitation of the p-type tip, its height must be larger than the absorption length. Thus diffusion plays a key role for transferring the photoelectrons from the rear of the tip to the apex. Most of the results presented here therefore rely on the description of the evolution of electron concentration and spin polarisation under diffusion in the injector, taking account of surface recombination. The description of charge and spin diffusion is summarized in Appendix A and will be used throughout this work.

Another major challenge is the fabrication of the injectors which requires the development of a new clean room process. This has been undertaken by our collaborators at Thales R & T, the University of Clermont-Ferrand and IEMN Lille. Their efforts are summarized in this thesis. For the charge and spin injection experiments reported here, tipless GaAs cantilevers have been used since fabrication and interpretation of the results is simpler. GaAs tips on transparent GaInP cantilevers have also been fabricated and their spin dependent properties are investigated using luminescence microscopy.

The manuscript is organized as follows. Part I is dedicated to the description of charge and spin injection into metallic and magnetic surfaces from tipless cantilevers. This part contains the following chapters:

-Chapter 2: Theory of charge and spin injection by photo-assisted tunnelling

-Chapter 3: Description of the experimental setup, the procedure for spin-polarised injection and of the technology for injector fabrication

-Chapter 4: Charge injection into nonmagnetic gold surfaces

-Chapter 5: Charge and spin injection into (magnetic) cobalt surfaces

Part II of this thesis presents luminescence investigations (under circularly-polarised excitation) in which one measures the luminescence degree of circular polarisation $\mathcal{P}$ given by

$$\mathcal{P}=\frac{I_+ - I_-}{I_+ + I_-} = P_i \int_{tip} (n_+ - n_-) e^{-\alpha_l z} dv \,/\, \int_{tip} (n_+ + n_-) e^{-\alpha_l z} dv \qquad (1.1)$$

where $I_\pm$ is the intensity of the $\sigma^\pm$ polarised component of the luminescence, $\alpha_l$ is the absorption coefficient at the luminescence energy, $z$ is the direction of light excitation and $P_i$ = 0.5 is the initial polarisation which depends on the matrix elements for recombination. $\mathcal{P}$ is therefore related to the average of the electron spin polarisation over the measured area. Chapter 6 presents a luminescence microscopy investigation of GaAs tip injectors. Chapter 7 presents an investigation charge and spin transport by diffusion. Both chapters use a novel technique consisting of imaging the luminescence and its polarisation with a microscope objective.

It is hoped that the experimental results and models described herein will prove to be a stepping stone to successfully performing GaAs tip SPSTM.

# Chapter 2: Theoretical description of charge and spin injection

## *I. Introduction*

In the past, photoexcited scanning tunnelling microscopy (STM) studies have been conducted with the semiconductor material as the sample, but also more recently as the tip material.[14] Although the present system is a metal-insulator-semiconductor (MIS) structure for which the thickness of the interfacial layer is adjustable, the understanding of the photoinjection properties is still far from complete.

Some studies have been performed in STM configurations, with a limited theoretical discussion.[15] Other investigations have considered MIS silicon-based components of controlled insulator thickness, with an emphasis on forward,[16] or zero bias.[17] Perhaps the most detailed investigations of charge injection, both theoretical and experimental, were performed by the Nijmegen group who developed a model called below the Nijmegen model.[18,19,20] In this model, to be described in Sec. II below, the tunnel current spectra are interpreted considering both the characteristics of the space charge layer formed at the tip surface and of the tunnel barrier itself. The predictions are compared with results obtained for GaAs tips and gold or cobalt metallic samples. This model can account for a number of observed phenomena for a small tip bias, up to about 0.5 V.

The use of films excited from the rear brings two simplifications to the understanding of the results. Firstly, the injected photocurrent originates from electrons created in the semiconductor bulk after diffusion from the rear surface and, unlike the front surface excitation configuration,[21] does not directly depend on the width of the depletion layer. Secondly, the use of a film rather than a tip increases the contact surface. Although one could expect that there results inhomogeneities in the tunnel distance, it will be shown in Chapter 4 that after correction the metal-semiconductor interface can be considered as planar.

---

[14] *S. Grafström J. Appl. Phys.* ***91****, 1717 (2002)*
[15] *F. F. Fan, and A. Bard, J. Phys. Chem* ***1431****, 97 (1993)*
[16] *H. C. Card, Solid State Electronics* ***18****, 881 (1975)*
[17] *H. C. Card, Solid State Electronics* ***20****, 971 (1977)*
[18] *M. W. J. Prins, R. Jansen, R. H. M. Groeneveld, A. P. van Gelder and H. van Kempen, Phys. Rev. B* ***53****, 8090 (1996)*
[19] *M. W. J. Prins, R. Jansen, and H. van Kempen, Phys. Rev. B* ***53****, 8105 (1996)*
[20] *R. Jansen, M. W. J. Prins, and H. van Kempen, Phys. Rev. B* ***57****, 4033 (1998)*
[21] *W. G. Gärtner, Phys. Rev* ***116****, 84 (1959)*

It will be shown that the Nijmegen model cannot interpret our experimental results, obtained for a reverse bias up to 1.5V. The explanation is that this model does not consider surface recombination and its bias dependence.

## *II. Background*

### *II.1 Generalities*

I first recall a very general framework concerning charge and current distributions in a MIS structure under light excitation.

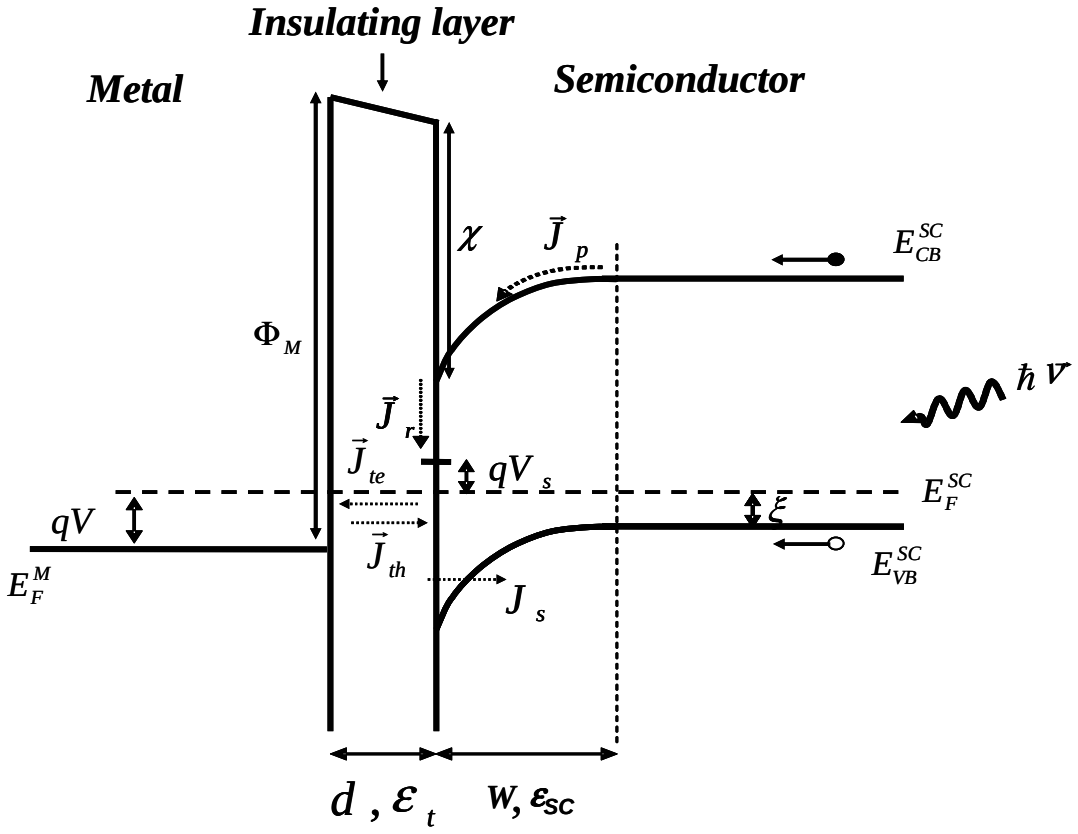


***Fig 2.1:*** *Metal-Insulator-Semiconductor structure. A positive bias (inverse) applied to the metal and a negative value of surface photovoltage $V_s$ is created by a flux of photons of energy $\hbar\nu$ .*

The metal-insulator semiconductor structure described in Fig. 2.1 is composed of a p-type semiconductor and a metal to which a potential *V* is applied, separated by an oxide or insulating layer of thickness *d* and dielectric constant $\varepsilon_t$.[22] Here $\Phi_m$ is the metal work function and $\chi$ is the semiconductor affinity, *W* is the width of depletion zone created at the surface interface of semiconductor which has dielectric constant $\varepsilon_{sc}$. Light excitation creates a

*22 It will be seen in the following chapter that in reverse bias, a voltage is in fact applied to the semiconductor. I have chosen here for clarity to shift the metal Fermi level. The energy shift for a negative bias applied to the semiconductor is negative and corresponds to reverse bias.*

population of photoelectrons in the conduction band and a photocurrent density $J_p$. The departure from equilibrium caused by light excitation and application of the bias $V$ generates a voltage $V_s$ and a Schottky current given by

$$J_s = J_{sat}\left[\exp(\frac{qV_s}{kT}) - 1\right] \tag{2.1}$$

where $q$ is the negative electronic charge. It will be seen that the form of the saturation current $J_{sat}$ depends on the model used. Here $T$ is the temperature and $k$ is the Boltzmann constant. In this equation, which will be justified in more detail below, it is pointed out that the Schottky current does not directly depend on the bias applied to the metal, but to the change of the band bending described by $V_s$.(which for $V$ = 0 is identical to the usual photovoltage)

The electron tunnel current density $J_{te}$ is the sum of all elementary contributions between a given occupied state at the semiconductor surface, at energy $E$ with respect to the semiconductor Fermi level, and an empty state at the same energy in the metal. This current density is given by [23]

$$J_{te} = \sum K(E)\rho_m(E)\rho_s(E)\, f_s(E)(1 - f_m(E))\left[\exp(-2\kappa(E)d\right] \tag{2.2}$$

where $f_s(E)$ and $f_m(E)$ are the respective occupation probabilities of the state at energy $E$ in the semiconductor and in the metal. A similar hole current density, $J_{th}$ from unoccupied metallic states can be defined. Here, *K(E)* is a constant related to the tunnel matrix element, $\rho_m(E)$, $\rho_s(E)$ are the densities of states of the metal and semiconductor surface at the corresponding energy $E$. $\kappa(E)$ is related to the electron mass $m$ and the spatially-averaged barrier $\overline{\Phi}$ by

$$\hbar^2\kappa(E)^2 / 2m = \overline{\Phi} \tag{2.3}$$

In this equation, the electron kinetic energy should be replaced by its sole component perpendicular to the surface. The tunnel currents can originate from the conduction band, the valence band, or from surface states. In order to calculate them, three equations can be written. The current conservation equations for electrons and for holes are respectively

$$\boxed{J_p - J_{te} = J_r} \tag{2.4}$$

$$\boxed{J_s = J_r - J_{th}} \tag{2.5}$$

[23] *J. G. Simmons, J. Appl. Phys.* ***34****, 1793 (1963)*

where the recombination current $J_r$, is often overlooked. Rather than writing the above current conservation equations, some works simply consider that the tunnel current is the product of the corresponding current in the solid by the tunnel probability.[24]

The third equation is the charge conservation equation, given by $Q_m + Q_{sc} + Q_{ss} = 0$ where $Q_m$, $Q_{ss}$, and $Q_{sc}$ are respectively the surface charge densities at the metal and at the semiconductor surface and in the semiconductor depletion layer. Since this equation is verified at equilibrium (zero applied bias and in the dark), we shall write a conservation equation concerning the bias and light –induced changes of the above charges.

$$\boxed{\delta Q_m + \delta Q_{sc} + \delta Q_{ss} = 0} \qquad (2.6)$$

Until now, the framework based on the three conservation equations (Eq. (2.4-6)) has not been considered completely. I explain now several models which present a simplified or partial approach.

*II.2 Expression for the photocurrent (Gärtner[25])*

In this classic work, the photocurrent $J_p$ of a metal-semiconductor structure *excited from the front side* is separated into two contributions. All electron-hole pairs excited in the depletion layer are collected by the Schottky contact. The second contribution to the photocurrent comes from the part of the photoelectrons created out of the depletion layer, which reach the depletion zone during their lifetime and are then collected by the contact. The final expression for the photocurrent, given by the resolution of the one-dimensional diffusion equation, (in the same way as in Appendix A) is

$$J_p = q\Phi\left[1 - \frac{e^{-\alpha W}}{1+\alpha L}\right] \qquad (2.7)$$

where $\alpha$ is the absorption coefficient and $\Phi$ is the photon flux, $L$ is the diffusion length of minority carriers. $J_p$ depends on bias via the width $W$ of the depletion region. As a result, the photocurrent increases with reverse bias, because since $W$ increases, more electrons are created in the depletion layer. For $\alpha W >> 1$, the photocurrent is constant since all photoelectrons are collected by the contact.

[24] *H. C. Card, Solid State Electronics* ***18****, 881 (1975)*
[25] *W. G. Gärtner, Phys. Rev* ***116****, 84 (1959)*

This dependence of the photocurrent on bias strongly complicates the interpretation of the experimental data. It will be seen below that in the present case for excitation from the rear of the cantilever, the photocurrent does not directly depend on bias.

### *II.3 Reichman*[26]

Reichman has considered the photocurrent in a n-type semiconductor-electrolyte junction under above bandgap light excitation. In this model, tunnel currents from surface states are neglected, so that only tunnel currents from the conduction or valence bands are considered. In the same way, the effect of surface states on recombination and photovoltage are neglected. An attractive idea is to consider the minority carrier concentration at the beginning of the depletion layer as an adjustable parameter, to be determined from the current conservation equation. Recombination in the depletion layer is also introduced.

Expressions for the current density as a function of photovoltage are obtained. These expressions cannot account for the experimental data to be presented in chapters 4 and 5 because no distinction is made between photovoltage and applied bias, and because the dependence of injected current on light excitation power is not considered.

### *II.4 Jansen et al* [27,28]

#### a. Surface statistics

The main originality of Nijmegen's model is the detailed description of semiconductor surface statistics under light excitation.

Figure 2.2 is the energy band scheme of the MIS junction as proposed in Nijmegen's model. The surface is assumed to be at thermodynamic equilibrium so that it is possible to define an electronic quasi Fermi level $E_{Fe}$. Because of the barrier modification caused by the presence of the photovoltage $qV_s$, the surface charge $Q_{ss}$ is modified so that $E_{Fe}$ is shifted from its position at equilibrium by a quantity $\Delta\varphi$. The surface barrier, defined as the energy difference between the top of the valence band at the surface and in the bulk is given by

$$\boxed{\varphi_b = \varphi_0 + \Delta\varphi - qV_s} \qquad (2.8)$$

[26] *J. Reichman, Appl. Phys. Lett.* ***36****, 574 (1980)*
[27] *R. Jansen, M. W. J. Prins, H. van Kempen, Phys. Rev. B* ***57****, 4033 (1998)*
[28] *M. W. J. Prins, R. Jansen, R. H. M. Groeneveld, A. P. Van Gelder, H. van Kempen, Phys. Rev. B* ***53****, 8090 (1996)*

where $\varphi_0$ is the equilibrium value of the surface barrier without applied voltage and photon excitation. Because of the large doping of the samples used, the energy difference between the Fermi level in the bulk and the top of the valence band in the bulk will be neglected.

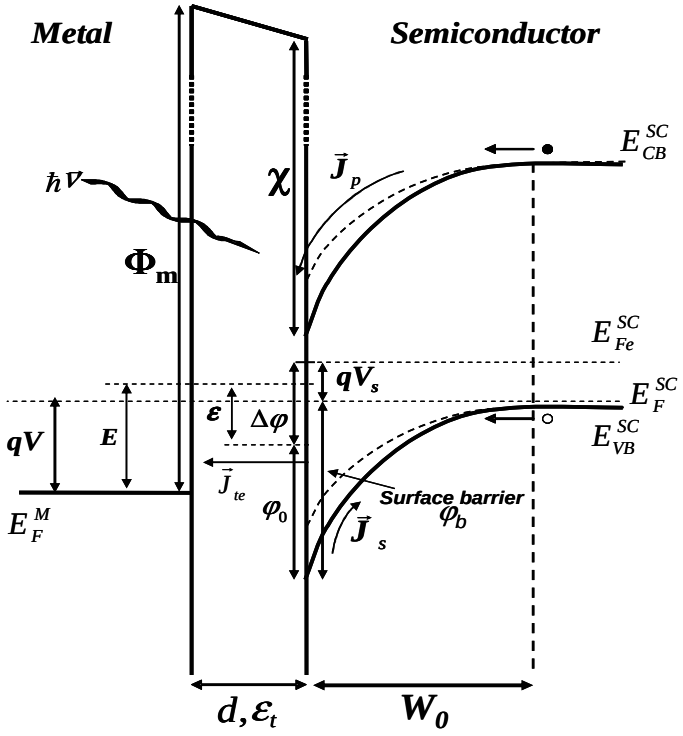


***Fig 2.2:*** *A MIS structure under Nijmegen's description in which the surface band structure is determined by the surface photovoltage $V_s$ and the variation of surface barrier $\Delta\varphi$. The energy ε of a given surface state with respect to midgap corresponds to energy E with respect to the metal Fermi level.*

In agreement with the thermionic theory of the metal-semiconductor junction,[29] the Schottky current $J_s$ is the sum of two terms. The majority carrier current is equal to $A^{**}T^2\exp(-\varphi_b/kT) = A^{**}T^2\exp(-\frac{\varphi_0+\Delta\varphi-qV_s}{kT})$ where $A^{**}$ is the Richardson constant. There is also a compensating minority carrier current, coming from the quasi Fermi level at the surface and equal to $A^{**}T^2\exp(-\frac{\varphi_0+\Delta\varphi}{kT})$. The final expression for $J_s$ is

$$J_s = J_0\exp(-\frac{\Delta\varphi}{kT})\left[\exp(\frac{qV_s}{kT})-1\right] \tag{2.9}$$

where

$$J_0 = A^{**}T^2\exp(-\frac{\varphi_0}{kT}) \tag{2.10}$$

is the usual saturation current density.

[29] *E. H. Rhoderick "Metal-semiconductor contacts" Clarendon (Oxford) 1978.*

b. Assumptions

The simplifying hypotheses of the Nijmegen model are:

i) Unlike Reichman's model, one assumes that the tunnel current flows via states at the semiconductor surface rather than from the conduction or valence band.

ii) The recombination at the interface and in the space charge region is not considered, so that Eq. (2.4) and Eq. (2.5) reduce to a single equation, further neglecting $J_{th}$

$$J_p - J_{te} = J_s \tag{2.11}$$

iii) The density of states of the semiconductor surface is assumed to be independent of energy. This assumption is valid provided $\Delta\varphi$ is smaller than the width of the distribution of surface states, which is probably the case in Jansen et al. papers where applied biases less than 0.5 V are used. As a result, neglecting the bias dependence of the height of the tunnel barrier, integrating over occupied states lying above the metal Fermi level at the semiconductor surface, Eq. (2.2) becomes

$$J_{te} = J_{te}^{0} q(V - V_s)\exp(-2\kappa d) \tag{2.12}$$

iv) The reciprocal distance $\kappa(E)$ is assumed independent on the height of the tunnel barrier and on the bias value.

c. Calculation of the photoassisted tunnel current from surface states

Eq. (2.11) and the charge conservation equation Eq. (2.6) enable the calculation of both $\Delta\varphi$ and $qV_s$ and finally an expression for the tunnel current. Eq. (2.6) can be rewritten, by considering only changes of the charges induced by light excitation and bias. The charge of photoelectrons in the depletion region is neglected so that the decrease $\varphi_b - \varphi_0$ of the surface barrier induces a decrease of the net negative charge of ionised acceptors, given by

$$\delta Q_{SC} = (1/q)C_s(\varphi_b - \varphi_0) = (1/q)C_s(\Delta\varphi - qV_s) \tag{2.13}$$

where $q$ is the negative electronic charge and

$$C_s = \varepsilon_s\varepsilon_0/W \tag{2.14}$$

is the capacitance per unit area of the depletion layer, taken constant to first order. One also has

$$\delta Q_m = C_m(V - V_s) \tag{2.15}$$

where

$$\boxed{C_m = \varepsilon_t\varepsilon_0/d} \tag{2.16}$$

is the capacitance of the tunnel gap. Finally, with the above approximations, one has

$$\delta Q_{SS} = qN_T \Delta\varphi \tag{2.17}$$

where $N_T$ is the density of surface states per unit area and per eV. The charge conservation equation Eq. (2.6) becomes

$$C_m(V - V_s) + (1/q)C_s(\Delta\varphi - qV_s) + qN_T\Delta\varphi = 0 \tag{2.18}$$

from which we obtain

$$\Delta\varphi = -\gamma_t q(V - V_s) + \gamma_s qV_s \tag{2.19}$$

where

$$\gamma_t = \frac{C_m}{C_m + C_s + q^2 N_T} \qquad \gamma_s = \frac{C_s}{C_m + C_s + q^2 N_T} \tag{2.20}$$

In reverse bias conditions, with the semiconductor grounded, the bias applied to the metal is positive and $V_s$ is negative ( $qV < 0$ and $qV_s > 0$), and one has

$$\Delta\varphi > 0 \quad \delta Q_m > 0 \quad \delta Q_{ss} < 0 \tag{2.21}$$

Resolution of the current conservation equation Eq. (2.11) using Eq. (2.18) for the photocurrent will then give the value of $V_s$ and of the tunnel current from surface states.[Eq.(2.12)]

d. Application of Nijmegen's model to our case.

In the geometry used by Jansen et al., the interpretation is complicated by two facts. Firstly, since the light excitation is from the front, in agreement with Eq. (2.7), the photocurrent directly depends on *W*. Secondly, Jansen et al. take account of the electric field configuration underneath the tip apex and multiply both the tunnel and Schottky currents by a bias-dependent numerical factor. In the present case these complications do not occur: i) since the excitation is from the rear, the second term of Eq. (2.7) is negligible and the injected photocurrent can be considered as constant. ii) The injection geometry for our tipless cantilevers is two dimensional. Application of the Nijmegen model has simple solutions in the extreme cases of small and large tunnel current.

At large distance, or for a small light excitation power, the tunnel current is small compared to the photocurrent so that this regime is called photovoltaic. Assuming that $qV_s >> kT$ , Eq. (2.11) and Eq. (2.19) become, respectively

$$J_0 \exp(-\frac{\Delta\varphi}{kT}) \exp(\frac{qV_s}{kT}) = J_p \tag{2.22}$$

$$qV_s = -\frac{\gamma_t}{(1-\gamma_t-\gamma_s)}qV + \frac{kT}{(1-\gamma_t-\gamma_s)}\ln\left(\frac{J_p}{J_0}\right) \qquad (2.23)$$

so that, as seen from Eq. (2.12), the tunnel current increases linearly with bias and is proportional to the log of the excitation power. In the opposite (photoconductive) regime, $J_{te}$ is not negligible compared to $J_p$ and all the photoelectrons tunnel to the metal surface. The tunnel current is then constant and equal to $J_p$ and is proportional to the light power.

In the general case, the bias dependence of the tunnel current, obtained from a numerical resolution of Eq. (2.12) and (2.23), is shown in Fig. 2.3 for several values of the photocurrent.[30] As predicted above, the tunnel current first increases linearly as a function of bias (and logarithmically as a function of light power) before saturating at $J_p$. It is then independent of bias and increases linearly as a function of light excitation power. Fig. 2.3 shows that the switching between the photovoltaic and photoconductive regimes is quite abrupt and occurs in a bias range smaller than 0.1eV.

Unlike the prediction of Fig. 2.3 the observed bias dependence of the tunnel current will be shown in Chapter 4 to be far from linear so that the Nijmegen model cannot account for the results.

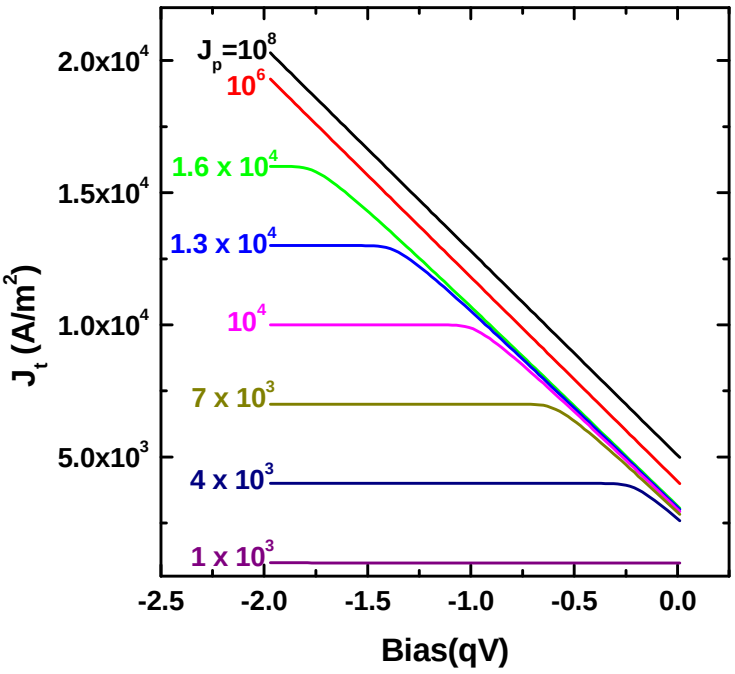


***Fig 2.3:*** *J-V characteristic as a function of photocurrent density as predicted by the Nijmegen model.*

[30] *In this calculation, the work function of metal surface is assumed to be 5 eV, the density of surface states* $N_T$ *is taken as* $10^{18} m^{-2} eV^{-1}$ *and the concentration of acceptors in the semiconductor bulk is fixed at* $10^{24} m^{-3}$. *The dielectric constant is taken as 1 for the tunnel gap and 13 for GaAs.*

*II.5 Effect of bias dependence of tunnel barrier height ("Advanced Nijmegen model")*

I have first brought a simple refinement to the Nijmegen model, by taking account of the known bias dependence of the tunnel barrier height. The tunnel barrier which appears in Eq. (2.3) is the *spatial average* of the microscopic barrier.[31] Neglecting image charge effects, the barrier with respect to the *semiconductor Fermi level* is the average of the energy of the vacuum levels of the metal and of the semiconductor. As seen in Fig. 2.2, the vacuum level of the metal lies at an energy equal to $\Phi_m + qV$ where $\Phi_m$ is the metal work function, and changes linearly with bias. The energy of the semiconductor vacuum level is $-\varphi_b + E_G + \chi$, where $\chi$ is the semiconductor affinity, and depends on $V_s$ and $\Delta\varphi$ through $\varphi_b$.

For a given surface state, defined by its energy $\varepsilon$ with respect to midgap, the tunnel barrier is then given by

$$\overline{\Phi} = \Phi_s^* + \frac{q}{2}(V - V_s) + \frac{\Delta\varphi}{2} - \varepsilon$$

where $\Phi_s^* = \frac{1}{2}(\Phi_m + \chi + \varphi_0)$ and $\overline{\Phi} - \Phi_s^*$ is the part of the tunnel barrier which depends on bias and on the energy of the surface state. The expression for $\kappa$, given by Eq. (2.3), to first order in $(\overline{\Phi} - \Phi_s^*)/\Phi_s^*$ is given by

$$\kappa d_0 = \sqrt{\Phi_s^*} + \left[\frac{\overline{\Phi} - \Phi_s^*}{2\sqrt{\Phi_s^*}}\right]$$

where $d_0 = \hbar/\sqrt{2m}$ is a distance times the square root of an energy. One has exp(-2 $\kappa d$ ) = $A \exp\left\{-\frac{\omega_s}{kT}\left[q(V - V_s) + \Delta\varphi - 2\varepsilon\right]\right\}$ where $A = \exp\left[-2d\sqrt{\Phi_s^*}/d_0\right]$ and where $\omega_s = \frac{d}{2d_0}\frac{kT}{\sqrt{\Phi_s^*}}$

is the reduced distance. The tunnel current, obtained by integration between the electron quasi Fermi level and the metal Fermi level, is given by

$$J_{ts} = N_T(0) A \exp\left\{-\frac{\omega_s}{kT}\left[q(V - V_s) + \Delta\varphi\right]\right\} \int_{\Delta\varphi + q(V - V_s)}^{\Delta\varphi} K_s(E)\rho_m(E)\exp\left(\frac{2\varepsilon\omega_s}{kT}\right)d\varepsilon \quad (2.24)$$

where $N_T(0)$ is the surface state density and the energy $E$ with respect to the metal Fermi level is given by $E = \varepsilon - \Delta\varphi + qV_s - qV$. In the case of gold, where $\rho_m(E)$ is a constant and $K(E)$ is equal to the matrix element $K_s$ for surface states, integration of Eq. (2.24) gives

[31] *J. G. Simmons, J. Appl. Phys.* ***34****, 1793 (1963)*

$$J_{ts} = -2N_T(0)(kT/2\omega_s)AK_s\rho_m \exp\{\omega_s \Delta\varphi / kT\} Sh\{[q(V-V_s)]\omega_s / kT\}$$

where $\Delta\varphi$ is given by Eq. (2.19) and, in the photovoltaic regime, $qV_s$ is given by Eq. (2.23).

In the framework of the Nijmegen model [Eq. (2.19)], $\Delta\varphi$ depends linearly on bias and photovoltage and the predicted bias dependence of the tunnel current is exponential, whereas nonexponential dependences are observed (Chapter 4 and 5) at small distances. This shows that, for the large bias range used here the energy dependence of the surface density of states must play a role in Eq. (2.24). In addition, the dependence of the tunnel current as a function of light power is not in agreement with the experimental results. Assuming that $-[q(V-V_s)]\omega_s$ >>kT, only one exponential term of the hyperbolic sine can be retained. Using Eq. (2.23), one finds a power-law dependence, with an exponent $\omega_s[1+\gamma_t+\gamma_s]/[1-\gamma_t-\gamma_s] \approx \omega_s$. Since $\omega_s \approx 10^{-3}$ and since $\gamma_t$ and $\gamma_s$ are typically smaller than several percent, the exponent is more than a factor of 10 smaller than the measured quantity. As will be seen in the following section, these results suggest that, unlike assumption i) of the Nijmegen model, tunnelling from electrons in the conduction band plays a dominant role.

## *III. Model for charge injection*

The key points of the present model are:

- Inclusion of tunnelling from the conduction band which, although neglected in the Nijmegen work, has already been found to be dominant for tunnelling from silicon tips.[32] Also considered is the modification of tunnelling from the valence band by the light excitation.

- Quantization of electronic states in the depletion layer near the surface. (This is important for $p^+$ GaAs.)

- Inclusion of a surface recombination velocity *S* dependent on the density of surface states at the quasi Fermi level. Assuming that, at equilibrium, the surface Fermi level is pinned at the maximum of the density of states, ($\Delta\varphi$=0), the increase of $\Delta\varphi$ results in a decrease of *S* which should induce an increase of the tunnel current from the conduction band.

- Inclusion of the bias dependence of the tunnel barrier, closely following the treatment of Sec. II.5. ("Advanced Nijmegen model")

[32] *A. C. H. Rowe and D. Paget Phys. Rev. B* ***75****, 115311 (2007)*

It will be seen below that, at large distance, the bias dependence of the tunnel current is rather determined by the bias dependence of the tunnel barrier, while at small distance, the change of *S* becomes dominant. Because of this variation, the electronic concentration $n_0$ at the beginning of the depletion layer is considered as an unknown parameter. The three conservation equations (2.4) (2.5) and (2.6) are used to calculate $qV_s$, $\Delta\varphi$, and $n_0$.

While a completely general model can be made, we make the following assumptions:

i) In order to obtain analytic expressions for the tunnel currents, these currents are assumed smaller than the Schottky and photocurrents, so that we limit ourselves to the photovoltaic regime defined in Sec. II.4. Furthermore, using Eq. (2.9), the two conservation equations Eq. (2.4) and (2.5) become respectively Eq. (2.11) which we reproduce here

$$J_s = J_0 \exp(-\frac{\Delta\varphi}{kT})\left[\exp(\frac{qV_s}{kT})-1\right] = J_p \qquad (2.25)$$

and

$$J_s = J_r$$

ii) We define a thermodynamic quasi-equilibrium, characterised by electron and hole quasi Fermi levels, for which the energy difference at the surface is equal to $qV_s$. We further assume that the energies of these levels are constant throughout the space charge layer. As discussed elsewhere,[33, 34] this approximation holds if the carrier diffusion lengths are larger than the space charge layer width and if photocurrents and recombination currents in the space charge layer are sufficiently small. The hole concentration at the semiconductor surface, is related to the surface barrier $\varphi_b$ by

$$p_s = (N_A + n_0)e^{-\frac{\varphi_b}{kT}} \qquad (2.26)$$

For a strongly-doped material, the concentration $n_s$ is that in the lowest quantised state. This state lies at an energy $f^*\varphi_b$ above the bottom of the conduction band at the surface, where it has been shown[35] that $f^*$ is between 0 and 1 and approximately related to the surface electric field $E_{eff}$ by

$$f^* \approx \frac{1}{\varphi_b}\left(\frac{q^2\hbar^2 E_{eff}^2}{2m^*}\right)^{1/3}\left[3\pi/4\right]^{2/3} \qquad (2.27)$$

One then has

[33] *L. Kronik, and Y. Shapira, Surf. Sci. Rep.* ***37****, 1 (1999)*
[34] *C. G. B. Garret and W. H. Brattain, Phys. Rev* ***99****, 376 (1955)*
[35] *J. He, M. Chan and Y. Wang, IEEE trans. El. Dev.* ***53****, 2082 (2006)*

$$n_s = n_0 e^{\frac{(1-f^*)\varphi_b}{kT}} \qquad (2.28)$$

iii) While it has been found that the density of surface states is generally strongly peaked near midgap,[36] it is assumed for simplicity that this density of states is exactly peaked at midgap and that consequently the barrier in the dark is equal to half the bandgap.

Shown in Fig. 2.4 is the one dimensional energy diagram for our planar tunnel metal - p type semiconductor junction. In section III.1 below, the key quantities of the system ($V_s$, $S$, $n_0$) are expressed as a function of $\Delta\varphi$. $\Delta\varphi$ is then obtained from a resolution of the charge conservation equation.

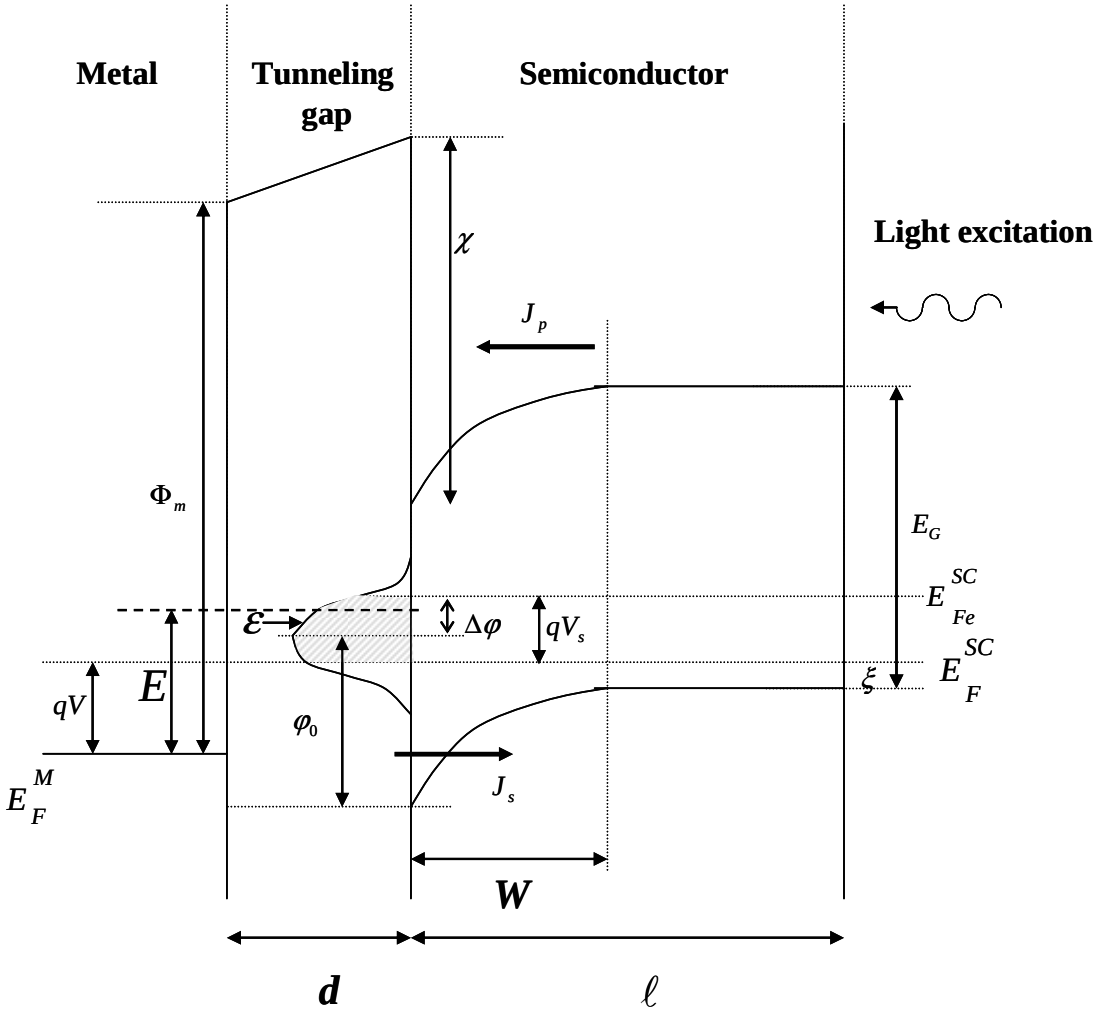


***Fig 2.4:*** *Description of the MIS structure under light excitation*

[36] *E. W. Kreutz, Phys. Stat. Sol. (a)* ***56****, 687 (1979)*

*III.1 Surface photovoltage and surface recombination velocity*

a. Expressions for $V_s$ and for the photoelectron concentration

I first calculate the injected photocurrent density as a function of the surface recombination velocity. As shown in Appendix A, a resolution of the one-dimensional diffusion equation in the semiconductor bulk gives

$$n_0 = \beta\, N_0 \tag{2.29}$$

$$J_p = qn_0 S = q\beta N_0 S \tag{2.30}$$

where

$$\beta = (1 + S/v_d)^{-1} \tag{2.31}$$

Here $N_0$ and $v_d$ do not depend on recombination velocity $S$ or tip bias. Their expressions are given in Appendix A. The effective electron concentration $N_0$ is proportional to the light excitation power and the diffusion velocity $v_d$ is proportional to the ratio $D/L$ of diffusion constant and diffusion length.

Using Eq. (2.25) and further assuming that $e^{\frac{qV_s}{kT}} >> 1$, $J_p = q\beta N_0 S$ gives

$$\boxed{qV_s = qV_s^* + \Delta\varphi + kTLog[1-\beta]} \tag{2.32}$$

The quantity $V_s^*$, defined by

$$qV_s^* = kTLog(qv_d N_0 / J_0)$$

is equal to the usual value of the photovoltage $kTLog(J_p / J_0)$ in the limit where $S >> v_d$. Note that, with respect to most studies performed for light excitation at the front surface,[37] the transmission geometry strongly simplifies the expression for the effect of surface recombination on the photovoltage value.[given by Eq. (2.32) in the case where $V = 0$]

Further use Eq. (2.26), Eq. (2.28) and $J_p = qn_0 S$, yields

$$\boxed{n_s = \frac{A^{**}T^2}{qS}\exp(-f^*\varphi_b / kT) = \frac{A^{**}T^2}{qS}\left[\frac{qSn_0}{A^{**}T^2}\right]^{f^*}} \tag{2.33}$$

In the absence of quantization, ($f^* \approx 0$) $n_s$ only depends on the excitation power via the quantity $1/S$. This result implies that the increase of $n_0$ caused by the increase in light excitation power is compensated by the decrease of $\exp(\varphi_b / kT)$ caused by the increase of $V_s$. Quantization introduces an extra dependence of $n_s$ on the excitation power. The expression

[37] *L. Kronik, and Y. Shapira, Surf. Sci. Rep.* ***37****, 1 (1999)*

for $\exp(-f^*\varphi_b/kT) = \left[\frac{qSn_0}{A^{**}T^2}\right]^{f^*}$ is obtained using Eq. (2.8) for the surface barrier and Eq. (2.32) for the photovoltage.

b. Expression for the surface recombination velocity

It is assumed, as discussed in Appendix C, that the density of surface states has a maximum at midgap $N_T(0)$ and a relative dependence $D(\varepsilon)$, as a function of energy difference from midgap $\varepsilon$, of typical half width at half maximum $\sigma$ of the order of $\sigma \approx 0.1$-$0.2$ eV.[38] These states induce a recombination current calculated in Appendix B,[39] [Eq. (B.16)] and takes the form of an integral over the shaded range of energies shown in Fig. 2.4.

$$J_r = qN_T(0)\int_{-qV_s+\Delta\varphi}^{\Delta\varphi} D(\varepsilon)\sigma_p v_p \left[n_s p_s - n_i^2\right] n_s^{-1} d\varepsilon \qquad (2.34)$$

Here $\sigma_p$ is the hole capture cross section, for a hole velocity $v_p$. Applying elementary semiconductor statistics to the surface,[40] where the hole and electron quasi Fermi level energies differ by $qV_s$, one finds $n_s p_s - n_i^2 = n_i^2\left(e^{\frac{qV_s - f^*\varphi_b}{kT}} - 1\right) \approx n_i^2 e^{\frac{qV_s - f^*\varphi_b}{kT}}$. Since the occupation probability is close to unity for all states lying between the two quasi Fermi levels, the only states which contribute to surface recombination are in a relatively narrow range of typical width $kT$ situated near $E_{Fn}$. One has

$$J_r \approx J_{r0}\frac{N_T^* D(\Delta\varphi)}{n_s} e^{\frac{qV_s - f^*\varphi_b}{kT}} = J_{r0}\frac{N_T^* D(\Delta\varphi)}{A^{**}T^2} qSe^{\frac{qV_s}{kT}} \qquad (2.35)$$

where $J_{r0} = qv_p n_i \left(an_i\sigma_p\right)$ and $N_T^* = N_T(0)kT/a$ is an equivalent volume concentration of the relevant centres. The effective thickness $a$ of the surface only plays a role for the homogeneity of the expressions for $N_T^*$ and $J_{r0}$ and cancels in Eq. (2.35). Using $J_s = J_r$, one finds finally

$$\boxed{S = S_0 \exp(-\frac{\Delta\varphi}{kT}) / D(\Delta\varphi)} \qquad (2.36)$$

[38] *E. W. Kreutz, Phys. Stat. Sol. (a)* ***56****, 687 (1979)*
[39] *D. Aspnes, Surf. Sci,* ***132****, 406 (1983)*
[40] *R. A. Smith, Semiconductors, Second Edition, Cambridge University Press, Cambridge, 1978.*

where the equilibrium surface recombination velocity is given by $S_0 = (J_0^2 / qN_T^* J_{r0})\, e^{\frac{\varphi_0}{kT}}$. This expression is not modified by quantization of surface electronic states. It will be used in Eq. (2.33) to find $n_s$.

c. Charge densities

Two modifications are brought to the simplified charge conservation equation (Eq. 2.18) of the Nijmegen model. First the charge density $\delta Q_{ss}$ at the semiconductor surface is obtained by an integration of surface states. For the expression of the charge of the depletion layer, $\delta Q_{sc}$ we take into account both the charge of ionized acceptors and of conduction electrons. This calculation is given by Kronik and Shapira.[41] The total charge in the depletion layer is equal to $\varepsilon_s E_{eff}$, where $E_{eff}$ is the surface electric field and $\varepsilon_s$ is the semiconductor dielectric constant. This electric field is obtained by integrating the Poisson equation over distance where the electronic concentration at a given distance is in thermodynamic equilibrium with the bulk.

Removing terms at equilibrium, for which the sum is zero, Eq. (2.18) becomes finally

$$C_m\left[V + (1/q)(\varphi_b - \varphi_0)\right] + qW_0 N_A \left[\sqrt{\left[\frac{\varphi_b}{\varphi_0}\right]\left[1 + \frac{n_s}{N_A}\frac{kT}{\varphi_b}\right]} - 1\right] + qN_T(0)\int_0^{\Delta\varphi} D(\varepsilon)d\varepsilon = 0 \qquad (2.37)$$

Here $W_0$ is the equilibrium value of the depletion layer width and $N_A$ is the acceptor concentration. Since $\varphi_b$ and $n_s$ which appear in this equation are functions of $\Delta\varphi$, numerical resolution of this equation will give $\Delta\varphi$. Using Eq. (2.36), Eq. (2.32) and Eq. (2.8), one then obtains $S$, $V_s$ and $\varphi_b$. The structure of the calculation is summarised in the following inset.

[41] *L. Kronik, and Y. Shapira, Surf. Sci. Rep.* ***37****, 1 (1999)*

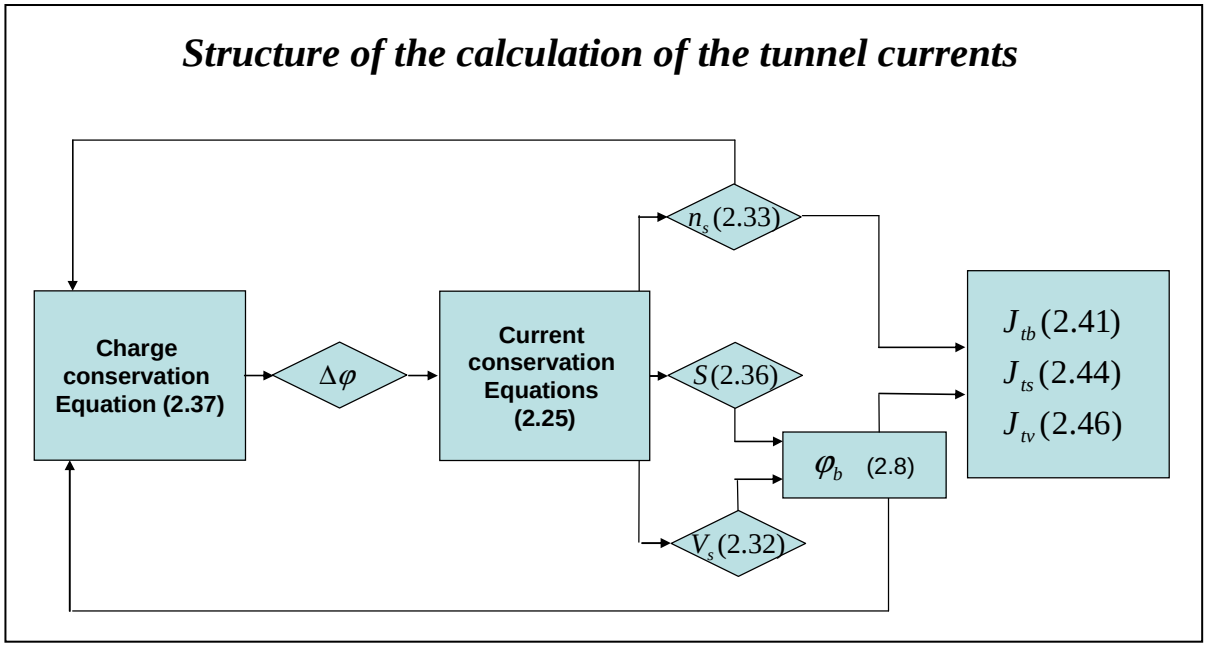


*III.2 Tunnel photocurrents and photoassisted tunnel currents*

a Tunnel photocurrent $J_{tb}$ from the conduction band

Calculation of this current requires integration over all conduction electrons of energy $\varepsilon_c$ above the conduction band edge at the surface.[42] Considering the perpendicular and parallel components $k_\perp$ and $k_{//}$ components of the momentum, it is known from first principles that the parallel component is conserved in the tunnel process, and is therefore the same in the tunnel gap and in the metal. The perpendicular momenta $i\kappa$ in the tunnel gap and $k'_\perp$ in the metal are then determined by energy conservation. It is then straightforward to impose continuity of the wavefunctions and their derivatives at the semiconductor/vacuum and the vacuum/metal interfaces.

For a given electron, assuming that $\exp(-2\kappa d) << 1$, one finds that the tunnel probability is proportional to $G(\varepsilon_c)\exp(-2\kappa d)$ where

$$G(\varepsilon_c) = \frac{k}{k'} \frac{1}{\left(1 + k_\perp / k'_\perp\right)^2 + \left(\kappa / k_\perp + k'_\perp / \kappa\right)^2} \qquad (2.38)$$

[42] *In the case of quantisation, $\varepsilon_c$ is composed of a part related to $k_\perp$ mostly determined by the potential energy of the quantised states and of a second part due to kinetic energy parallel to the surface.*

As discussed in Eq. (2.2), the tunnel current at a given energy $\varepsilon_c$ also depends on the product of the tunnel matrix element, of the metallic density of states and of the concentration of electrons of energy $\varepsilon_c$ at the semiconductor surface.

The tunnel barrier $\overline{\Phi}$ is computed in the same way as for the advanced Nijmegen model. [Sec. II.5] The surface concentration of tunnelling electrons at kinetic energy $\varepsilon_c$ is $W(\varepsilon_c)\rho(\varepsilon_c)\left[n_s \exp(-\frac{\varepsilon_c}{kT})\right]$ where the multiplication by the width $W(\varepsilon_c)$ of the space charge layer at $\varepsilon_c$ converts a volume concentration to a surface one and $\rho(\varepsilon_c)$ is the density of states. One finally has

$$J_{tb} = Kn_s \exp(-2d\sqrt{\overline{\Phi}}/d_0)\times$$
$$\times\int_0^{\varphi_b} \rho_m(E)W(\varepsilon_c)G(\varepsilon_c)\rho(\varepsilon_c)\exp(\frac{\varepsilon_{c\perp}d}{d_0\sqrt{\overline{\Phi}}}-\frac{\varepsilon_c}{kT})\,d\varepsilon_c \qquad (2.39)$$

Since $W(\varepsilon_c)G(\varepsilon_c)$ is zero for $\varepsilon_c = 0$ and increases with $\varepsilon_c$, one can assume that the majority of tunnel electrons have a nonzero energy, written for simplicity $f\varphi_b$ such that

$$K\int_0^{\varphi_b} W(\varepsilon_c)G(\varepsilon_c)\rho(\varepsilon_c)\exp(\frac{\varepsilon_{c\perp}d}{d_0\sqrt{\overline{\Phi}}}-\frac{\varepsilon_c}{kT})\,d\varepsilon_c \approx K_c W_0 \exp\left[-\frac{f\varphi_b}{kT}\right] \qquad (2.40)$$

where $K_c$ is a constant. Because of the dependence of the tunnel probability on energy, the tunnelling electrons can be at an energy larger than the lowest quantized state, so that *f* is *a priori* larger than $f^*$, given by Eq. (2.28). Using $\exp\left[-\frac{f\varphi_b}{kT}\right] = \left[\frac{qSn_0}{A^{**}T^2}\right]^f$ the tunnel current is expressed as the product of an exponential dependence, due to the bias dependence of the barrier height, and of an effective concentration $N^*(S)$, which depends on the surface recombination velocity:

$$\boxed{J_{tb} = J_{tb}^0 N^*(S)\exp\left(-\frac{\omega qV}{kT}\right)} \qquad (2.41)$$

$$N^*(S) = \frac{A^{**}T^2}{qS}W_0\left[\frac{qSn_0}{A^{**}T^2}\right]^{f+\omega(1-2\alpha f)} \qquad (2.42)$$

where

$$\omega = \frac{d}{2d_0}\frac{kT}{\sqrt{\Phi_b^*}} \qquad (2.43)$$

is the reduced distance. As found from the values of the work function given in Appendix C, its typical value is several $10^{-3}$ for $d$=1nm. One has $J_{tb}^{0} = K_c \rho_m [E] \exp\left[ -\frac{2d\sqrt{\Phi_b^*}}{d_0} + \frac{d(1-2f)\varphi_0}{2d_0\sqrt{\Phi_b^*}} \right]$, $\Phi_b^* = [\Phi_m + \chi - E_G + (1-2f)\varphi_0]/2$. Eq. (2.43) also contains the parameter $\alpha = \varepsilon_{c\perp}/\varepsilon_c$. This quantity is not known but does not play an important role because of the small value of $\omega$. ($\omega \approx 5x10^{-2}$ for $d$=1nm)

b. Tunnel photocurrent $J_{ts}$ from surface states

The tunnel current from surface states, given by Eq. (2.24), can be rewritten, introducing the energy dependence of the density of surface states $D(\varepsilon)$ and taking account of the expression for $V_s$ of Eq. (2.32)

$$\begin{aligned} J_{ts} &= N_T(0) A \exp\left\{ -\frac{\omega_s}{kT}[q(V-V_s)+\Delta\varphi] \right\} \int_{\Delta\varphi+q(V-V_s)}^{\Delta\varphi} K_s(E)\rho_m(E)D(\varepsilon)\exp\left(\frac{2\varepsilon\omega_s}{kT}\right)d\varepsilon \\ &= N_T(0) A \exp\left[ -\frac{q\omega_s V}{kT} \right] \left[ \frac{qSn_0}{J_0} \right]^{\omega_s} \int_{\Delta\varphi+q(V-V_s)}^{\Delta\varphi} K_s(E)\rho_m(E)D(\varepsilon)\exp\left(\frac{2\varepsilon\omega_s}{kT}\right)d\varepsilon \end{aligned} \quad (2.44)$$

where it is recalled that $A = \exp\left[ -2d\sqrt{\Phi_s^*}/d_0 \right]$. Since $\omega_s$, defined in Sec. II.5, is generally much smaller than unity, $(qSn_0/J_0)^{\omega_s}$ weakly depends both on power and bias.

In summary, the tunnel photocurrents, defined by Eq. (2.42) and (2.44), are expressed as a function of the applied bias $qV$, of the quantity $n_0$ which depends on the light excitation power, and of the surface recombination velocity. The value of this velocity is related by Eq. (2.36) to the quantity $\Delta\varphi$, and is found from the resolution of the charge conservation equation Eq. (2.37).

c. Dark current

The calculation of the dark current will not be explained in detail.

For a forward bias the expression of the ideality factor has been found by separating the interface states into a fraction $\eta$ of the total number of states for which the occupation follows the metal statistics and a fraction 1-$\eta$ which are rather coupled to the semiconductor.[43, 44] Including residual processes which induce a dependence of the barrier on

[43] *H. C. Card and E. H. Rhoderick, J. Phys. D* ***4****, 1589 (1971)*

bias, such as image charge effects and tunnelling of holes across the barrier, one finds to first order

$$\frac{1}{n} = 1 - \frac{\varepsilon_s / W + q(1-\eta) N_T(0)}{C_m + \varepsilon_s / W + q N_T(0)} - \alpha_d \qquad (2.45)$$

where $\alpha_d$ is the contribution of the residual processes. The second and third terms of Eq. (2.45) are equal to the derivatives of the barrier as a function of the bias applied to the semiconductor (here $qV_s - \Delta\varphi$) due to the corresponding process.[45]

For a reverse bias, one defines $\Delta\varphi$ and $qV_s$ in the same way as under light excitation. Current conservation implies that the dark tunnel current, defined by Eq. (2.44), [46] is equal to the Schottky current. For the Schottky current, because of the large value of the applied bias, the first order approximation for a forward bias is replaced by a second order approach where the barrier $\varphi_0$, defined in Eq. (2.8), is replaced by $\varphi_0^* = \varphi_0 + \alpha_d (qV_s - \Delta\varphi) + \alpha'_d (qV_s - \Delta\varphi)^2$. In the condition for charge neutrality of Eq. (2.37), one must first make $n_s$=0 in $\delta Q_{sc}$. The third term $\delta Q_{ss}$ must take account of two types of states and becomes $q\eta N_T(0)\int_0^{\Delta\varphi} D(\varepsilon)d\varepsilon - q(1-\eta)N_T(0)\int_{E_{Fm}}^{0} D(\varepsilon)d\varepsilon$. The current and charge conservation equations are nonlinear and must be solved numerically in a coupled way to obtain $\Delta\varphi$ and $qV_s$ and to calculate the tunnel current.

For a forward bias the ideality factor depends on $\eta$ and $\alpha_d$. The dark current under reverse bias also depends on $\alpha'_d$ and on the tunnel matrix element $K_s$ defined in Eq. (2.44). Since the expression of the tunnel current uses the product $K_s N_T(0)$, the quantity $N_T(0)$ will be replaced by an effective density of states $N_T^d(0)$. In the same way as for the Nijmegen model under light excitation, the dark current behaviour exhibits two regimes. At large distance, in the voltaic regime, $qV_s$ is nearly independent on bias, so that the band structure of the semiconductor at the surface does not follow the metal Fermi level. At short distance, in the conductive regime, $qV_s \approx qV$ so that the semiconductor surface band structure follows the motion of the Fermi level of the metal. In this case, the top of the valence band at the surface lies approximately at $qV - \varphi_0$.

---

*[44] Under light excitation, since capture processes of photoelectrons increase the kinetics of establishment of equilibrium with the semiconductor, it is not a bad approximation to assume that η=0.*
*[45] E. H. Rhoderick "Metal-semiconductor contacts" Clarendon (Oxford) 1978.*
*[46] The dark tunnel current from the valence band will be shown in Chapter 4 to be negligible with respect to that from surface states.*

d. Photoassisted tunnel current $J_{tv}$ from the valence band.

A mechanism for photoassisted tunnelling is the light-induced modulation of the tunnel current from the valence band. This mechanism is illustrated in Fig. 2.5

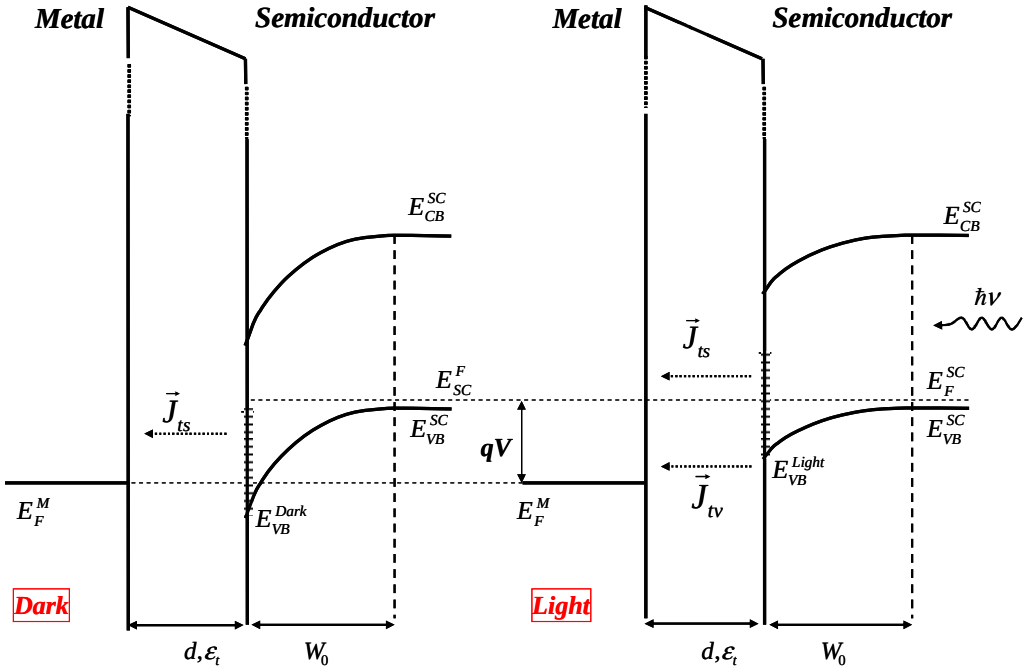


***Fig. 2.5:*** *Energy band structure of a MIS junction without light excitation (left) and under light excitation (right). The photoelectrons generated in the bulk flow toward the contact interface then reduce the surface barrier. When –qV> $\varphi_b$ , there appears an electron tunnel current from an occupied level in the valence band to unoccupied states at metal surface. This current is quenched or reduced in the dark because of the variation of the barrier.*

Described in the left panel of Fig. 2.5 is the band structure schematic in the dark in the case where the valence band edge at the surface $E_{VB}^{dark}$ lies below the metal Fermi level $E_F^M$ . This corresponds to the conductive mode explained in the preceding section. Under light excitation,(right panel of Fig. 2.5) because of the photovoltage, this position $E_{VB}^{light}$ , which lies at an energy $\varphi_b$ below the bulk Fermi level, may lie above $E_F^M$ . As a result, the tunnel current of valence electrons situated between $E_{VB}^{light}$ and $E_F^M$ is quenched under light excitation and contributes to the photoassisted tunnel current.

This current appears as soon as $-qV > \varphi_b$. This contribution is an integral over the energy $\varepsilon_v$ below the valence band edge, and is given by

$$J_{tv} = J_{tv}^{0} \exp\left[-\frac{\omega_v q V}{kT}\right]\left[\frac{qSn_0}{J_0}\right]^{\omega_v} \int_0^{qV-\varphi_b} G_v(\varepsilon_v)\rho_m(E)D(\varepsilon_v)\exp(-\frac{4\omega_v \varepsilon_{v\perp}}{kT})d\varepsilon_v \tag{2.46}$$

where

$$\omega_v = \frac{d}{2d_0}\frac{kT}{\sqrt{\Phi_v^*}} \tag{2.47}$$

$$\Phi_v^* = \left[\Phi_m + \chi + E_G + \varphi_0\right]/2 \tag{2.48}$$

$$J_{tv}^{0} = K_v \exp\left[-\frac{2d\sqrt{\Phi_v^*}}{d_0}\right] \tag{2.49}$$

and

$$D(\varepsilon_v) = \frac{\ell_c \left(2m^*\right)^{3/2}}{\hbar^3}\sqrt{\varepsilon_v} \tag{2.50}$$

where $\ell_c$ is the coherence length, is the density of states per unit surface and per eV in the valence band. $K_v$ gives a measure of the tunnel matrix element and, in the same way as in Eq. (2.38),

$$G(\varepsilon_v) = \frac{k_v}{k'}\frac{1}{\left(1+k_{v\perp}/k_\perp'\right)^2 + \left(\kappa/k_{v\perp} + k_\perp'/\kappa\right)^2} \tag{2.51}$$

In the same way as for surface states, the dependence of this current as a function of light excitation power is given by the third factor of Eq. (2.46) and is of the form $N_0^{\omega_v}$ where $\omega_v$ is smaller than $\omega_s$ because of the large value of the tunnel barrier. In the same way as for surface states, the photoassisted tunnel current from the valence band weakly depends on light excitation power.

## *IV. Physical processes for photoassisted tunnelling.*

The description of the preceding section considers three possible photoassisted tunnel processes (tunnelling from the conduction band, from surface states or from the valence band) and two main mechanisms for the bias dependence of the tunnel current (bias dependence of the tunnel barrier height or of the surface recombination velocity).

The relative importance of the tunnel processes relies on the knowledge of the respective tunnel matrix elements, which are not well-known, so that the discussion of this

issue relies on the experimentally observed dependence of the tunnel current and will be postponed to Chapter 4.

In the present discussion, we consider the relative importance of the bias dependence of the tunnel barrier height and of the surface recombination velocity. For specificity, we take reasonable values of the parameters from the literature. These values are given in Appendix C. The density of surface states $N_T(0)$ will be chosen to be $6x10^{18}eV^{-1}m^{-2}$, as justified in Sec. V. 2b of Chapter 4 from the experimental results.

It is shown here that, at large distance, the photocurrent bias dependence occurs mainly because of the bias dependence of the tunnel barrier while, at small distance, the change of surface recombination velocity is dominant. These issues are directly related to pinning of the electron quasi Fermi level by the band of midgap surface states: As long as the Fermi level is pinned by the band of surface states, $\Delta\varphi << \sigma$, the density of states at the quasi Fermi level does not strongly change. The bias-induced change of surface recombination velocity is small so that the bias-dependence of the photocurrent is dominated by that of the tunnel barrier. In the opposite case of unpinning, the electron quasi Fermi level lies outside of the main band of surface states so that the resulting strong decrease of the surface recombination velocity plays a dominant role.

The change of $\Delta\varphi$ is determined by the bias-induced change of the surface charge $\delta Q_{ss}$ which is determined by the charge conservation equation Eq. (2.37). As seen from the shape of this equation, $\Delta\varphi$ is obtained by a graphical resolution consisting in plotting as a function of $\Delta\varphi$ the quantity $A_q = -V$ , where

$$A_q = V_s^* + \frac{kT}{q} Log(1-\beta) + \frac{\delta Q_{sc}}{C_m} + \frac{\delta Q_{ss}}{C_m} \qquad (2.52)$$

Shown in Fig. 2.6 is the distance dependence of $A_q$ for several values of $C_m$. For illustrative purposes, one neglects here the presence of electronic quantised states.(i.e. $f^*$=0) Also shown in the figure are the dependences of $\delta Q_{sc}/C_m$ and $\delta Q_{ss}/C_m$ as a function of $\Delta\varphi$ in the case of Curve i.

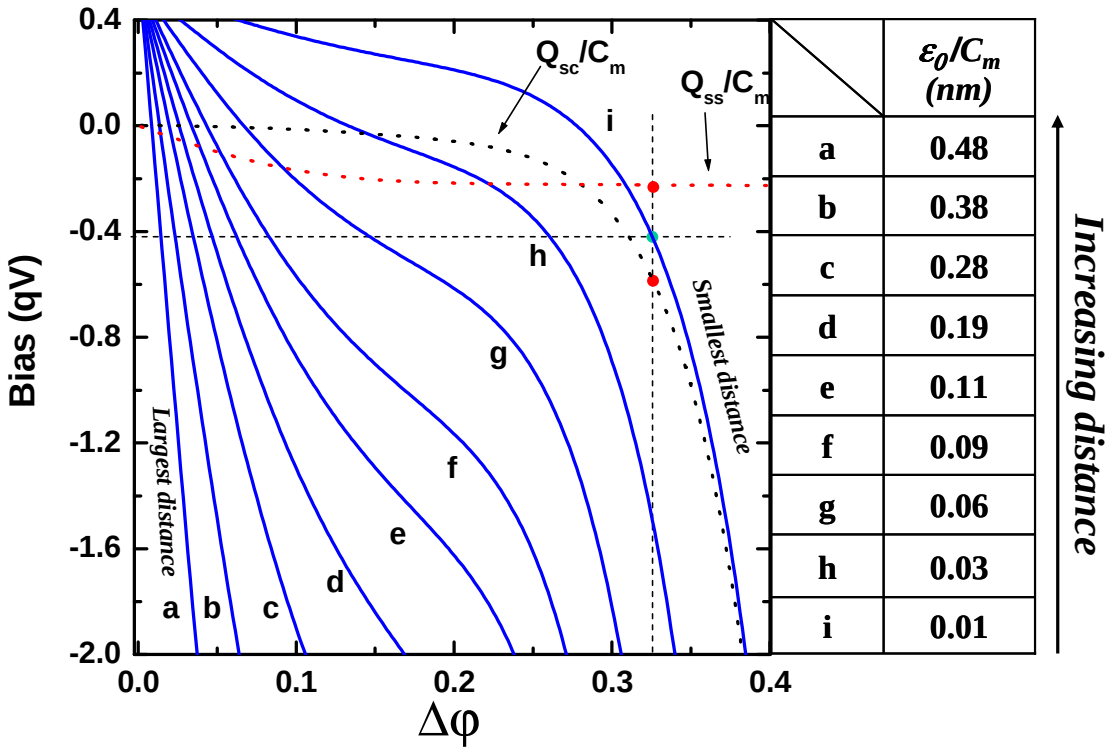


***Fig. 2.6:*** *Dependence of the quantity $A_q$ defined by Eq. (2.52) as a function of $\Delta\varphi$. For a given bias V, the value of $\Delta\varphi$ is the one which gives $A_q$=-V. As an example, for a bias of -0.4V, the value of $\Delta\varphi$ for curve i is found of 0.33 eV. The biases $Q_{ss}/C_m$ and $Q_{sc}/C_m$ are indicated by red dots. The values of $\varepsilon_0/C_m$ for the various curves are given in the table.*

At large distance the maximum value of $\Delta\varphi$ for Curve a, of 30 meV, is smaller than the width $\sigma$ of the surface density of states, so that the electron quasi Fermi level is indeed pinned near midgap. This implies that the change of surface barrier is small so that the change of $\delta Q_m$ (which is small because of the small value of the capacitance $C_m$) is mostly compensated by that of $\delta Q_{ss}$. Since $\Delta\varphi$ is small, $\delta Q_m$ and $\delta Q_{ss}$ are approximated by Eq. (2.15) and (2.17), (Nijmegen model) and one finds

$$\Delta\varphi \approx -\gamma_t^* q\left[V - V_s^*\right] = \frac{C_m\left[V - V_s^*\right]}{|q| N_T(0)} \qquad (2.53)$$

In this pinning situation the surface recombination velocity is still larger than $v_d$ so that Eq. (2.31) gives $\beta<<1$.

Conversely, at small distance, the value of $\Delta\varphi$ is larger than $\sigma$ which induces unpinning of the surface Fermi level. There results [according to Eq. (2.36)] a strong decrease of the surface recombination velocity, which implies an increase of the electron concentration

$n_s$ that can be as large as three orders of magnitude. For a very small distance one has $|\delta Q_{sc}| >> |\delta Q_{ss}|$.

## *V. Calculation of spin-dependent tunnel photocurrents*

In Chapter 5 one measures for a given surface magnetisation the tunnel photocurrent $I_t^{ph}$ as a function of excitation light helicity, and one obtains the asymmetry factor defined as

$$A = \frac{I_t^{ph}(\sigma^+) - I_t^{ph}(\sigma^-)}{I_t^{ph}(\sigma^+) + I_t^{ph}(\sigma^-)} \tag{2.54}$$

We shall limit ourselves here, for conciseness, to the contribution of the dominant tunnel current from the conduction band.[Eq. (2.41)] Assuming that tunnel transitions preserve the spin, one finds

$$A = \left( \frac{\delta K}{K} + \frac{\delta \rho}{\rho} \right) \frac{\delta n_s}{n_s} \tag{2.55}$$

where the symbol $\delta X$ will denote, throughout this section, the difference of the quantity $X$ for electrons of + and – spin. Recall that $K$ is the tunnel density matrix, $\rho$ is the density of states of the metal and that $\delta n_s / n_s$ is the spin polarisation of electrons tunnelling from the conduction band at the surface.[47]

The model of section III predicts a strong variation of the surface recombination velocity with bias at small distance. Since $\delta n_s / n_s$ is a balance between spin lattice relaxation and recombination in the bulk,[48] this polarisation should also depend on bias. In this section, we evaluate $\delta n_s / n_s$ . Since one assumes that the tunnel current is negligible with respect to the photocurrent, $\delta n_s / n_s$ does not depend on the shape of the metal density of states, determination of $\frac{\delta K}{K} + \frac{\delta \rho}{\rho}$ can be performed independently and will be taken from the literature in Chapter 5.

[47] *If one neglects the spin lattice relaxation in the depletion layer, the electronic spin polarisation should be independent of the energy $\varepsilon_c$ in the depletion layer.*

[48] *I. Favorskiy, D. Vu, E. Peytavit, S. Arscott, D. Paget and A. C. H. Rowe , submitted to Appl. Phys. Lett.*

*V.1 General framework for calculation of the spin currents*

The spin dependence of the tunnel current between surface states and a magnetic surface under injection of spin-polarised photocurrent is summarized in Fig. 2.7 and has already been considered by Jansen et al[49].

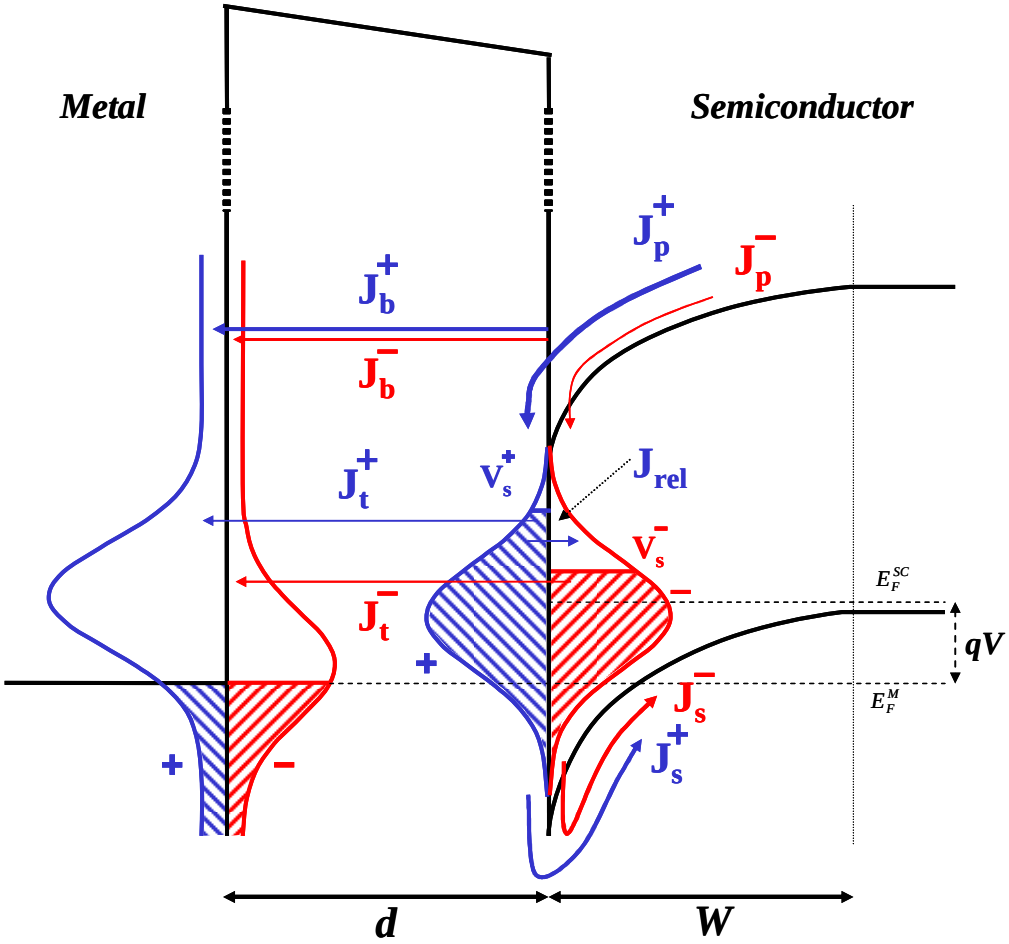


***Fig 2.7**: Diagram of the spin-polarised currents in a ferromagnetic/semiconductor junction under optical excitation. Arrows indicate the electron flow and their widths correspond to the relative magnitudes of the currents. The spin dependence of the tunnel current is determined by the polarisation of the magnetic states of the metal at the energy of injection and by the spin polarisation of electrons at the semiconductor surface.*

This picture considers the + and – spin reservoirs separately so that, because of the distinct concentrations of injected electrons of + and – spin, the quasi Fermi levels of the two electron spins are at distinct positions. This implies that the photovoltage and therefore $\Delta\varphi$ depend on spin.

The current conservation equations, written separately for the two types of spins and neglecting the tunnel current, are

$$J_p^+ + J_s^+ + J_{rel}^+ = 0 \qquad (2.56)$$

[49] *R. Jansen, M. W. J. Prins, H. van Kempen, Phys. Rev. B* ***57****, 4033 (1998)*

$$J_p^- + J_s^- + J_{rel}^- = 0 \tag{2.57}$$

where $J_p^{\pm}$ are the injected photocurrent densities for ± spins, $J_s^{\pm}$ are the Schottky currents and $J_{rel}^{\pm}$ are the losses by spin relaxation. The expression of the Schottky currents is simply, using Eq. (2.9)

$$J_s^{\pm} = J_0 \exp(-\frac{\Delta\varphi^{\pm}}{kT})\left[\exp(\frac{qV_s^{\pm}}{kT}) - 1\right] \approx A^{**}T^2 \exp(-\frac{\varphi_b}{kT}) \tag{2.58}$$

Since the Schottky barrier for holes $\varphi_b = \varphi_0 + \Delta\varphi - qV_s$ this barrier obviously does not depend on the electronic spin one has $\delta J_s = 0$, so that Eq. (2.56) and (2.57) give by difference

$$\delta J_{rel}^s / q + \delta J_p / q = 0 \tag{2.59}$$

*V.2 Expressions for spin injection and relaxation currents*

The model of Sec. III is extended here by considering two spin dependent values $\Delta\varphi^{\pm}$ of $\Delta\varphi$ for the two electronic spins. The spin-dependence of the surface quasi Fermi level position implies a spin dependence of the surface recombination velocity. For an exciting light helicity such that $n_0^+ > n_0^-$, one has $\Delta\varphi^+ > \Delta\varphi^-$ so that $S_+ < S_-$ which further increases the electronic spin polarisation. This spin dependence of the surface recombination is taken into account by taking the derivative of Eq. (2.36) with respect to spin, which gives

$$\frac{\delta S}{S} = -\frac{\delta(\Delta\varphi)}{\varsigma} \tag{2.60}$$

where the energy $\varsigma$ is given by

$$\frac{1}{\varsigma} = \frac{1}{kT} + \frac{\partial D(\Delta\varphi)}{D\partial(\Delta\varphi)} \tag{2.61}$$

For a given initial spin polarisation, the steady-state spin in a given electronic state depends on a balance between spin relaxation in the electronic state and recombination in this state. Thus, the spin-dependence of the surface recombination velocity modifies the polarisation of injected electrons.

The spin polarisation of injected electrons and the spin photocurrents are calculated in Appendix A from a resolution of the spin and charge diffusion equations, using Eq. (2.60) in the boundary condition. The result is

$$\delta n_0 / n_0 = N_{os}\beta_s / N_o\beta + (1 - \beta_s)\delta(\Delta\varphi / \varsigma) / 2 \tag{2.62}$$

where $N_{os}$ and $\beta_s$ are the spin equivalents of $N_o$ and $\beta$ . The first term of this equation can be simplified since, as shown in Appendix (Eq. A.28),

$$\frac{N_{0s}}{N_0} \approx \frac{(g_+ - g_-)}{(g_+ + g_-)} \sqrt{\frac{\tau_s}{\tau}} \frac{Sh(\ell / L\ )}{Sh(\ell / L_s)} \tag{2.63}$$

The corresponding value of the polarisation is within the multiplicative factor $\frac{Sh(\ell / L\ )}{Sh(\ell / L_s)}$, equal to the value $\frac{(g_+ - g_-)}{(g_+ + g_-)} \sqrt{\frac{\tau_s}{\tau}}$ obtained in the case of a large surface recombination for a thin sample. The second term of Eq. (2.62) expresses the increase of the polarisation due to the spin dependence of the surface recombination.

As shown in Appendix B, the spin photocurrent is given by

$$\delta J_p / q = S\delta n_0 - n_0 S\delta(\Delta\varphi / \varsigma) / 2 \tag{2.64}$$

For the expression of the spin relaxation current, we consider the surface states situated in an energy range $d\varepsilon$ at energy $\varepsilon$ above midgap. A fraction $f^{\pm}$ of these states is occupied by ± electronic spins, while a fraction 1- $f^+$- $f^-$ is unoccupied. The relaxation current for these states is given by

$$\delta J^s_{rel} / q = \frac{N_T d\varepsilon}{T_1^s} \left( f^+ - f^- \right) \tag{2.65}$$

where $T_1^s$ is the relaxation time of electronic spins trapped at the surface. For integration over energy, it is considered that states situated at $\Delta\varphi^- < \varepsilon < \Delta\varphi^+$ are fully spin-polarised ($\left| f^+ - f^- \right| = 1$), and that states situated below $\Delta\varphi^-$ are characterized by their polarisation $f^+ - f^-$. This gives

$$\delta J^s_{rel} / q = \frac{N_T \Delta\varphi}{T_1^s} \delta(\Delta\varphi) + \frac{N_T \left( f^+ - f^- \right)}{T_1^s} \int_0^{\Delta\varphi} D(\varepsilon) d\varepsilon \tag{2.66}$$

and finally, Eq. (2.59) becomes

$$S\delta n_0 - n_0 S\delta(\Delta\varphi / \varsigma) / 2 = \frac{N_T \Delta\varphi}{T_1^s} \delta(\Delta\varphi) + \frac{N_T \overline{\Delta\varphi} \left( f^+ - f^- \right)}{T_1^s} \tag{2.67}$$

where

$$\overline{\Delta\varphi} = \int_0^{\Delta\varphi} D(\varepsilon) d\varepsilon \tag{2.68}$$

The quantity $f^+ - f^-$ is calculated in Appendix B. The result is

$$f^+ - f^- = \frac{\sigma_p v_p p_s T_1^s}{\sigma_p v_p p_s T_1^s + 1} \frac{\delta n_s}{n_s} = \gamma \frac{\delta n_s}{n_s} \tag{2.69}$$

so that the spin polarisation in the surface state is the product of the initial polarisation, equal to the polarisation of conduction electrons at the surface, times a dynamic factor $\gamma$ which includes the spin relaxation rate $1/T_1^s$ and the capture rate $\sigma_p v_p p_s$ of valence holes.

Since the width of the space charge layer is much smaller than the electronic spin diffusion length, the argument already made for the charge[50] allows us to assume that the energy of the spin Fermi levels is constant throughout the space charge layer, so that $n_s^{\pm} = n_0^{\pm} e^{\frac{f\varphi_b}{kT}}$ and $\delta n_s / n_s = \delta n_0 / n_0$. Eq. (2.67) finally gives

$$\delta(\Delta\varphi / \varsigma) = \frac{\delta n_0}{n_0} \frac{S T_1^s n_0 - \gamma N_T \overline{\Delta\varphi}}{\frac{1}{2} S T_1^s n_0 + N_T D(\Delta\varphi)\varsigma} \tag{2.72}$$

and

$$\boxed{\frac{\delta n_s}{n_s} = \frac{\delta n_0}{n_0} = \frac{N_{0s}\beta_s}{N_0\beta}\left[1 + \frac{(1-\beta_s)\left(s - \gamma\overline{\Delta\varphi^*}\right)}{\beta_s s + 2\varsigma^* D(\Delta\varphi) + (1-\beta_s)}\right]} \tag{2.73}$$

where the dimensionless parameter *s* is defined by

$$s = S T_1^s n_0 / (N_T kT) \tag{2.74}$$

and $\varsigma^*$ and $\overline{\Delta\varphi^*}$ are the values of $\varsigma$ and $\overline{\Delta\varphi}$ in units of *kT*. The second term of Eq. (2.73) is proportional to $T_1^s$ and represents the effect of the spin-dependent surface recombination. It will be seen in Chapter 5 that this term is negligible with respect to the first one.

## *VI. Conclusion*

The present chapter presents an original picture for describing both the intensity and the spin dependence of the photoassisted tunnel current from a semiconductor into a metal.

For the intensity of the tunnel current, the key equation is the charge neutrality equation, Eq. (2.37). This equation enables one to calculate the shift of the electron quasi Fermi level, $\Delta\varphi$, from which the photovoltage, the surface barrier and the surface recombination velocity are obtained quite simply. The spin dependence of the tunnel current is determined by the asymmetry factor given by Eq. (2.54), where the spin polarisation of the tunnelling electrons is given by Eq. (2.73).

[50] *C. G. B. Garret and W. H. Brattain, Phys. Rev* ***99****, 376 (1955)*

## Chapter 2 : Useful equations

### Charge

*Surface barrier* $\varphi_b = \varphi_0 + \Delta\varphi - qV_s$ (2.8)

*Photovoltage* $qV_s = qV_s^* + \Delta\varphi + kTLog[1-\beta]$ (2.32)

$\beta = (1+S/v_d)^{-1}$ (2.31)

*Electron concentration, surface* $n_s = \frac{A^{**}T^2}{qS}\left[\frac{qSn_0}{A^{**}T^2}\right]^{f^*}$ (2.33)

*beginning of depletion region* $n_0 = \beta\, N_0$ (2.29)

*Recombination velocity* $S = S_0 \exp(-\frac{\Delta\varphi}{kT}) / D(\Delta\varphi)$ (2.36)

*Charge neutrality equation* [ $\delta Q_m + \delta Q_{sc} + \delta Q_{ss} = 0$ ] [Eq. (2.37)]

$$C_m\left[V - V_s^* - \frac{kT}{q}Log(1-\beta)\right] + qW_0N_A\left[\sqrt{\left[\frac{\varphi_b}{\varphi_0}\right]\left[1+\frac{n_s}{N_A}\frac{kT}{\varphi_b}\right]} - 1\right] + qN_T(0)\int_0^{\Delta\varphi} D(\varepsilon)d\varepsilon = 0$$

*Tunnel current from the conduction band*

$J_{tb} = J_{tb}^0 N^*(S)\exp\left(-\frac{\omega qV}{kT}\right)$ (2.41)

$N^*(S) = \frac{A^{**}T^2}{qS}W_0\left[\frac{qSn_0}{A^{**}T^2}\right]^{f+\omega(1-2\alpha f)}$ (2.42)

$\omega = \frac{d}{2d_0}\frac{kT}{\sqrt{\Phi_b^*}}$ (2.43)

*Ideality factor for a forward bias*

$\frac{1}{n} = 1 - \frac{\varepsilon_s/W + q(1-\eta)N_T(0)}{C_m + \varepsilon_s/W + qN_T(0)} - \alpha_d$ (2.45)

($C_m$ is the capacitance of the tunnel gap and $\alpha_d$ accounts for residual processes )

### Spin

*Measured asymmetry factor* $A = \left(\frac{\delta K}{K} + \frac{\delta\rho}{\rho}\right)\frac{\delta n_s}{n_s}$ (2.55)

*Spin polarisation* $\frac{\delta n_s}{n_s} = \frac{N_{0s}\beta_s}{N_0\beta}\left[1 + \frac{(1-\beta_s)\left(s - \gamma\overline{\Delta\varphi^*}\right)}{\beta_s s + 2\zeta^* D(\Delta\varphi) + (1-\beta_s)}\right]$ (2.73)

$s = ST_1^s n_0 / (\, N_T kT\,)$ (2.74)

$\gamma = \frac{\sigma_p v_p p_s T_1^s}{\sigma_p v_p p_s T_1^s + 1}$ (2.69)

$\zeta^* = \left[1 + kT\frac{\partial D(\Delta\varphi)}{D\partial(\Delta\varphi)}\right]^{-1}$ (2.61)

# Chapter 3: Experimental setup for investigation of charge and spin tunnel injection

## *I. Introduction and background*

At the beginning of my Ph.D. work, the existing system (operating in air) was adapted to atomic force microscopy (AFM) and to photo-assisted, spin-unpolarised tunnel experiments. This system, described in Fig. 3.1, was previously used to investigate injection of spin unpolarised photoelectrons from silicon tips into nonmagnetic gold surfaces.[51] The relative position of tip on the surface of the sample is controlled by two piezoelectric tubes. The first tube (#1) modifies the position of the tip on the surface sample while the second one (#2) determines the tip-surface distance. For the laser excitation, we use the collimated output of a polarisation-preserving optical fibre, giving a typical power of 5 mW at 780 nm. This beam is focused onto the rear of the tip to a spot of minimum diameter 20 μm by a lens with $f$ = 23 mm focal length.[52] In addition, a non-polarizing beam splitter is used to direct the laser beam reflected from the cantilever to a quadrant photodiode for AFM measurements.

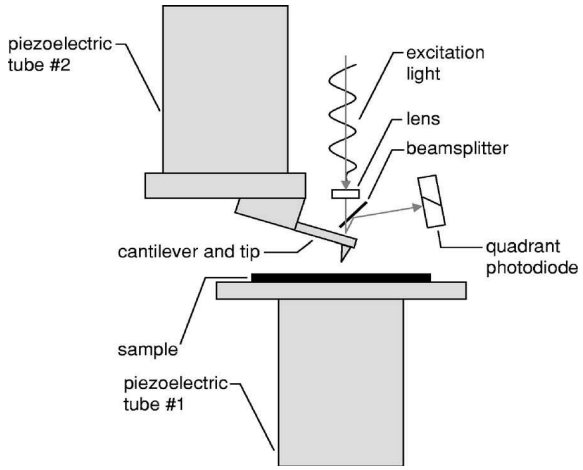


***Fig. 3.1:*** *Spin unpolarised photo-assisted tunnel system*

While the sample is grounded and a bias is applied to the cantilever, a preamplifier monitors the cantilever current, and a conventional feedback system, using proportional and integral settings, enables to stabilize the tip-surface distance in order to obtain a constant

[51] *A. C. H. Rowe and D. Paget, Phys. Rev. B* ***75****, 115311 (2007)*

[52] *The size of the laser spot can be made smaller by decreasing the focal length, but then the lens must be installed between the beam splitter and the cantilever, which strongly reduces the sensitivity of AFM measurements.*

tunnelling current. For the investigation of the photoassisted tunnelling current the experimental procedure is described in Fig 3.2. During a time $T_1$, the tip-surface current is stabilised in the dark at a nominal value $I_{set}$ while a tip bias $V_{set}$ is applied. The relation between $I_{set}$ and the actual current is given in Fig. 3.3. The feedback loop is then opened during an acquisition time $T_2 + T_3$ (with $T_2 = T_3$). During this time, two voltage bias scans are rapidly performed, the first under laser excitation and the second in the dark. A time-resolved current measurement gives the bias dependencies of the tunnel current under light excitation $I_{light}$ and in the dark $I_{dark}$. The difference of these signals gives the tunnel photocurrent, $I_{ph}$. This sequence can be repeated a number of times in order to increase the signal-to-noise ratio (S/N ratio).

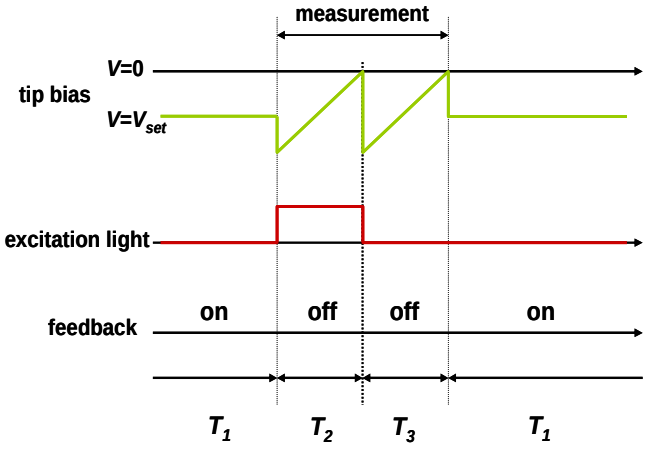


***Fig. 3.2**: Experimental procedure for investigation of spin-unpolarised photoassisted tunnelling. After stabilisation of the tip-surface distance in the dark, the feedback loop is opened and two bias scans are rapidly performed, the first one under laser excitation and the second one in the dark.*

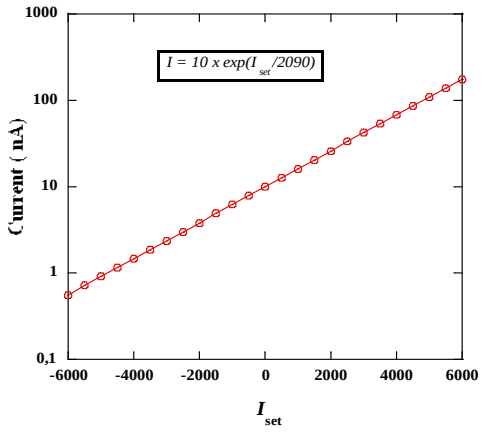


***Fig. 3.3:** Value of the tunnel current imposed by the feedback loop as a function of the parameter $I_{set}$.*

In this chapter, I describe the modifications of the experimental setup required for spin-polarised photoassisted tunnelling measurements.

- Sec. II is devoted to the circular polarisation of the laser and to its switching from $\sigma^+$ to $\sigma^-$.
- Sec. III describes the experimental procedure.
- Sec. IV analyses the application of a magnetic field larger than the coercive field of the magnetic surface under investigation.
- Sec. V and Sec VI discuss respectively the technological aspects for cantilever and sample fabrication.

## *II. Controlling the polarisation of the excitation light*

For spin injection investigations, it is necessary to switch the circular polarisation of the laser from $\sigma^+$ to $\sigma^-$. Since relatively small spin dependent effects are expected, great care has been taken in order to have as perfect and as symmetric as possible helicities of the laser. We have chosen to insert into the laser beam a longitudinal KD*P Pockels cell (Linos CPC12). This cell (PC) of length 2 cm, has a quarter wave voltage of the order of 2500 V at the energy of excitation. The high voltage of the PC, applied between the top and bottom windows of the cell, is delivered by a home made power supply and can be switched by a TTL level between two independently adjustable values. The experimental setup is shown in Fig. 3.4.

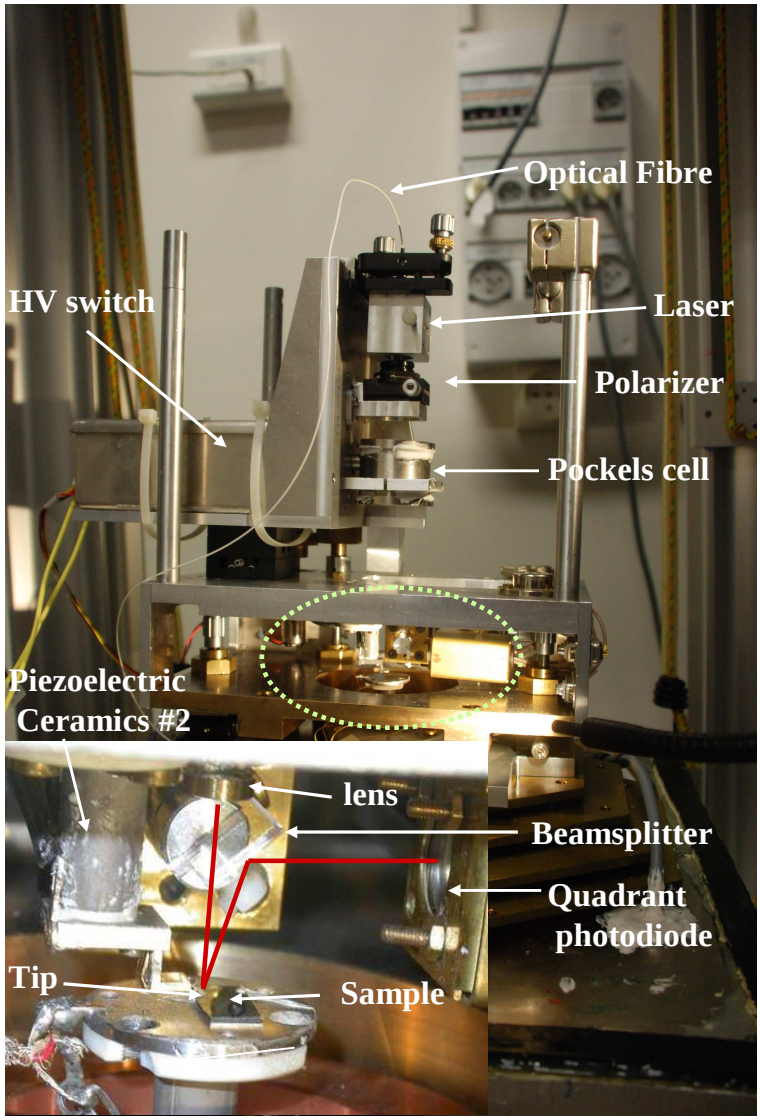


***Fig. 3.4:*** *Experimental setup for tunnel injection.*

This figure shows the laser head, the PC and the switch for the high voltage of the Pockels cell. In order to avoid electromagnetic parasites, the switch, the Pockels cell and the cables between the two are carefully shielded by a grounded permalloy box. Also shown in the figure is a linear polariser cube used to fix the polarisation of laser beam at the entrance of the PC.

*II.1 Aligning the PC:*

In the absence of an applied voltage, the PC is a uni-axial crystal with the direction z of light propagation as its axis. As described in Fig. 3.5, a voltage $V_z$ is applied between the two faces via transparent electrodes. Under the effect of this electric field along the z direction, the PC becomes a biaxial crystal with two principal axes denoted as *x* and *y*. One considers the case when the laser is not perfectly aligned with the PC axis.

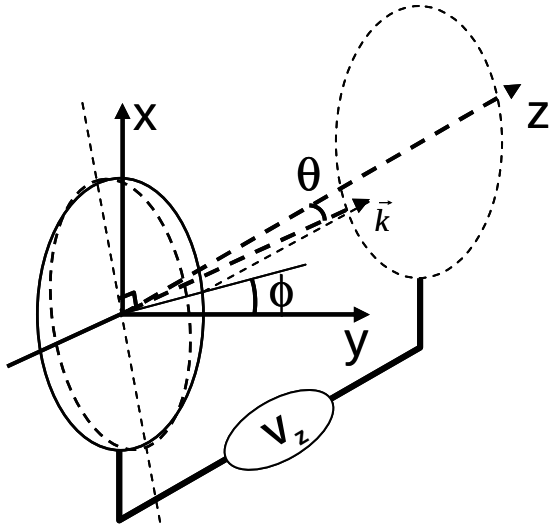


***Fig 3.5:*** *Representation of the Pockels Cell for which the bias is applied between the front and the back faces. The misalignment of the incident laser beam with respect to the crystal axis is characterized by* $\theta$ *and* $\phi$**.** *The dashed ellipse represented in the entrance plane is the cross section of the index ellipsoid by the plane orthogonal to the wave vector* $\vec{k}$**.** *Its principal axes are rotated by an angle* $\alpha$ *given by Eq. (3.7).*

The refractive indices along x and y are[53]

$$n_x = n_0 + \Delta n^{eo}$$
$$n_y = n_0 - \Delta n^{eo} \qquad (3.1)$$

Here, $n_0 =$ 1.5001 is the ordinary index of refraction and $\Delta n^{eo}$ given by

$$\Delta n^{eo} = \tfrac{1}{2} n_0^3 r_{63} V_z / L \qquad (3.2)$$

[53] *T. Dartigalongue and F. Hache, J. Opt. Soc. Am. B* ***20****, 1780 (2003)*

is the electro-optic birefringence which depends on the electro-optic coefficient $r_{63}$ ($r_{63}$ = 25 x $10^{-12}$ m/V for KD*P). For a PC of length $L$ = 20 mm and for a excitation wavelength ($\lambda$=780nm), the phase shift between the x and y polarised light is

$$\Delta\varphi = 4\pi\Delta n^{eo}(L/\lambda) = 2\pi n_0^3 r_{63} V_z / \lambda \tag{3.3}$$

For the production a $\sigma^+$ and $\sigma^-$ circularly-polarised light, one must have an incident light polarised along the bisector of x and y and $\Delta\varphi$ =±π/2, from which one finds $\Delta n^{eo} \approx 10^{-5}$ and a voltage $\pm V_{\lambda/4}$ where

$$V_{\lambda/4} = \lambda/(4{n_0}^3 r_{63}) \tag{3.4}$$

equals to 2.35 kV for KD*P. As seen in Fig. 3.5, the components of the laser wave vector k are

$$\begin{aligned} \mathrm{k_x} &= k_0 \sin\theta\cos\phi \\ \mathrm{k_y} &= k_0 \sin\theta\sin\phi \\ \mathrm{k_z} &= k_0 \cos\theta \end{aligned} \tag{3.5}$$

where $\phi$ is the angle of the projection of $k$ in the xy plane with respect to the y direction. It can be shown that,[54] to first order, the principal axes of the PC are rotated with respect to x and y by an angle,

$$\alpha = \frac{\Delta n^n}{4\Delta n^{eo}}\theta^2 \frac{k_x k_y}{k_0^2} \tag{3.6}$$

and the modified phase shift is given in a way similar to Eq. (3.3). In this case, the optical index in the z direction, given by $n_z = n_0 + \Delta n^n$ where $\Delta n^n$ is the natural birefringence of KD*P will play a role. The polarisation of the output beam for an incident beam at angle $\theta$ with the z direction can be calculated quite simply.

$$\Delta\varphi^{eff} = 4\pi\Delta n^{eff}(L/\lambda) \tag{3.7}$$

where $\Delta n^{eo}$ is replaced by

$$\Delta n^{eff} = 2\Delta n^{eo} + \Delta n^n \theta^2 \cos(2\phi) \tag{3.8}$$

Since $\Delta n^n \approx 0.04$ is about three orders of magnitude larger than $\Delta n^{eo}$,[54] it is crucial that the alignment be perfect. In the general case of an input beam for which the linear polarisation is misaligned by an angle $s$ with respect to the bisector of the axis x and y, the misalignment

[54] *T. Dartigalongue and F. Hache, J. Opt. Soc. Am. B* ***20****, 1780 (2003)*

with respect to the modified principal directions is $s-\alpha$. The electric field of the input beam can be written, omitting the $e^{i\omega t}$ factor

$$E_{in} = \cos\left(\frac{\pi}{4}+s-\alpha\right)\hat{x}_\alpha + \sin\left(\frac{3\pi}{4}+s-\alpha\right)\hat{y}_\alpha \tag{3.9}$$

where $\vec{x}_\alpha$ and $\vec{y}_\alpha$ are the unit vectors along the modified principal axis. For $V_z^{\pm} = \pm V_{\lambda/4}$, the phase shift, given by Eq. (3.7) (3.8) and (3.4), is equal to [55]

$$\Delta\varphi^{eff\pm} = \frac{\pi}{2}\frac{V_z^{\pm}}{V_{\lambda/4}} + 4\pi\frac{L}{\lambda}\Delta n^n\theta^2\cos\left(2\phi\right) = \pm\frac{\pi}{2} + 2\delta^{\pm} \tag{3.10}$$

This polarisation is defined by the following electric field

$$E_{out}^{\pm} = \hat{e}_{L,R} + \left(\pm\alpha - s - i\delta^{\pm}\right)\hat{e}_{R,L} \tag{3.11}$$

where $\hat{e}_{L,R}$ and $\hat{e}_{R,L}$, given by $\hat{e}_{L,R} = \left(1/\sqrt{2}\right)\left(\hat{x}_\alpha + i\hat{y}_\alpha\right)$ and $\hat{e}_{R,L} = \left(1/\sqrt{2}\right)\left(\hat{x}_\alpha - i\hat{y}_\alpha\right)$ correspond to circularly-polarised light of right and left helicities. The polarisation of the output beam is left(right) circular with a small right(left) component arising from the misalignment. The rates of admixtures $\pm\alpha - s - i\delta^{\pm}$ must be complex conjugates, implying that

$$0 = \alpha = \frac{\Delta n^n}{2\Delta n^{eo}}\left(k_x k_y / k_0^2\right) \approx \frac{\Delta n^n}{4\Delta n^{eo}}\theta^2\sin(2\phi) \tag{3.12}$$

$$0 = \delta^+ + \delta^- \approx \frac{L}{\lambda}\Delta n^n\left(k_x^2 - k_y^2\right) = 0 \tag{3.13}$$

otherwise parasitic intensity modulation effects due to polarisation-dependent reflexions or transmissions will be present at the cantilever. These two equations suggest several important comments. Because of absence of the angle *s* the PC does not need to be perfectly at 45°. In the same way, $\Delta n^{eo}$ does not appear in Eq. (3.13) so that the exact value of the applied voltage is not so important. The only important feature determining the asymmetry is the alignment of the laser beam with respect to the z axis which introduces non zero values of α (Eq. 3.6) and values of $\Delta\varphi^{eff} - \Delta\varphi$ proportional to $(\Delta n^n / \Delta n^{eo})\theta^2$. It is therefore important to minimise $\theta$ to less than a very small fraction of $\sqrt{\Delta n^n / \Delta n^{eo}} \approx 10^{-2}$.

[55] *The quantity $\delta^{\pm}$ (- $\delta^{\pm}$) is the phase shift for light along x (y), which gives using Eq. (3.1) the factor 2 in the value of $\Delta\varphi^{eff\pm}$*

*II.2 Optical alignment procedure*

Shown in Fig. 3.6 is the alignment procedure, taking for clarity a horizontal laser beam. One uses a polariser at 45° to the PC axis, a diffusive plate and an analyzer crossed with the polariser. The role of the diffusive paper is to give rise to a large range of wave vector directions, defined by $\theta$ and $\phi$. As shown in the figure, when $V_z = 0$, one observes on a screen placed at some distance a series of concentric dark circles as well as a dark cross.

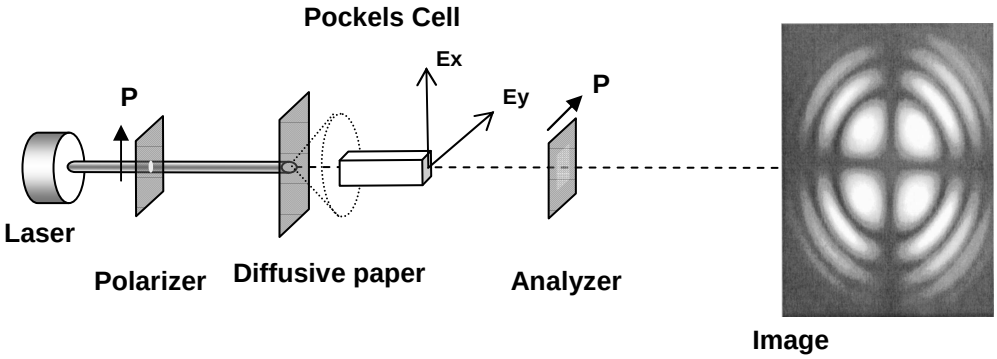


***Fig. 3.6:*** *Optical alignment procedure of the PC. The linearly polarised laser after being diffused by a paper gives an image which reveals the axes of the PC. [After Ref. (56)]*

In the case where $\Delta n^{eo} = 0$, Eq. (3.8) shows that the principal directions of the cell for a given beam are at $\phi$ and $\phi + \pi/2$ and that the birefringence is $\Delta n_{V=0}\theta^2$. The dark cross corresponds to directions for which the polarisation direction ($\phi$ =0 and $\phi + \pi/2$ =0) coincides with the principal axis of the cell, so that the polarisation is not modified by the PC. The concentric circles correspond to beams for which the phase shifts $4\pi\frac{L}{\lambda}\Delta n_{V=0}\theta^2$ are multiples of $2\pi$ so that these beams are also blocked by the analyzer.

By placing the direct laser beam at the centre of the dark cross and dark circles, one can achieve $\theta$ smaller than several $10^{-3}$. Once the laser beam has been aligned with the PC, one removes the diffusive paper in Fig. 3.6 and starts to measure the intensity after the analyser.

The principal polarisation directions of the PC are then determined by looking for the direction of the linear polarisation of the incident light such that the intensity after the analyser does not depend on the PC voltage. One finds two perpendicular directions coinciding with the x and y axis.

[56] *T. Dartigalongue and F. Hache, J. Opt. Soc. Am. B* ***20****, 1780 (2003)*

The polariser is then rotated by 45°, so that the polarisation vector of the laser beam coincides with the bisector between two principal axes.[57] For an arbitrary value of $V_z$, the polarisation of the output beam is elliptic and the measured intensity depends on the angle of the analyzer. When the total electro-optic dephasing is $\pm\pi/2$, i.e. when $V_z$ is equal to the quarter wave voltage the polarisation is circular and the intensity is independent of analyser angle. Finally, in order to decrease the ellipticity of the output light, the whole procedure is iterated, thus completely optimising in turn the parameters $\theta, \phi$ and the quarter-wave voltages.

The quality of the circular polarisation of the exciting light, obtained after completing the above procedure is finally evaluated by continuously turning the analyzer and by calculating

$$P = \frac{I_{\max} - I_{\min}}{I_{\max} + I_{\min}} \tag{3.14}$$

where $I_{max}$ and $I_{min}$ are the observed intensity extremes. $P$ = 0 when the exciting light is perfectly circularly polarised and $P$ = 1 if the polarisation is linear. One can approximately decompose the elliptic polarisation into a combination of left and right circular polarisations. The electric vector which responds to the polarisation of the light can be rewritten

$$E = \begin{pmatrix} (1+\varepsilon)\cos(\omega t) \\ (1-\varepsilon)\sin(\omega t) \end{pmatrix} = \sigma^{+} + \varepsilon\sigma^{-} \tag{3.15}$$

where $\varepsilon = P^2$ . (3.16)

| λ(nm) | HV(kV) | $I_{max}$(mW) | $I_{min}$(mW) | $P$ | $\varepsilon$ |
|---|---|---|---|---|---|
| 780 | -2.45 | 16.35 | 15.75 | 1.8% | 0.03% |
| | 0.01 | 33.5 | 0.01 | 99% | 99% |
| | +2.5 | 16.2 | 15.9 | 2.8% | 0.08% |
| 635 | -2.07 | 17 | 16 | 3% | 0.09% |
| | 0.09 | 30 | 0.01 | 99% | 99% |
| | +1.92 | 17 | 16 | 3% | 0.09% |

***Table 3.1:*** *The quarter wave voltage for two different wavelengths and their polarisation properties.*

Table 3.1 summarizes the values of $I_{max}$ and $I_{min}$ obtained at the end of the alignment procedure for λ = 780 nm and also for λ = 635 nm. The obtained quarter-wave voltages are indeed proportional to λ. Also shown in the table are the values of $P$ and $\varepsilon$. The polarisation of the exciting light at the rear of the tip could be slightly different from the above values because of the diffraction of the light passing through the lens. However, the asymmetry of

[57] *Slight errors in this setting correspond to nonzero values of s in Eq. (3.10) and produce an ellipticity of the final polarisation which is the same for the positive and negative values of the high voltage.*

the effective light ellipticity between the two optimal settings, of $\varepsilon^+ - \varepsilon^- \approx 10^{-4}$, is well below expected spin signals.

## *III. Electronic control system and experimental procedure:*

The overall scheme for the control electronics for the injection experiment is shown in Fig. 3.7. It is composed of a generator fabricating a voltage ramp and a synchronisation signal used for driving the laser power supply, the switch of the PC, the feedback system and for generating the voltage applied to the cantilever for I(V) curves. The corresponding control signals are generated by an in-house made module, also shown in this figure.

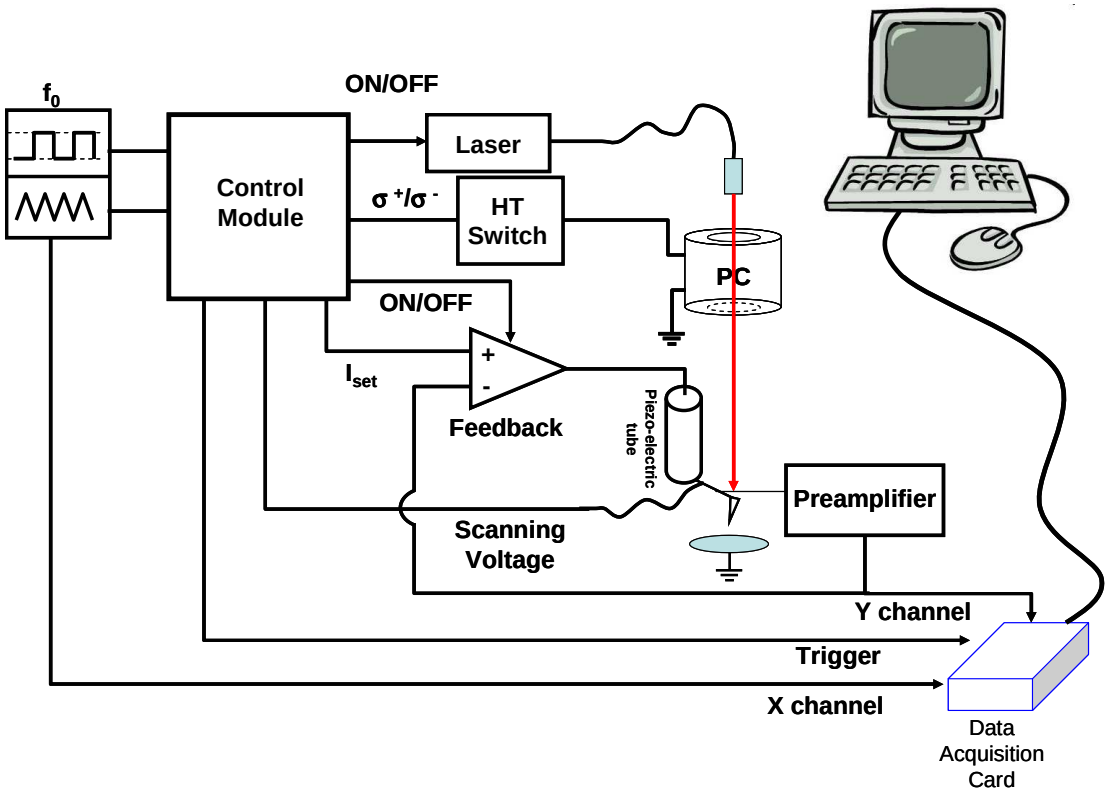


***Fig. 3.7:*** *Electrical configuration for injection experiments.*

The experiment is controlled as described in Fig. 3.8. For spin injection, one uses two acquisition cycles of the type shown in Fig. 3.2, one for $\sigma^+$-polarised light, one for a $\sigma^-$ polarisation. At the top of the figure is the triangular voltage ramp applied to the cantilever, at frequency $2f_0$,[58] as well as two synchronisation signals at respective frequencies

[58] *The injection processes described in Chapter II are observed under reverse bias, by applying a negative bias to the cantilever.*

$f_0$ and $f_0/2$. The two measurement cycles, defined by the signal disabling the feedback loop, are separated by an adjustable time, larger than the time constant of the feedback loop, during which the feedback loop is closed. In the same way as for Fig. 3.2, a constant, adjustable voltage $V_{set}$ is applied to the cantilever when the feedback loop is on. As a result, the cantilever bias must be switched between the ramp and $V_{set}$ over the acquisition cycle. The laser beam is on during the first ramp of each acquisition cycle, and off during the stabilisation time when the feedback is on.

Note finally that the switching of a high voltage, as high as ±2.4kV, will inevitably generate an electro-magnetic field and also induce disturbances because of the small value of the tunnelling current. As shown in Fig. 3.8, to minimize the disturbance, this switching defined by the change of the TTL level controlling the HV switch, occurs after the end of each measurement cycle, so that any resulting parasitic signal occurs when no data acquisition takes place.

For most experiments described in this thesis, the frequency $f_0$ was adjusted to a value between 40 Hz and 70 Hz. Experimentally, changing the cantilever voltage to higher frequencies induces an error signal at the output of the preamplifier, which is likely to be large when the sign of the voltage scan is reversed. This signal may alter the feedback control and generate artefact data at the beginning of the voltage sweep. On the other hand the acquisition frequency should be sufficiently high so that the overall measurement is performed faster than the characteristic time of possible instabilities of the tunnelling current.

The difference signal from the quadrant photodiode shown in Fig. 3.1 was also monitored in an independent acquisition channel. This signal allows us to characterise mechanical contact.

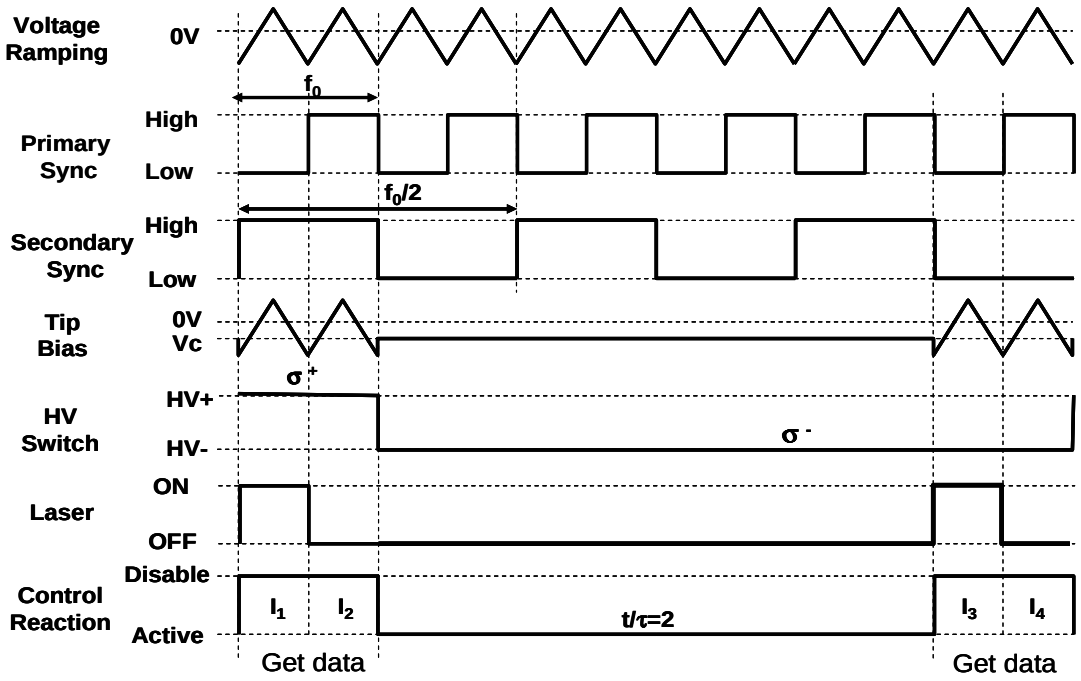


***Fig. 3.8:*** *Timing diagram of electric components.*

## *IV. Application of a magnetic field:*

As mentioned at the beginning of this chapter, the configuration of our system requires a magnetic field in order to reverse the surface magnetisation of the sample under investigation. Experimentally, the coercive field of the samples investigated here is of the order of 200 G. Application of this magnetic field should not induce any parasitic motion since the whole system is made of non magnetic materials.

Because of the small space available and in order to minimize the heating of the piezoelectric tube, it was decided to use a magnetic core placed inside the piezo-electric tube (#1). As described in Fig. 3.9, this magnetic field is created by a remote coil of 3500 turns and of resistance 100 Ω and guided to the sample by a soft iron core.

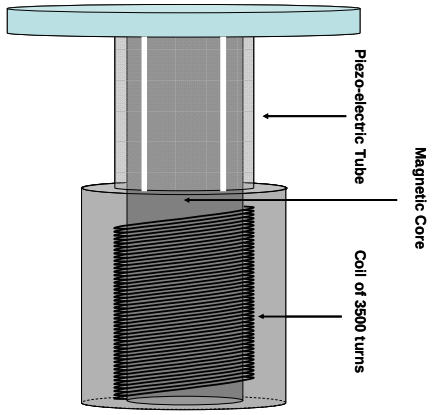


***Fig. 3.9:*** *Magnetic source installed in the injection experiment. The coil is separated from the sample plate because of the piezo-electric tube. The magnetic field is guided to the sample holder by a soft iron core.*

In the left panel of Fig. 3.10 the magnetic fields at different distances to the sample holder surface are shown. The reduction of the field with the distance ensures that the magnetic field makes a reduced effect on the electronic or mechanic components of the system. Experimentally, the thickness of a sample is around 1 mm. As shown in the left panel of Fig. 3.10 for a distance *d* from the top of the soft iron core equal to 2 mm, one can create a magnetic field up to 600 G by a current of 0.9 A to the coil.

When such high power is dissipated in the coil, the heat generated could induce a significant thermal expansion of the piezo-electric tube, possibly larger than the capacity of the feedback control system. As a result, this current should be passed only over a limited time otherwise drift effects such as those shown in the right panel of Fig. 3.10 occur. In the first 100 s, i.e. before application of the magnetic field, the current is stable under the effect of the feedback loop. The *start point* in this figure is the moment when the current is passed through the coil. As little as 20 s later, the stability of the system vanishes and after 50 s the feedback control is out of function. Because of this, we have chosen to apply the current for times less than 20 s.

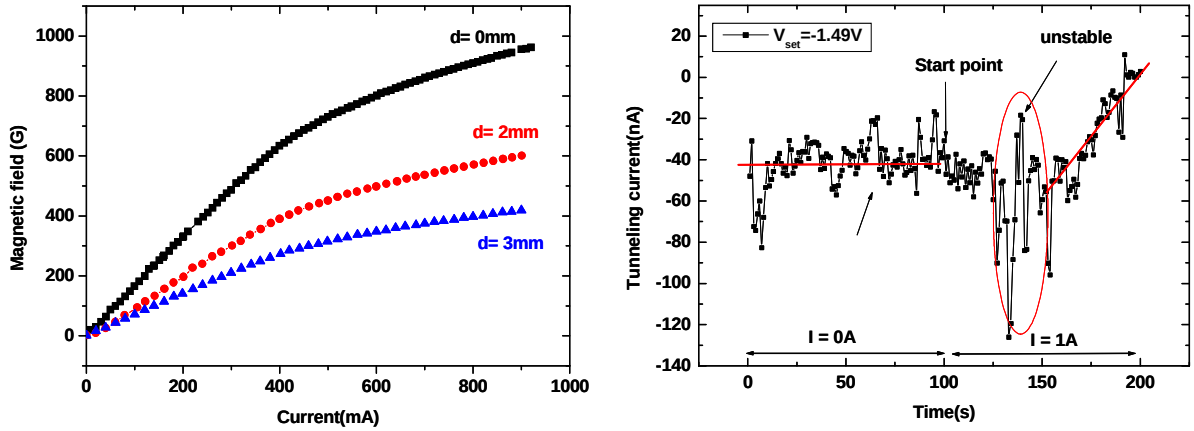


***Fig. 3.10:*** *Magnetic field calibration: (Left) Magnetic field as a function of distance to the magnetic core; (Right) the time variation of the tunnel current due by thermal effects when a 1A current is applied through the coil.(feedback off)*

## *V. Cantilever fabrication*

In Chapters 4 and 5, I have used tipless GaAs cantilevers fabricated by S. Arscott et. al.[59] at the Institut d'Electronique et de Microélectronique et de Nanotechnologie (Lille). These cantilevers are shown in Fig. 3.11. They consist of thin (3µm) GaAs patches of $p^+$ GaAs, fixed on silica substrates. These substrates are metallized so that an ohmic contact can be established to the patch.

[59] *S. Arscott, E. Peytavit, D. Vu, A. C H Rowe and D. Paget, Journal of Micromechanics and Microengineering,* ***20****, 025023 (2010)*

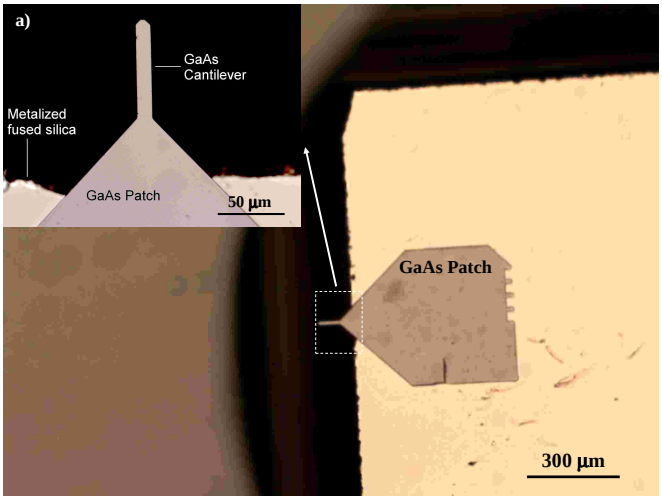


***Fig. 3.11:*** *Images of a GaAs microcantilever on a silica support.*

The process used to fabricate the microcantilever is shown in Fig.3.12:

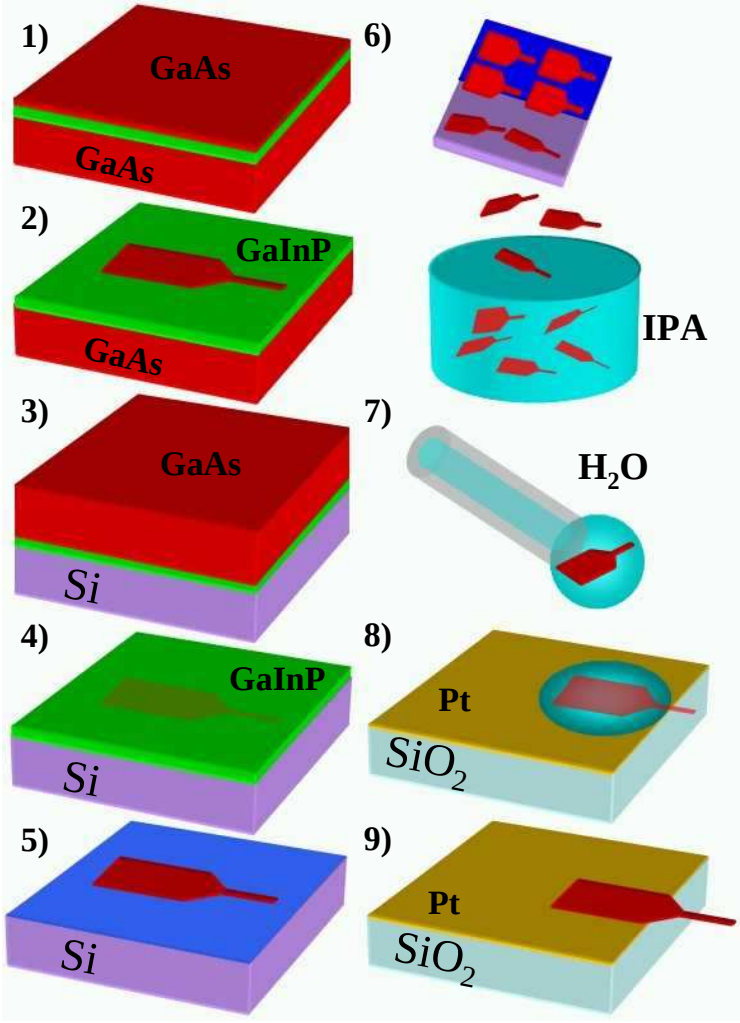


***Fig. 3.12:*** *Fluidic assembly process sequence for the fabrication of the hybrid MEMS microcantilevers:1) Epitaxial growth of a GaAs/GaInP heterostructure; 2-6) free pre-patch GaAs definition; 7-9) Fluidic manipulation and assembly onto a Pt-coated metallised silica support*[1].

First, (Stage 1) an epi-ready semi-insulating GaAs wafer (2 inch diameter, orientation (100)) is used to grow a 100nm thick layer of non-intentionally doped lattice-matched $Ga_{0.51}In_{0.49}P$ at 520°C. The future cantilever is then grown on top of this GaInP layer, as a layer of 3µm carbon-doped at $\approx 10^{18} cm^{-3}$ GaAs. In Stage 2, photolithography and wet etching are then used to pattern the 3µm thick GaAs layer.

Stages 3 to 6 lead to liberation of patches into a solvent.

Stage 3 and 4: After being turned upside down, the wafer surface is glued to another silicon substrate by another photoresist. The back GaAs substrate now is on top of the structure. The back GaAs substrate is then completely removed. At this stage, as shown in Fig. 3.13, the densely packed mesa patches can be observed from underneath the 100*nm* thick GaInP layer.

Stage 5 and 6: The GaInP layer is removed. This etch is selective to the GaAs mesa and leaves then embedded in the photoresist adhesion layer. The patches are finally liberated by dissolving the photoresist bonding layer.

Finally, using micropipettes, a single patch is removed from the solution and placed onto the edge of a rectangular metallized silica support, along with a drop of liquid. The samples are then annealed in order to achieve an ohmic contact between the patch and the metal.

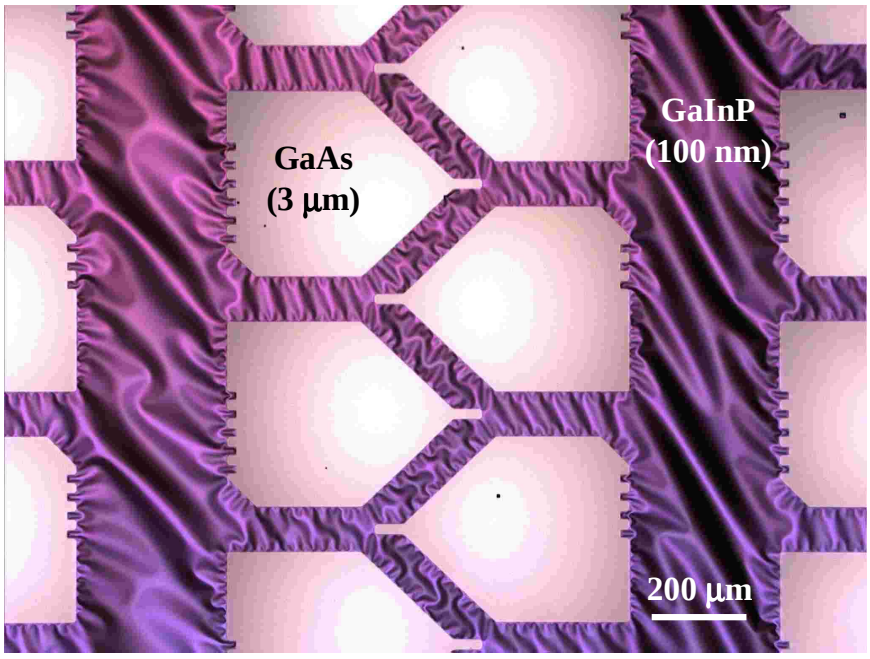


***Fig. 3.13:*** *Densely packed GaAs patches observed underneath the thin GaInP layer after back etching of the GaAs substrate.*

## *VI. Preparation of metallic and magnetic films*

For the charge injection studies described in Chapter 4, I have used a (nonmagnetic) gold surface since its density of empty states is independent of energy. The film was deposited electrochemically onto silicon substrates and the surface roughness is on the atomic scale.[60]

For investigating spin injection the spin polarisation of the photoelectrons, parallel to the direction of light excitation, is perpendicular to the surface of the sample. This means that only samples with out-of-plane magnetisation can be used to investigate the spin dependent tunnelling injection. Experimentally, another requirement of the sample magnetic behaviour is that the coercivity be in the range of the magnetic field produced by the system.

I have chosen thin (4 to 8 monolayers) cobalt films electrochemically deposited on gold, as described by P. Prod'homme *et al.*[61] Since our system operates in air, in order to avoid the contamination which would oxidize the cobalt film and destroy the magnetism, the sample is passivated by a carbon monoxide layer. This passivation has been found by Math *et. al.* not to destroy the magnetic properties.[62]

The fabrication procedure is described in Fig. 3.14. First, a ~60 ML (14 nm) thick Au (111) buffer layer was electrodeposited onto an H-terminated Si (111) substrate under potentiostatic mode at -2 V. The substrate is then mounted in another electrochemical cell to epitaxially grow a continuous Co(0001) layer. Fig. 3.14 shows the voltage and current variations as a function of time in the cell during growth.

[60] *S. Warren, P. Prod'homme, F. Maroun, P. Allongue, R. Cortes, C. Ferrero, T. –L. Lee, B. C. C. Cowie, C. J.Walker, S.Ferrer, J. Zegenhagen, Surf. Sci.* ***603****, 1212 (2009)*

[61] *P. Prod'homme, F. Maroun, R. Cortes, P. Allongue, J. Hamrle, J. Ferré, J.P. Jamet, N. Vernier, J. Magn. Magn. Mater.* ***315****, 26 (2007)*

[62] *C. Math, J. Braun, and M. Donath, Surf. Sci.* ***482-485****, 556 (2001)*

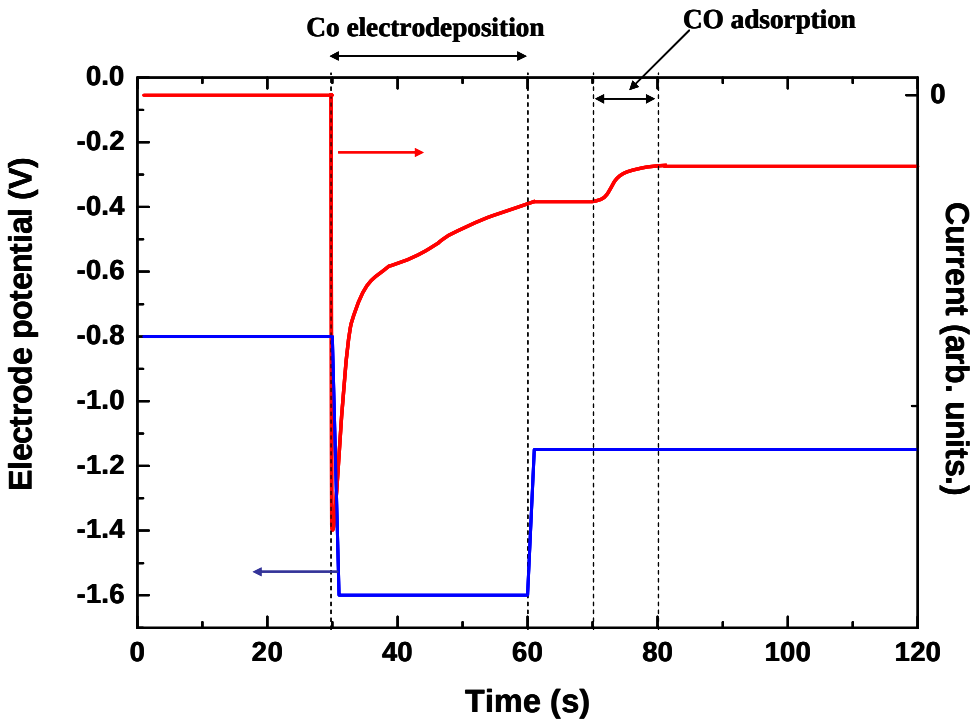


***Fig. 3.14:*** *Electrode potential (bottom curve) and current (top curve) as a function of time during the fabrication of a Co/Au sample.*

At the beginning of the procedure a constant potential of -0.8 V is fixed on the electrode. A potential of -1.6 V is then applied on the electrode for 30 s in order to deposit a 4 ML-thick Co layer. At the end of the deposition, the electrode potential is ramped to -1.15 V, where Co neither grows nor dissolves and the current is constant. When the potential is still maintained in the stabilisation level, CO is bubbled through the cell. The presence of an adsorbed CO layer on the surface reduces the current until the CO covers the entire surface.

The hysteresis loop of a sample fabricated by the above process was measured using the Magneto-Optical Kerr effect. In this experiment the polarisation rotation of linearly polarised laser beam reflected off the sample surface is monitored as a function of the applied perpendicular magnetic field.[63] This rotation is formally equivalent to the precession of the electric field vector of the light around the magnetisation vector of the surface.[64] Typical results for the as-prepared Co thin films are shown in Fig. 3.15. The magnetisation is found perpendicular to the surface plane, with a coercive field is found to be around 200 Oe, within reach of the experimentally accessible fields on the injection experiment.

[63] *K. Sato, J. Phys. Soc. Jpn.* ***43****, 719 (1977)*
[64] *P. Bertrand, C. Hermann, G. Lampel, J. Peretti and I. Safarov, Phys. Rev. B* ***64****, 235421 (2001)*

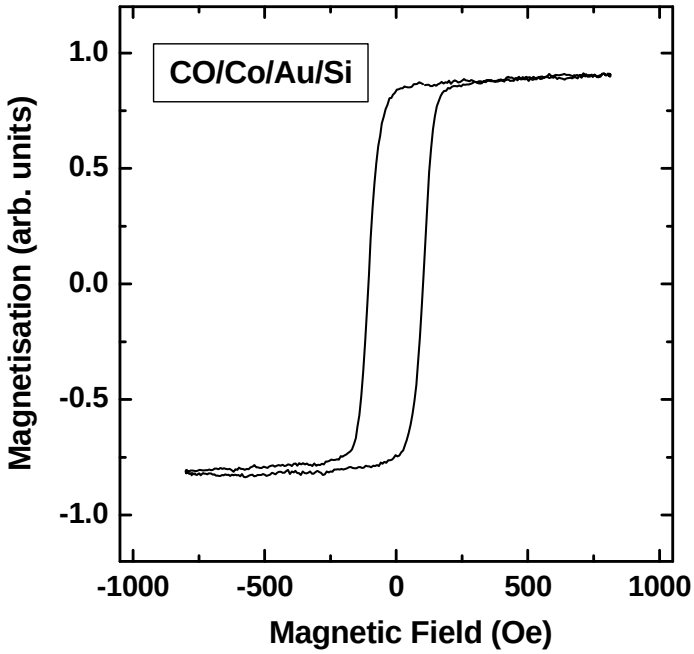


***Fig. 3.15:*** *Normalized hysteresis loop measured for a CO/Co(4.6ML)/Au(30ML)/Si sample, showing the magnetisation perpendicular to the surface.*

## *VII. Conclusion*

In this chapter, I have presented the setup and configuration of the experiment for spin and charge injection as well as an analysis showing that spin-polarised effects can be detected to within a fraction of a percent.

Four key points have been discussed:

-The alignment of the PC is crucial because of the large longitudinal birefringence. Even a slight misalignment of the laser can affect the spin polarisation of the injected photoelectrons. We have obtained an ellipticity of the exciting light and an asymmetry of this ellipticity for $\sigma^+$ and $\sigma^-$ less than 0.1%. This value is much smaller than expected spin-dependent tunnelling signals.

- The electronic control system for the experiment.

- A magnetic field larger than the coercive field of the sample is created in a transient way by a current up to 1 A passing through a coil for at maximum time of 20 s in order to minimize the heat generated by the coil.

- The technology for the fabrication of the cantilever and of the metallic and magnetic surfaces has been discussed. The experiments reported in Chapters 4 and 5 will be performed (respectively) on non magnetic gold surfaces and on magnetic cobalt thin films for which the magnetisation is perpendicular to the surface.

# Chapter 4: Photoassisted tunnelling into nonmagnetic metals

## *I. Introduction*

The purpose of this chapter is to analyse the mechanisms of photoassisted tunnel injection from GaAs thin films (without tips) into metals. The understanding of these mechanisms is crucial in order to clarify the spin injection process described in Chapter 5.

In order to aid the interpretation of the spin dependent experimental results on Cobalt, I chose to first investigate injection into (nonmagnetic) gold films for which the density of empty states is nearly independent of energy. Again, the use of a tipless cantilever simplifies the interpretation of the results since the injection geometry is planar and electric field focussing effects are avoided. On the other hand, contact between the metallic surface and the tipless cantilever could induce lateral variations in the tunnelling distance. It will be seen below that these variations can be characterised and consequently corrected for.

I have investigated the dependence of the tunnel photocurrent as a function of bias, cantilever/surface distance and excitation light power. This dependence is analysed using the model of Chapter 2. Unlike the Nijmegen model,[65] the tunnel photocurrent is found to originate from conduction electrons. Its bias dependence at large distance is caused by the bias dependence of the tunnel gap while at short distances it is due to a change of the surface recombination velocity induced by the unpinning of the surface Fermi level. These results and their interpretation have been recently submitted for publication.[66]

The outline is as follows.

- In Sec. II, I present the experimental results obtained on gold surfaces with the tipless cantilevers described in Chapter 3.
- Sec. III is devoted to the interpretation.
- Sec. IV is a discussion of the validity of the approximations.

## *II. Experimental results on nonmagnetic gold surfaces*

### *II.1 Experimental results*

Photoelectron injection was investigated using the procedure described in Fig. 3.2. The bias $V_{set}$ was -1.5 V. This was performed as a function of $I_{set}$ which, according to Fig. 3.3,

---

[65] *R. Jansen, M. W. J. Prins, and H. van Kempen, Phys. Rev. B* ***57****, 4033 (1998)*

[66] *D. Vu, S. Arscott, E. Peytavit, R. Ramdani, E. Gil, Y. André, S. Bansropun, B. Gérard, A. C. H. Rowe, and D. Paget, submitted to Phys. Rev B.*

determines the dark current at $V = V_{set}$. For the results presented below a total number of 20 measurements was performed. For each measurement the results of 10 acquisition cycles, as defined in Chapter 3, were averaged thereby corresponding to a total measurement time of 2 s at a frequency of 40 Hz. As stated in Chapter 3, the signal from the quadrant photodiode and the tunnel current were measured in parallel. Subsections 1-4 are devoted to the explanation of the various results, while Subsection 5 presents a correlated analysis of these results.

For the present experiment operating in air the chemistry of the interface is not well-controlled and as such, the tunnel current from silicon tips into gold surfaces has been found to exhibit instabilities. These instabilities have been interpreted as due to a change in thickness of the silicon oxide covering the tip due to incorporation or removal of single molecules in the tunnelling gap[67] and give rise to well-defined multi-valued tunnelling currents. For this reason, we first show the bias dependences of tunnel current and tunnel photocurrent with an emphasis on interscan repeatability of the signal.

The results for $I_{set}$ = -2500 are shown in Fig. 4.1. The top panel shows multiple dark current scans in black[68] with the total tunnelling current under light excitation in red. Along with the dark current, the tunnel photocurrent, defined as the difference between the two, is shown in logarithmic units in the bottom panel of the figure (red curves). For a reverse (negative) bias the tunnelling photocurrent corresponds, as described in Chapter 2, to the injection of minority carriers and gives rise to an exponential bias dependence of the tunnelling current. In forward bias the dark current is due to injection of holes while the positive tunnel photocurrent is due to an increase of this current caused by the presence of the photovoltage. The tunnel photocurrent is zero at a bias of about 0.25 V which is generally taken to be the photovoltage. The fluctuations of the tunnel photocurrent from one scan to the other are of the order of 10 %. The large majority of the scans is coincident and corresponds to a fixed exponential behaviour although there is some variation at small bias values. Note that the variation in the tunnel photocurrent is larger than that observed in the dark current scans because feedback stabilisation is performed using the dark current.

[67] *A. C. H. Rowe and D. Paget, Phys. Rev. B* ***75****, 115311 (2007)*

[68] *Because of a preamplifier offset which was subtracted in Fig. 4.2, the measured value of the dark current at V = $V_{set}$ does not correspond exactly to the one obtained from Fig. 3.3.*

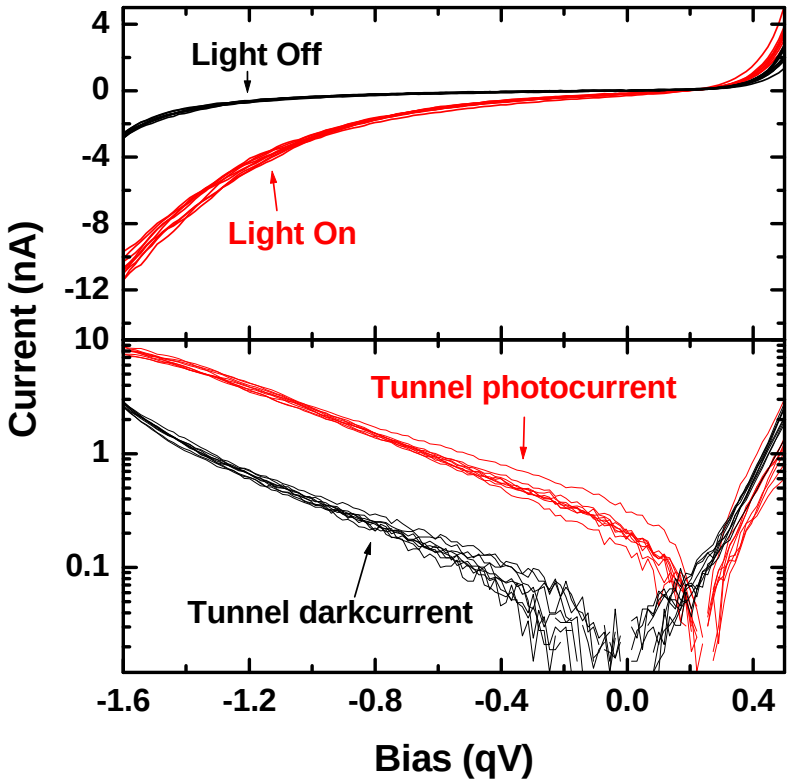


***Fig. 4.1:*** *The top panel shows the bias dependence of the dark tunnel current (black lines) and the tunnelling current under light excitation (red lines) obtained for $I_{set}$ = -2500. The bottom panel shows in logarithmic units the absolute values of the tunnel photocurrent (red lines), defined as the difference between the two, and of the tunnelling dark current (black lines).*

The bias dependence of the photocurrent for $I_{set}$ = 3000 is shown in Fig. 4.2. In contrast with Fig. 4.1, the bias dependence of the tunnel photocurrent is not exponential. At low bias one observes two distinct groups of curves which will be interpreted below (see Sec. II.1) as arising from a bistability of the mechanical contact. This bistability cannot be due to incorporation or removal of single molecules in the tunnelling gap[69] because the relatively large contact area averages out this type of fluctuation. It is also pointed out that individual bias scans are performed at a frequency higher than that of the instabilities which will allow us to remove their effects.

[69] *A. C. H. Rowe and D. Paget, Phys. Rev. B***75**, *115311 (2007)*

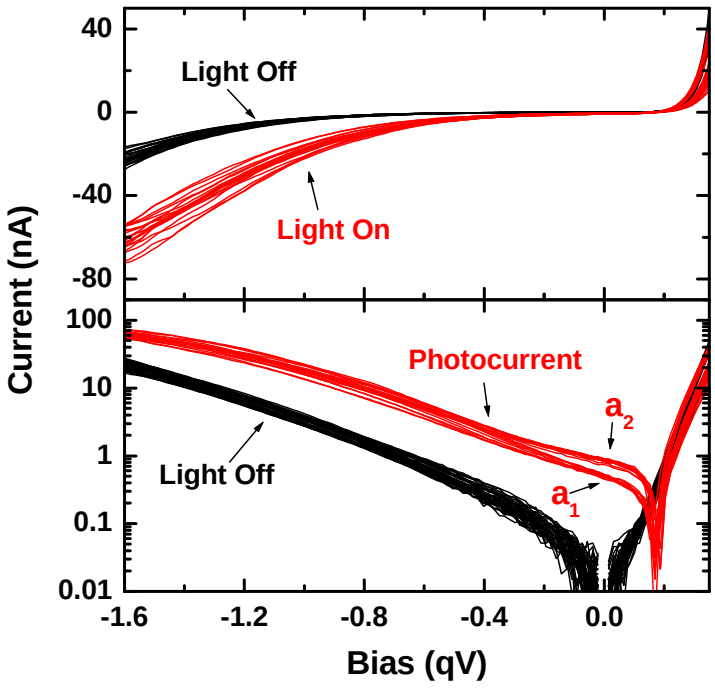


***Fig. 4.2:*** *The top panel shows, in black, the bias dependence of the dark tunnel current obtained for $I_{set}$= 3000 and, in red, of the current under light excitation. The absolute values of the tunnel photocurrent and of the dark current are shown in logarithmic units in the bottom panel. The scans for the tunnel photocurrent can be divided into two groups, labelled $a_1$ and $a_2$, thus showing the existence of instabilities in the contact. These groups correspond to a distinct combination of distance and contact area, and approximately give the same dark current value observed in reverse.*

We now summarise the experimental results for the selected values of $I_{set}$. The bias dependences of the tunnelling dark current are shown in Fig. 4.3. As expected, these curves show a rectifying behaviour with a current which increases with increasing $I_{\mathrm{set}}$. In forward (positive) bias the current increases exponentially. Qualitatively, the slope increases with increasing $I_{\mathrm{set}}$. This finding is in agreement with Eq. (2.45) and with the experimental results of Ref. (70) according to which the ideality factor decreases with increasing capacitance $C_{\mathrm{m}}$ of the tunnel gap.

It is concluded that an increase of $I_{set}$ induces a reduction of the cantilever-surface distance. In reverse (negative) bias at large distances (i.e. negative $I_{set}$) the dark current increases exponentially while its dependence at small distances is closer to linear. This is qualitatively similar to that observed elsewhere.[71] On acquisition cycle of the bias dependence of the additional current under light excitation is shown in Fig. 4.4 for selected values of $I_{set}$. As already suggested by Figs. 4.1 and 4.2, these curves can be separated into two groups.

[70] *H. C. Card and E. H. Rhoderick, J. Phys. D* ***4****, 1589 (1971)*
[71] *H. C. Card and E. H. Rhoderick, J. Phys. D* ***4****, 1602 (1971)*

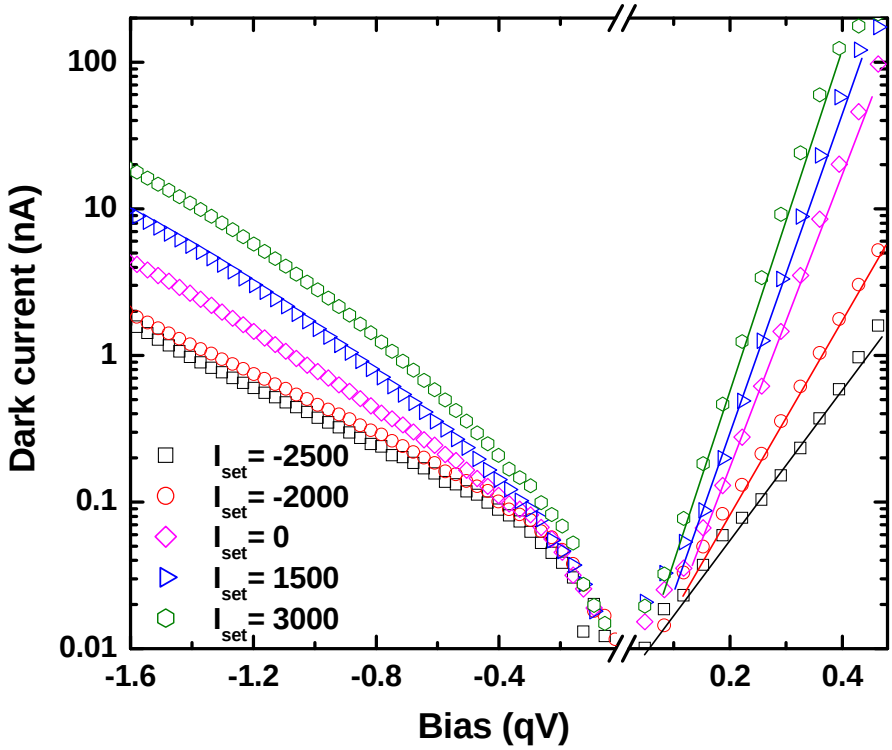


***Fig. 4.3:*** *Tunnel dark current from a cantilever into a nonmagnetic gold surface as a function of applied voltage for different values of $I_{set}$. The slope of the nearly exponential behaviour in forward (positive) bias gives the ideality factor.*

- At large distance ($-2500 < I_{set} \leq -1000$), in the same way as for Fig. 4.1, the curves are exponential with a slope which decreases with distance.

- For smaller distances ($0 \leq I_{set} < 1500$) there occurs, as for Fig. 4.2, a faster increase of the signal at large bias which eventually tends to saturate. The departure from exponential behaviour is quite small for $I_{set} = 0$ and progressively increases with increasing $I_{set}$. For $I_{set} =$ 2000 and 3000 the exponential behaviour is no longer visible at low bias.

The dependence of the tunnel photocurrent as a function of light excitation power has also been investigated. Shown in Fig. 4.5 are the dependences of the tunnel photocurrent on light power for a bias of -1.5 V. A power law dependence is observed with an exponent of the order of 0.5. The exponent seems to increase slightly with increasing distance from a value of 0.44 at small distances to 0.66 at large distances.

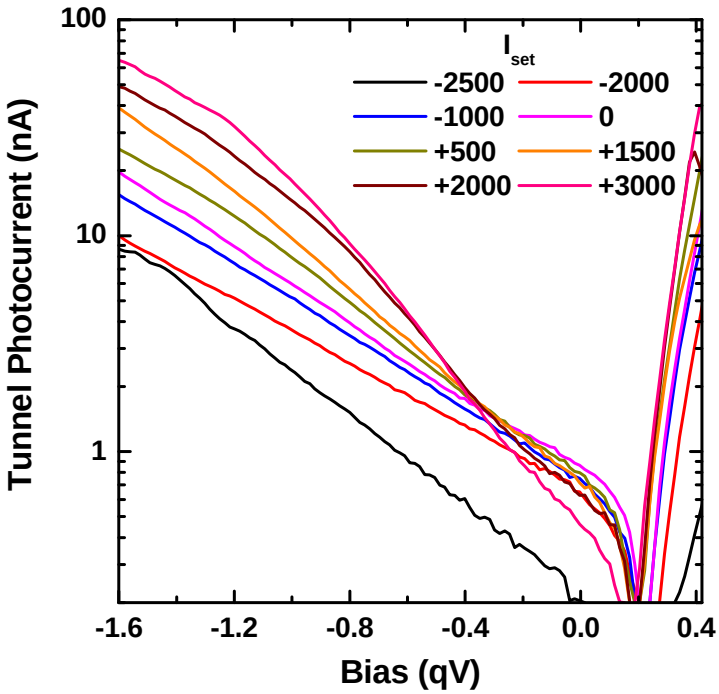


***Fig. 4.4:*** *Tunnel photocurrent from a cantilever to a nonmagnetic gold surface as a function of bias for different values of* $I_{set}$.

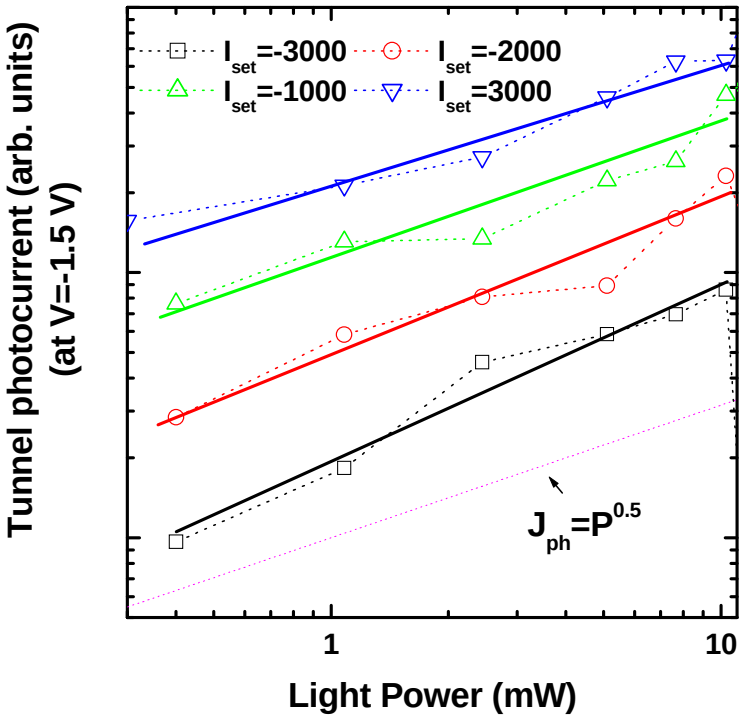


***Fig. 4.5:*** *Tunnel photocurrent as a function of exciting light power for different distances. All curves were taken under the same conditions as the corresponding curves of Fig. 4.4. The applied bias is -1.5 V.*

*II.2 Discussion*

It is now shown that the bias dependence of the tunnel photocurrent, the dark current and the instabilities at low bias and small distance are highly sensitive to the geometry of the mechanical contact between the tipless cantilever and the metal surface. Existence of the mechanical contact is first determined from the atomic force between the metal and the cantilever which can be measured using the quadrant photodiode. As seen in Fig. 4.6, up to a value of $I_{set}$ situated between 0 and +1500, this force is constant and equal to a value taken as zero (red squares). A repulsive force appears for larger values of $I_{set}$ so it is concluded that this threshold corresponds to mechanical contact between the cantilever and the metal.

Once in contact, the open squares of Fig. 4.6 reveal two distinct values of the atomic force and therefore demonstrate some degree of mechanical bistability. Since the atomic force and the injected current have been measured in the same experiment, this bistability has been found to be correlated with the bistability of the tunnel photocurrent shown in Fig. 4.2 as well as of the ideality factor.[72] The largest atomic force corresponds to the curves $a_1$ while the smallest atomic force corresponds to the curves $a_2$.

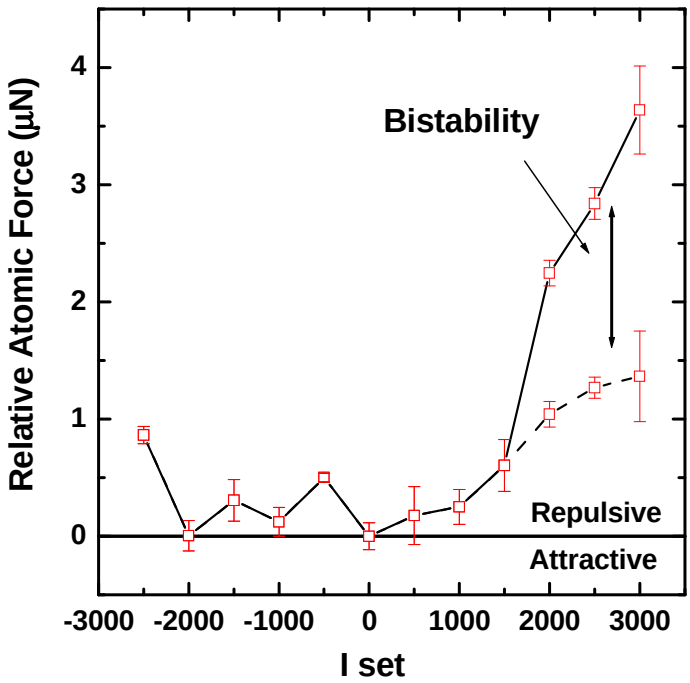


***Fig. 4.6:*** *Atomic force as a function of $I_{set}$, measured using the reflected laser beam and the quadrant photodiode. For negative values of $I_{set}$ the atomic force is approximately constant and taken as zero. It increases for positive $I_{set}$ situated between 0 and +1500. This regime corresponds to mechanical contact between the cantilever and the surface. In this case a bistability of the distance leads to the observation of two distinct values of the atomic force.*

[72] *For $I_{set}$=3000 the ideality factor changes from 1.64 to 1.51, between Curves $a_1$ and $a_2$ of Fig. 4.2, respectively This implies a slight bistability in cantilever-sample distance during the measurement.*

The observed bistability implies a correlated change of distance and total contact area for a constant value of the dark current at the reference bias $V_{set}$. This hypothesis is shown graphically in Fig. 4.7. Panel c indicates that in mechanical contact, the injected current comes from two zones: one in direct mechanical contact and another slightly out of mechanical contact. The bistability concerns the relative areas of the two zones and gives rise both to a modification of the bending of the cantilever and of the total injected current.

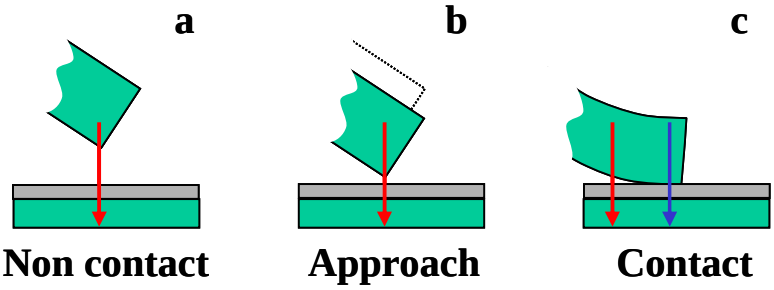


***Fig. 4.7****: Geometry of the cantilever for $I_{set}$ = -2500 (a), -1000 (b) and 2500 (c). Shown in grey is an interface layer, which determines the tunnelling distance in contact. The red arrows correspond to injection in the non contact regime, while the blue arrow is specific to injection in contact and corresponds to a bias dependence summarised in Fig. 4.8.*

These ideas are verified by a comparison of atomic force, ideality factor and tunnel photocurrent bias dependence as a function of $I_{set}$. These distinct measurements show two correlated regimes, approximately before and after mechanical contact.(The limit between the two corresponds to $I_{set} = 0$)

Before mechanical contact, the decrease of the ideality factor as a function of increasing $I_{set}$, (seen from the slope of the dark current in forward bias in Fig. 4.3) reveals a decrease of the cantilever-tip distance. The decrease of the tunnel distance is also revealed, as will be seen below, from the decrease of the exponential slope of the tunnel photocurrent between the curves at $I_{set}$ = -2500 and $I_{set}$ = -2000 (shown in Fig. 4.4).

After mechanical contact, the constant value of the ideality factor reveals as expected a constant cantilever-metal distance. The values of this distance and of the capacitance $C_m$ are probably determined by a residual interlayer whose nature will be discussed below. However as seen from Fig. 4.4, the tunnel photocurrent bias dependence does not saturate. The strong change of current magnitude with increasing $I_{set}$ can be given the same explanation as the instability: this change is due to the increase of the relative fraction of the cantilever in contact.

The dark current and tunnel photocurrent data in contact will now be corrected in order to extract the contribution from the sole part of the cantilever in mechanical contact. It

will be assumed that the bias dependence of the section just out of contact (red arrow of panel c in Fig. 4.7) is homogeneous in space and coincides with the one of the smallest distance giving an exponential dependence ($I_{set}$ = -1000). In this context it will be shown that it is possible to decompose all data curves for $I_{set}$ > -1000 into the sum of a fraction α of the signal obtained at $I_{set}$ = -1000 and of a signal for which the shape does not depend on the value of $I_{set}$.

Fig. 4.8 shows the calculated contributions of the contact to the tunnel photocurrent for various values of $I_{set}$. As expected, these curves are almost coincident within a multiplicative factor. In the same way, as shown in Fig. 4.9 all the corrected dependences of the dark current for $I_{set}$ > 0 are identical within a multiplicative factor. The values obtained for α, given in Table 4.1, decrease for increasing $I_{set}$, thus revealing the increase of the relative fraction of the tunnel area in mechanical contact. For $I_{set}$=3000, the value of α corresponding to Curves $a_2$ of Fig. 4.2, is larger than for Curves $a_1$, which indicates that the contact area is smaller.

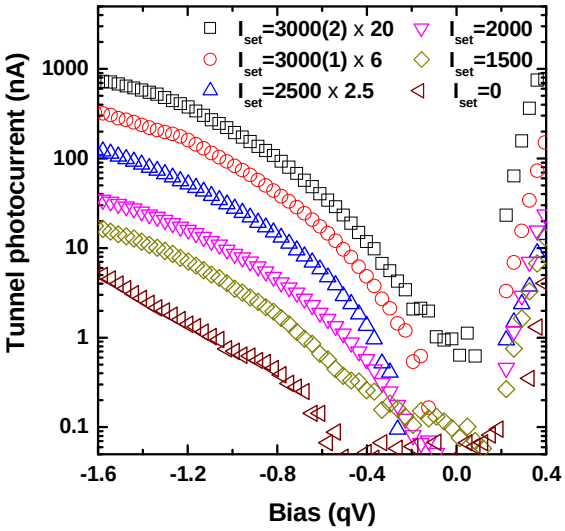


***Fig. 4.8:*** *Corrected dependences of the tunnel photocurrent in the mechanical contact regime. For $I_{set}$ = 3000 the two curves $a_1$ and $a_2$ of Fig. 4.3 have been included in the correction.*

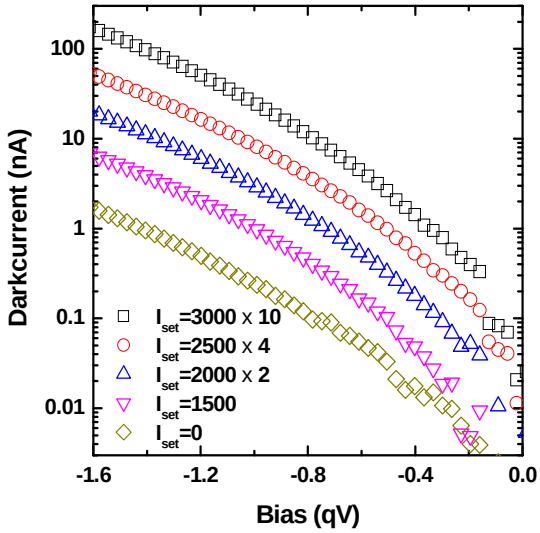


***Fig. 4.9****: Corrected dependence of the dark current. (reverse bias)*

| $I_{set}$ | 3000 ($a_2$) | 3000 ($a_1$) | 2500 | 2000 | 1500 | 0 |
|---|---|---|---|---|---|---|
| α | 1 | 0.7 | 0.8 | 0.85 | 1 | 1 |

***Table 4.1:*** *The parameter α gives a measure of the relative fraction of the tunnel area out of contact. As expected this value decreases with increasing $I_{set}$.*

The right panel of Fig. 4.10 shows the corrected dark current behaviour for a forward bias, to be compared with the uncorrected one shown in the left panel. The uncorrected curves show a non exponential behaviour for a bias smaller than 0.2 V arising from the admixture of the noncontact (smaller slope) component. This nonexponential behaviour has completely disappeared after correction thus revealing a homogeneous contact geometry and an improved exponential behaviour over as much as 4 orders of magnitude.

These results show that, in mechanical contact, the tunnel current can be modelled by two contributions: one characterized by a non contact configuration close to that found for $I_{set}$ = -1000 and homogeneous in space. The other one, characterized by a fixed cantilever/metal distance, defines the bias dependences of the reverse and forward bias dark currents and the tunnel photocurrent which are independent of $I_{set.}$ These curves are shown respectively in Fig. 4.8, the left panel of Fig. 4.10 and in Fig. 4.9. The dependence of the ideality factor as a function of $I_{set}$ is shown in Fig. 4.11. This value increases from 1.6 under contact to 2.9 at large distances. This behaviour is similar to that obtained by Card and Rhoderick for controlled MIS structures based on silicon.[73]

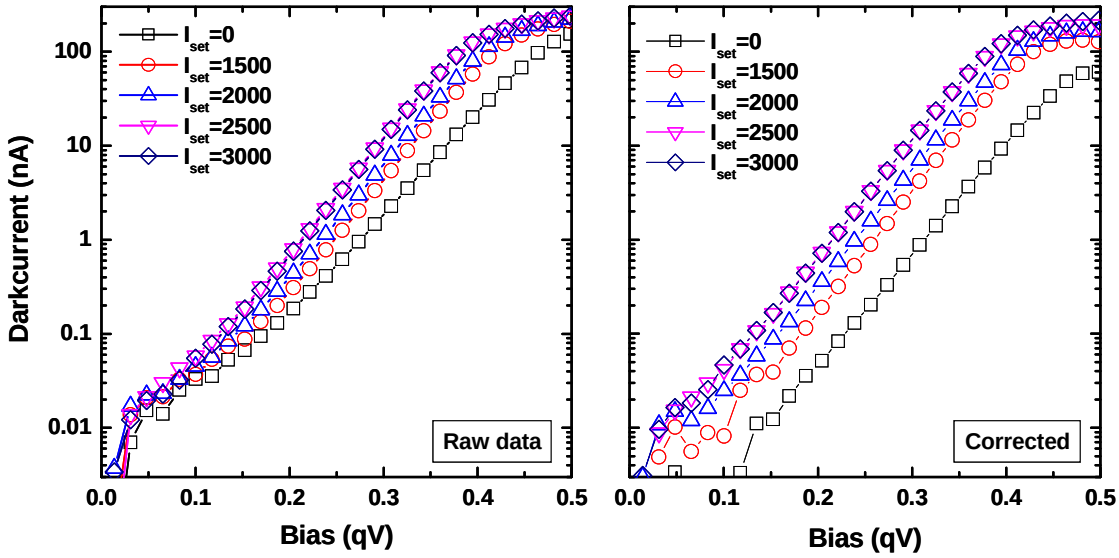


***Fig. 4.10**: Forward bias dark current dependence before (left) and after (right) the correction which removes the effect of the tunnel area out of contact. This correction improves the exponential character of the current for forward bias.*

[73] *H. C. Card and E. H. Rhoderick, J. Phys. D* ***4****, 1602 (1971)*

The bias dependences of the tunnel photocurrent as a function of distance are summarised in Fig. 4.12. This figure groups the measured results for the noncontact situations where $I_{set} \leq 0$ along with the curve characteristic of mechanical contact [we have taken curve (3000) (1) of Fig. 4.8 as a representative for mechanical contact]. These results will be compared with the model in the following section.

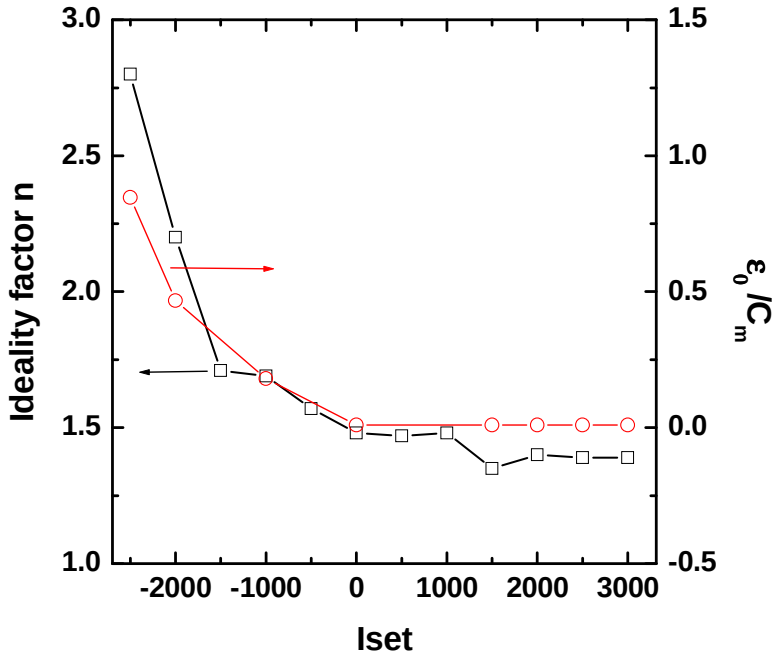


***Fig. 4.11:*** *Dependence of the ideality factor as a function of $I_{set}$. For $I_{set} \geq 0$ that is, in the contact regime, the ideality factor is found nearly constant. Also shown in red are the values of the tunnel capacitance used in the fits of Sec. III. There is a qualitative agreement between the variations of the two quantities.*

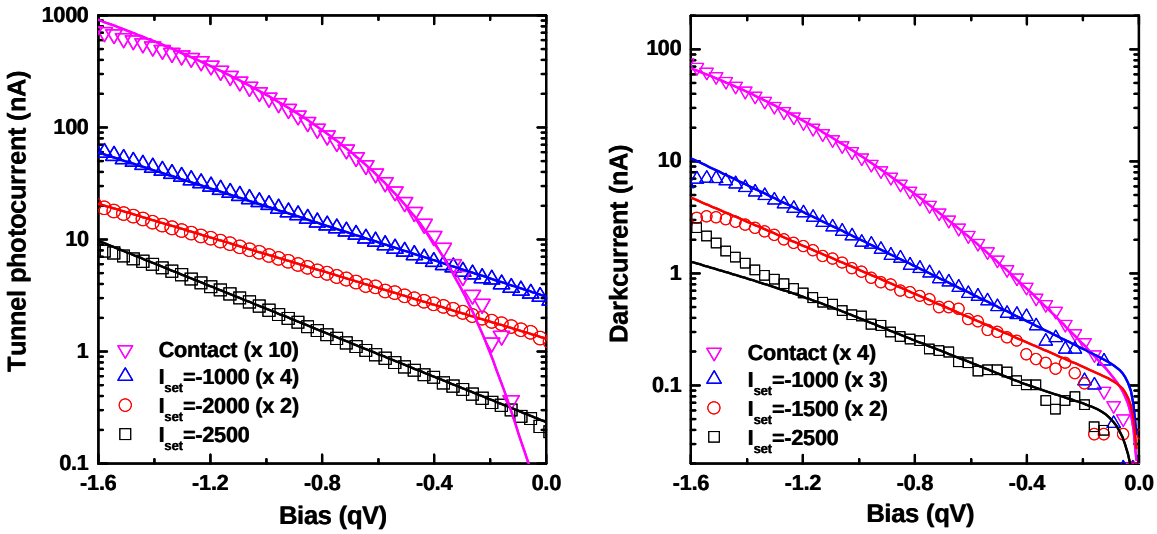


***Fig 4.12:*** *Interpretation of the experimental tunnel photocurrent (left panel) and dark current (right panel) into nonmagnetic gold surfaces using the model of Chapter 2. The solid lines are calculations made with the parameters outlined in the text. The curve labelled contact presents the corrected data for $I_{set}$ = 3000 after subtraction of the contribution from the non contact tunnel current.*

## *III. Interpretation*

The purpose of the present section is twofold:

- To determine which of the components of the photoassisted tunnel current is dominant among the three possibilities considered in Chapter 2 (tunnelling from the conduction band, from surface states or from the valence band)

- To determine the relevant mechanism for its bias dependence. As discussed in Chapter 2, this process can be the bias dependence of the tunnel barrier height or of the surface recombination velocity.

These issues are analysed successively in subsections 2 and 3, while subsection 4 is devoted to the fits of the experimental results as a function of distance.

### *III.1 Values of the parameters used in the interpretation*

Before discussing physical processes, it is crucial to assign values to the parameters used in the model. Since there is a relatively large number of parameters, in order to obtain a qualitative picture we have taken reasonable values from the literature without attempting to adjust them. These values are given in Appendix C.

Apart from these values, three semi-adjustable parameters were kept constant for all spectra. The density of surface states $N_T(0)$ will be chosen to be $6\text{x}10^{18}\text{eV}^{-1}\text{m}^{-2}$, as justified in Sec. III.3 below. As seen in Appendix A, the concentration $N_0$ is estimated from a resolution of the diffusion equation. Using Eq. (2.42) which expresses the dependence of tunnel photocurrent on the excitation power, we take $f^*=0.38$ which is close to the measured exponent in Fig. 4.5. For simplicity we also take $f= f^*$.[74] The surface recombination velocity $S_0$ was taken as $10^5$ m/s.

The only completely adjustable parameters for each spectrum were $\varepsilon_0/C_m$ and $\omega$, defined respectively by Eq. (2.16) and Eq. (2.43) which are both proportional to the tunnelling distance. The respective proportionality constants are $\varepsilon_t$ and $\Phi_b^*$, neither of which is well-known since they depend on the interfacial chemistry. Also unknown are the tunnel matrix elements for tunnelling from the conduction and valence bands as well as from surface states.

[74] *Recall that $f^*$ defined by Eq. (2.27) defines the energy of the first quantised state in the depletion layer, while f, defined by Eq. (2.40), defines the kinetic energy of the tunnelling electrons from the conduction band.*

*III.2 Negligibility of the photoassisted tunnel currents from surface states or from the valence band.*

The observed tunnel photocurrent cannot come from surface states or from the valence band for two distinct reasons:

- As discussed in Sec. III.2 of Chapter 2, the power dependence of $J_{ts}$ is very weak and cannot explain the experimental results. At large distances one has $\beta << 1$ so that, as seen from Eq. (2.44), this dependence is dominated by that of $N_0^{\omega_s}$. For $d$ = 1nm one finds $\omega_s \approx 5x10^{-3}$ which is one order of magnitude smaller than the experimental value. Even larger discrepancies are found at smaller distances. The same reasoning also holds for the photocurrent from the valence band, defined by Eq. (2.46), where the larger tunnel barrier height results in values of $\omega_v$ even smaller than $\omega_s$.

- The bias dependence of $J_{ts}$ and $J_{tv}$ cannot explain the experimental results. Fig. 4.13 shows a comparison with experimental data using Eq. (2.44) and Eq. (2.46). The tunnel current from surface states is dominated by the exponential terms so that at large distance the experimental data can be fitted. At shorter distances however, the exponential bias dependence of $J_{ts}$ cannot fit the experimental data. $J_{tv}$ shows a very strong bias dependence near the threshold voltage (i.e. at low bias) that is not observed in the experiment.

$J_{ts}$ and $J_{tv}$ are small with respect to $J_{tb}$ because their respective tunnel barriers are larger than for conduction electrons, or possibly because of their relatively small tunnel matrix elements and coherence length $\ell_c$ for $J_{tv}$ in Eq. (2.46). In agreement with these conclusions, the tunnel current from the conduction band of n-type GaAs is known to be larger than that from the valence band.[75] Moreover, no tunnel current from defects is found on oxygen covered GaAs.[76]

*III.3 Comparison of the model with experimental data*

The calculated dependences of the tunnel photocurrent from the conduction band $J_{tb}$, shown in Fig. 4.12, are in very good agreement with the experimental results. The obtained values of $C_m$ and $\omega$ are given in Table 4.2. The same parameter values also enable us to quantitatively explain the power dependence of the photocurrent shown in Fig. 4.5 because the value of $f$ used in the model is close to the exponent of the power dependence. Also

[75] *R. M. Feenstra, Phys. Rev. B* ***50****, 4561 (1994)*
[76] *R. M. Feenstra, and J. A. Stroscio, J. Vac. Sci. Technol. B****5****, 923 (1987)*

shown in Fig. 4.11, along with the experimental values of the ideality factor, are the values of $\varepsilon_0/C_m$. The qualitative agreement between the two quantities will be interpreted in the following section.

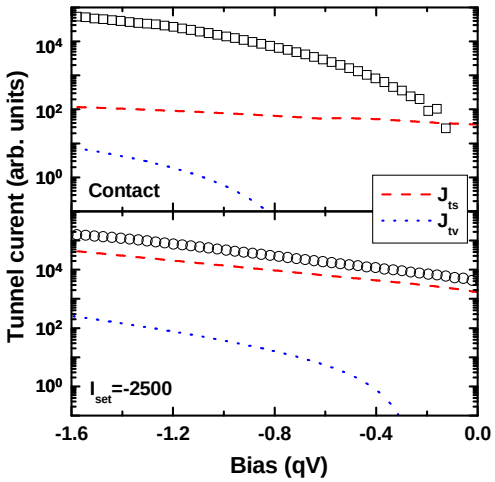


***Fig. 4.13:*** *Calculated bias dependences of the tunnel currents for the processes discussed in Chapter 2: $J_{ts}$ and $J_{tv}$. While the relative amplitude of these currents, which depends on the relative matrix elements, is not well-known, the bias dependence of these tunnel currents can not fully explain the experimental results for all of noncontact (circles) and contact regimes (squares).*

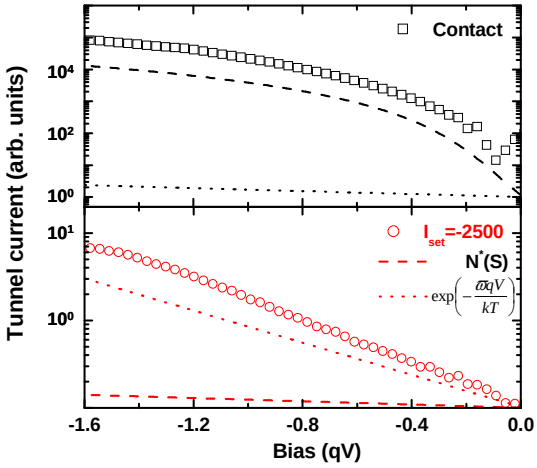


**Fig. 4.14:** *Identification of the dominant mechanism for bias dependence of the tunnel photocurrent. This figure shows the calculated bias dependences of the factors $\exp(-\omega qV/kT)$ and $N^*(S)$ of Eq. (2.41), describing the bias dependence of the tunnel barrier and the effect of surface recombination, respectively. While the former effect is dominant at large distance, ($I_{set}$=-2500) in contact ($I_{set}$=3000) after correction the bias dependence of the tunnel photocurrent is determined by the changes of surface recombination velocity.*

Recalling Eq. (2.41) and Eq. (2.42), which we reproduce here taking $\omega << f$

$$J_{tb} = J_{tb}^0 N^*(S) \exp\left(-\frac{\omega qV}{kT}\right) \qquad N^*(S) = \frac{A^{**}T^2}{qS} W_0\left[\frac{qSn_0}{A^{**}T^2}\right]^f$$

the bias dependence of the tunnel barrier height is responsible for the exponential factor of $J_{tb}$, while the surface recombination velocity $S$ modifies the effective electron concentration $N^*(S)$. The bias dependences of $\exp(-\omega qV/kT)$ and of $N^*(S)$ are shown in Fig. 4.14 for $I_{set} = -2500$ and in the contact regime.

At large distance, the linear variation of $\Delta\varphi$ shown in Section IV.2 of Chapter 2 induces an exponential dependence of the photocurrent of the type exp(-$V/V_{ph}$), where

$$\frac{kT}{qV_{ph}} = \gamma_t^* + \omega \qquad (4.1)$$

The first term in this expression, defined in Eq. (2.53), reflects the bias dependent change of concentration $N^*(S)$ caused by the change of the recombination velocity. Since at

large distance $S >> v_d$ in Eq. (2.42), $Sn_0$ does not depend on bias and its value is obtained using Eq. (2.53). This is equal to $C_m / qN_T(0)$ and is proportional to $d^{-1}$. The second term of Eq. (4.1), proportional to *d*, expresses that of the tunnel barrier. The observed decrease of the slope for decreasing distance between $I_{set}$ = -2500 and $I_{set}$ = -2000 implies that the exponential increase of the tunnel current is determined by the bias dependence of the tunnel barrier so that $\gamma_t^* < \omega$. The subsequent increase between $I_{set}$ =-2000 and $I_{set}$ =-1000 suggests that d is now small enough that $\gamma_t^* > \omega$.

| $I_{set}$ | Contact | -1000 | -2000 | -2500 |
|---|---|---|---|---|
| $\varepsilon_0/C_m$ *(nm)* | 0.009 | 0.18 | 0.46 | 0.85 |
| $\omega$ | 0.011 | 0.017 | 0.027 | 0.043 |
| $\alpha_d'$ $(10^{-3}\,V^{-1})$ | 30 | <2 | <2 | irrelevant |

***Table 4.2:*** *Values of the capacitance of the tunnel gap $C_m$[Eq. (2.16)] and of the reduced distance ω, [Eq. (2.43)] for the model calculation shown in Fig. 4.12. $\alpha_d'$ is used for calculating the dark current.*

The condition $\gamma_t^* \approx \omega$ implies that the value of $\omega$ is given by the measured exponential slope at large distance. Using the values of $C_m$ and $\omega$ given by Table 4.2, one finds that $qN_T(0)$ should be of the order of several $10^{18}$ $eV^{-1}.m^{-2}$ which is indeed the case.

In contact, as shown in the top panel of Fig. 4.14, the effect of the tunnel barrier variation on the bias dependence of the tunnel current is negligible, so that this dependence is almost entirely caused by the bias change of the surface recombination velocity.

## *IV. Discussion*

### *IV.1 Interface chemistry*

The values of the parameters used in the comparison with data obtained for Au suggest that the natural oxide layer originally present at the GaAs surface has been partially removed. Indeed for a Schottky barrier composed of gold deposited on naturally-oxidized GaAs, one finds a value of $\varepsilon_0/C_m = d/\varepsilon_t \approx 1.5$ that is about 2 orders of magnitude larger than the one measured here in contact.[77] A possible explanation for this result is that the oxide has

[77] *N. L. Dmitruk, O. Yu Borkovskaya, and O. V. Fursenko, Vacuum, **50**, 439 (1998)*

been at least partly removed by an electrochemical reaction at cathodic potentials, similar to that previously observed on InP.[78]

Taking $\Phi_b^* \approx 4$ eV as discussed in Appendix C, one finds using Eq. (2.43) that the distance *d* ranges between realistic values of 1.1 nm to 0.45 nm in the non contact regime and is about 0.28 nm under contact. The value of the dielectric constant of the interfacial layer $\varepsilon_t$ is shown in Fig. 4.15 as a function of distance. It is equal to $\varepsilon^* \approx 30$ in contact which suggests the formation of a partial molecular film of water (dielectric constant 80 and thickness $d^* \approx$ 0.28 nm) between the semiconductor and the metal. Also shown in Fig. 4.15 is the expected distance dependence of the effective dielectric constant as a function of distance for the non contact regime where $d > d^*$. The correspondence between the calculated curve and the data is unexpectedly good.

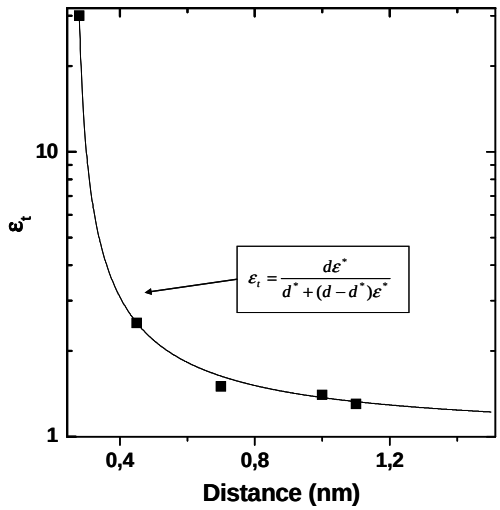


***Fig. 4.15:*** *Calculated dependence of the dielectric constant out of contact as a function of distance d assuming that the metal is covered by a layer, probably mainly water, for which the dielectric constant and thickness are the values obtained by comparing the model with the data obtained in contact. The data points correspond to the dielectric constant and distance used in the model for the out of contact curves.*

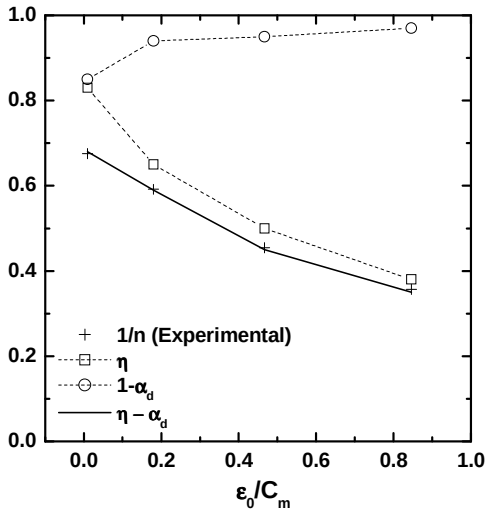


***Fig. 4.16****: Measured inverse values of the ideality factor as a function of the inverse capacitance (black crosses). The open squares are the values of η, the fraction of surface states following the metal statistics. Also shown (open circles) are the values of 1-$\alpha_d$, the inverse ideality factor corresponding to residual mechanisms. The equality between η-$\alpha_d$ (solid line) and $n^{-1}$ was imposed in the calculation according to Eq. (2.45).*

[78] *N. C. Quach, N. Simon, I. Gérard, P. Tran Van and A. Etcheberry, J. Electrochem. Soc.* ***151****, C318 (2004)*

*IV.2 Dark current*

The model of Chapter 2 (Sec. II. c) also allows quantitative analysis of the ideality factor and of the dark current under reverse bias using the same parameter values. These quantities depend on the following additional parameters: i) $\eta$, ii) $\alpha_d$ and $\alpha_d'$, iii) the effective density of states $N_T^d(0)$ taken here as $0.1\,N_T(0)$ [Recall that $\eta$ is the fraction of surface states which follow the metal statistics and that $(1-\alpha_d)^{-1}$ would be the ideality factor corresponding to additional processes].[79] Under forward bias, the behaviour of the ideality factor in Fig. 4.11 is clearer in Fig. 4.16 which shows the dependence of $n^{-1}$ as a function of $\varepsilon_0/C_m$. Since the above analysis shows that $\varepsilon_s/W << q(1-\eta)N_T(0)$ and $C_m << \eta q N_T(0)$, Eq. (2.45) simply becomes $n^{-1} \approx \eta - \alpha_d$.

The reverse bias dependence of the dark current, calculated by imposing $\eta - \alpha_d = n^{-1}$, accounts very well for the experimental results of Fig. 4.12. The values of $\eta$ and $1-\alpha_d$ are also shown in Fig. 4.16. As shown in Table 4.2, $\alpha_d'$ has very small value, of the order of $10^{-3}$ $V^{-1}$ apart from the contact regime. This analysis also suggests that, as expected,[80] the quantity $\eta$ decreases with increasing distance from a value of about 0.84, while the residual ideality factor $(1-\alpha_d)^{-1}$ decreases from 1.20 to 1.04 so that the latter processes are only significant in contact.

*IV.3 Effect of quantisation of surface states.*

The kinetic energy $f\varphi_b$ of the relevant tunnelling electrons is found from the power dependence of the tunnel photocurrent which gives $f \approx 0.4$. This value gives an upper limit to the parameter $f^*$ which yields the energy of the first quantised level. Shown in Fig. 4.17 is the bias dependence of the value of $f^*$ along with that of the surface barrier in the contact regime. This value was calculated using Eq. (2.27) neglecting the modification of the surface electric field due to the photoelectrons in the depletion layer. One sees that $f^*$ ranges from 0.38 to about 0.25, which is smaller than the measured value of $f \approx 0.4$. In view of the numerous quantities which play a role in defining the value of *f*, the agreement is considered quite

[79] *The presence of two distinct types of surface states and the bias dependence of the barrier* $\varphi_0^*$ *have not been taken into account under light excitation. This is reasonable since i) photoelectron capture processes increase the kinetics of establishment of equilibrium with the semiconductor, ii) because of the photovoltage, the correction term, proportional to* $\Delta\varphi - qV_s$, *is smaller under light excitation than in the dark.*

[80] *H. C. Card and E. H. Rhoderick, J. Phys. D* ***4****, 1589 (1971)*

satisfactory and one can consider $f \approx f^*$. The small difference between the two parameters could be due to the effect of the electric field on the conduction electrons in the depletion layer. It is concluded that the tunnelling electrons have a nearly constant energy quite close to that of the first quantised state in the depletion layer.

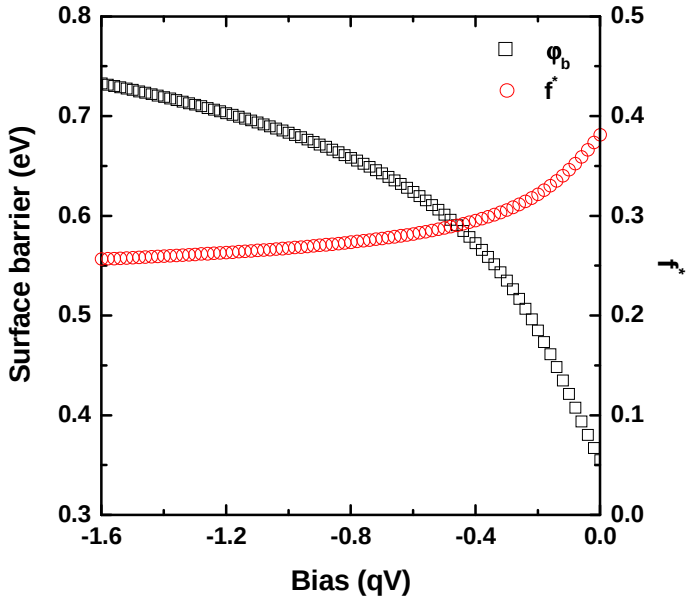


***Fig. 4.17:*** *Bias dependence of the surface barrier, as found from the model calculation of the tunnel photocurrent in the contact regime. Also shown is the quantity $f^*$, defined by Eq. (2.27), which characterises the position of the lowest quantised state in the depletion layer near the surface. This factor ranges from 0.4 to 0.28 and is slightly smaller than the exponent for the power dependence of the tunnel photocurrent.*

### *IV.4 Validity of the approximations made*

Image charge effects, which have been neglected in Eq. (2.41), might modify the tunnel photocurrent bias dependence at small distance. However, the characteristic energy for evaluating the magnitude of these effects $\lambda = q\ln(2)/(8\pi\varepsilon_t d)$, of the order of 0.4 eV for $\varepsilon_t = \varepsilon_0$ and $d$ = 1 nm, is one order of magnitude smaller than the effective tunnel barrier height $\Phi_b^*$. As proposed by Simmons,[81] these effects mostly induce an effective reduction of the tunnel distance. This effective distance increases with increasing bias and should therefore lead to a super-exponential dependence of the tunnel photocurrent on applied bias. This however is at variance with the experimental results at small distance so image charge effects are negligible.

In order to obtain analytical expressions for $J_{tb}$, this current was assumed to be negligible with respect to the photocurrent ($J_p$) and Schottky currents ($J_s$). This assumption is

[81] *J. G. Simmons, J. Appl. Phys.* ***34****, 1793 (1963)*

certainly valid at large distance but in contact, the photocurrent $J_p \approx qN_0 S / v_d$ decreases because of the reduced surface recombination velocity and could become a lower limit value for the tunnel photocurrent. However, this possibility can also be excluded because the tunnel photocurrent in Fig. 4.12 does not saturate at high bias and the power dependence of $J_p$ is quite different from that predicted in Eq. (2.30).

## *V. Conclusion*

This chapter contains an experimental study of unpolarised photoelectron injection from a tipless GaAs cantilever into a (nonmagnetic) gold surface. It has been shown that as soon as mechanical contact is established, the bias dependence of the injected tunnel current is composed of a noncontact part and of a contact part, the ratio of which depends on the geometry and bending of the cantilever against the metal.

The bias, distance and power dependence of the tunnel photocurrent, the ideality factor and the dependence of the dark current under reverse bias are well interpreted by the model described in Chapter 2 using identical parameters under all experimental conditions. It is shown that:

- In agreement with the power dependence of the tunnel photocurrent, the dominant contribution to this current comes from conduction electrons.

- In the noncontact mode, the exponential dependence of the tunnel photocurrent is due to the bias dependence of the tunnel barrier.

- The bias dependence of the tunnel photocurrent in the contact mode is a result of a decrease in the surface recombination velocity.

These results have been obtained in spite of the fact that i) the matrix elements for tunnelling from the conduction and valence bands and from surface states are not well-known. ii) The tunnel conditions of our experiment in air imply an imperfect knowledge of the parameters of the contact (width and dielectric constant of the tunnel gap). However, the fact that the experimental results can be quantitatively interpreted using values of the parameters of the model taken from the literature give us confidence in the above conclusions. The present picture will be used for the interpretation of the spin injection results in the following chapter.

## Chapter 4 : Summary

- Injection of charge from a tipless cantilever under mechanical contact can give rise to inhomogeneities in the tunnel photocurrent bias dependence. These inhomogeneities are corrected, so that the tunnel photocurrent bias dependence is given by Fig. 4.12. Unlike the case of a tip, the contact is approximately planar.

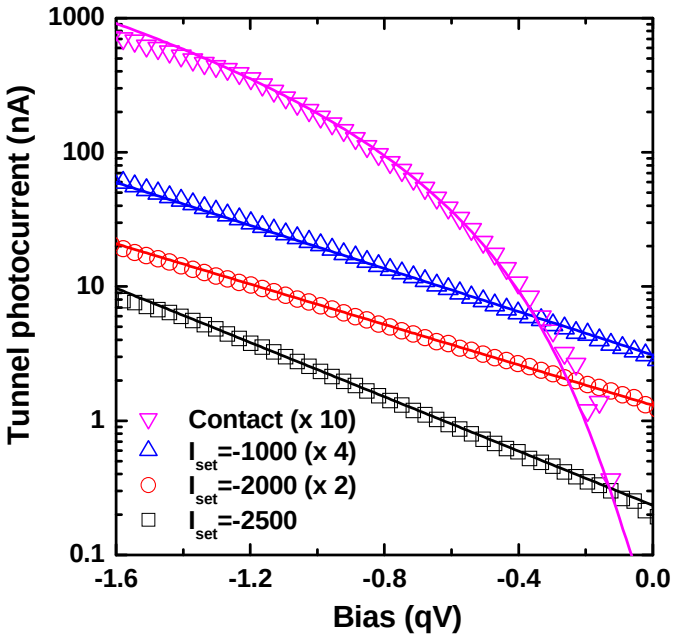


- In agreement with Eq. (2.41), at large distances the tunnel photocurrent increases exponentially with bias because of the bias dependence of the tunnel barrier. In contact, the sub-exponential increase of the tunnel photocurrent is due to the change of surface recombination velocity.

- The tunnel photocurrent mostly comes from conduction electrons.

- The model also accounts for the power dependence of the tunnel photocurrent, for the values of the ideality factor in forward bias and for the dark current under reverse bias.

# Chapter 5: Charge and spin injection into a magnetic surface

## *I. Introduction*

This chapter is dedicated to the presentation of the first results on spin dependent tunnel injection of photoelectrons into a (magnetic) Cobalt surface.

The density of unoccupied electron *3d* states probed by this injection has been studied before, mostly using inverse photoemission. According to Ref. (82) the exchange splitting between the minority-spin 3d band and majority-spin 3d band of a hexagonal-closed packed (hcp) Co(0001) thin film is 1.05 eV. Independently, C. Math *et. al.* have performed spin-resolved inverse photoemission analysis[83] with the results shown in Fig. 5.1. The experiment and theory for normal electron incidence on Co (0001) reveal a peak at 0.24 eV corresponding to the majority-spin band and a second peak near 0.7 eV corresponding to the minority-spin band. After passivation by gaseous CO (which will also be used on the Cobalt samples used in this work) the majority-spin peak is eliminated and the minority peak is little affected. It has been found that this spin dependent density of states is only slightly affected by the thickness of the Cobalt,[82] so it will be assumed that Fig. 5.1 represents a satisfactory description of the density of states of the Cobalt layers used here. The solid triangles of the top panel of Fig. 5.1 will be taken as the density of states $\rho_-$, while the open triangles will be taken as that for $\rho_+$, thus defining the relative difference in the density of states $\delta\rho/\rho = (\rho_+ - \rho_-)/(\rho_+ + \rho_-)$.

In Sec. II, I present the results of charge injection into magnetic Cobalt surfaces along with their interpretation, made using the same approach as for the Gold surfaces in Chapter 4.

Sec. III is devoted to the estimate of the electronic spin polarisation $\delta n_s / n_s$ using photoluminescence.

In Sec. IV, I show the absence (presence) of spin-dependent tunnelling for Gold (Cobalt) surfaces. For tunnelling into Cobalt, spin-dependent tunnelling asymmetries $A = [\delta n_s / n_s][\delta\rho/\rho]$ of the order of 6% are observed. The bias dependence of $A$ will be interpreted as being mostly due to that of $\delta n_s / n_s$, which in turn is the result of the bias-induced decrease of the surface recombination velocity (see chapter 2).

While the experimental results unambiguously demonstrate the spin-dependence of the tunnel effect, a more detailed analysis of the cantilever/surface distance dependence

[82] *G. J. Mankey, R. F. Willis and F. J. Himpsel Phys. Rev. B* ***47,*** *190 (1983)*
[83] *C. Math, J. Braun, and M. Donath, Surf. Sci.* **482-*485****, 556 (2001)***

requires better control of the chemical stability of the Co-GaAs interface which currently limits the dynamic range of the variation of the tunnel gap.

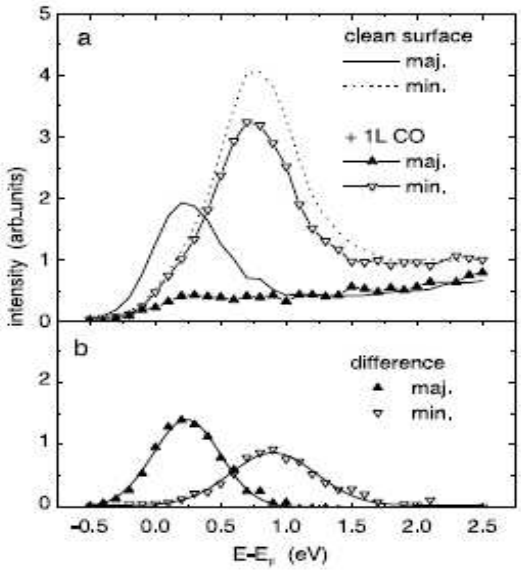


***Fig. 5.1:*** *Spin-resolved inverse-photoemission spectra of Co(0001) at the centre of the Brillouin zone: clean surface and surface exposed to 1L CO (a), difference spectra (b) [After Ref.( 2)].*

## *II. Charge injection into magnetic Cobalt layers*

### *II.1 Characterisation of possible instabilities of the interface*

The presence of a polar CO layer on the Cobalt surface renders it more hydrophilic and therefore less inert than the Gold surface. The interface chemistry could then give rise to a slow re-oxidisation of the surface and hence to more frequent instabilities in the atomic force and in the photocurrent. Fig. 5.2 (panel a) shows the time evolution of the dark current and of the photoassisted tunnel current directly after ex-situ growth of the Cobalt layer. Here $I_{set}$ = - 4000. The successive scans show a slow increase of the tunnel photocurrent, seen in more detail in the time evolution of the tunnel photocurrent at a bias of -1.5 V (panel b). The current progressively increases with time and tends to saturate after about 30 s.

Panel b of Fig. 5.2 also shows atomic force results. The increase with time of the atomic force between the cantilever and the surface (panel b) shows that mechanical contact is already established at the beginning of the experiment. According to the arguments presented in chapters 2 and 4, the non-exponential character of the tunnel photocurrent bias dependence (panel c) also indicates the establishment of mechanical contact.

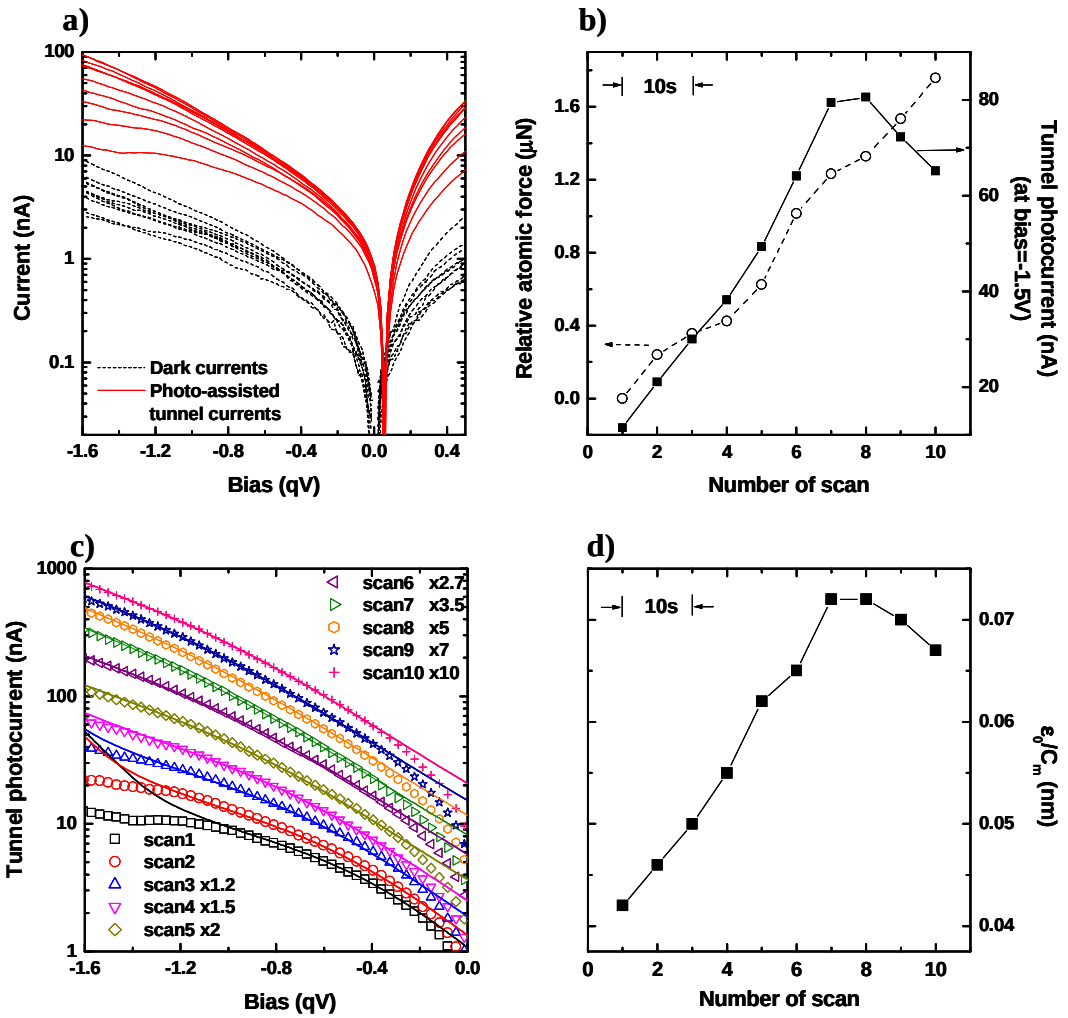


***Fig. 5.2:*** *Panel a shows the dark (dashed black lines) and the photo-assisted tunnel currents (solid red lines) for a Cobalt surface at $I_{set}$ = -4000. Panel b shows the evolution from one scan to another of the tunnel photocurrent at -1.5 V (dark squares). Also shown (open circles) is the relative variation of the atomic force between the cantilever and the surface. In panel c, each of these scans is interpreted by comparison of the bias dependence of the tunnel photocurrent with the model of Chapter 2 (see Sec. II. 3). Also shown in panel d is the dependence of the inverse tunnel capacitance as a function of the scan.*

We tentatively suggest that the observed evolution in the tunnel photocurrent and atomic force at the beginning of the experiment is due to the formation of an interfacial dielectric layer between the CO and the cantilever. This hypothesis will be verified in the following section from comparison of the tunnel photocurrent bias dependences (panel c) with the model described in Chapter 2. The formation of this layer induces a deflection of the cantilever and an increase of the dielectric constant of the interface which, according to Eq. (2.53),[84] increases $\Delta\varphi$ and therefore the tunnel current. Consequently most measurements on

[84] *Although this equation is valid at large distance, its qualitative implication according to which $\Delta\varphi$ increases with $\varepsilon_t$ is also true in contact.*

Cobalt surfaces are performed in mechanical contact with the interfacial layer so that a change of $I_{set}$ induces a change of the contact area rather than of the tunnel distance.

*II.2 Results*

The charge injection results are shown in Fig. 5.3 for the dark current and in Fig. 5.4 for the tunnel photocurrent. For a given $I_{set}$, relatively stable bias dependences were obtained, qualitatively similar to those obtained in Chapter 4 for Gold surfaces in mechanical contact. Since the cantilever is in mechanical contact, changes in $I_{set}$ only slightly affect the bias dependence of the current. Unexpected exceptions to this are most likely due to instabilities on a time scale longer than that of the measurements.

In reverse (negative) bias, the bias dependence of the dark current is generally sub-exponential. For a forward (positive) bias, the dark current bias dependence is exponential above about 0.2 V. Apart from $n$ = 1.9 obtained for $I_{set}$ = -1000, the ideality factor is larger than for Gold (in the 4-15 range).

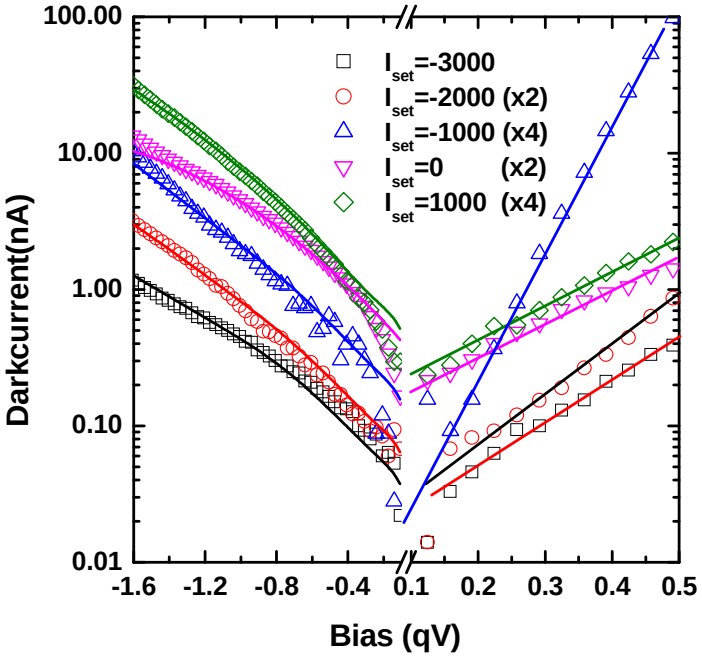


***Fig. 5.3:*** *Dark currents in forward (positive) bias as a function of tunnel distance. This is used to determine the ideality factor.*

Similarly, the bias dependence of the tunnel photocurrent only weakly depends on $I_{set}$ and is approximately exponential apart from $I_{set}$ = 1000, at which a clear sub-exponential dependence is found. Finally, Fig. 5.5 shows the power dependence of the tunnel photocurrent at a bias of -1 V for several values of $I_{set}$. The curves show a power law dependence with an exponent close to unity, at variance with the results obtained on Gold

surfaces. As in Chapter 4, this exponent is associated with the factor *f* describing the energy of tunnelling electrons at the semiconductor surface (see chapter 2).

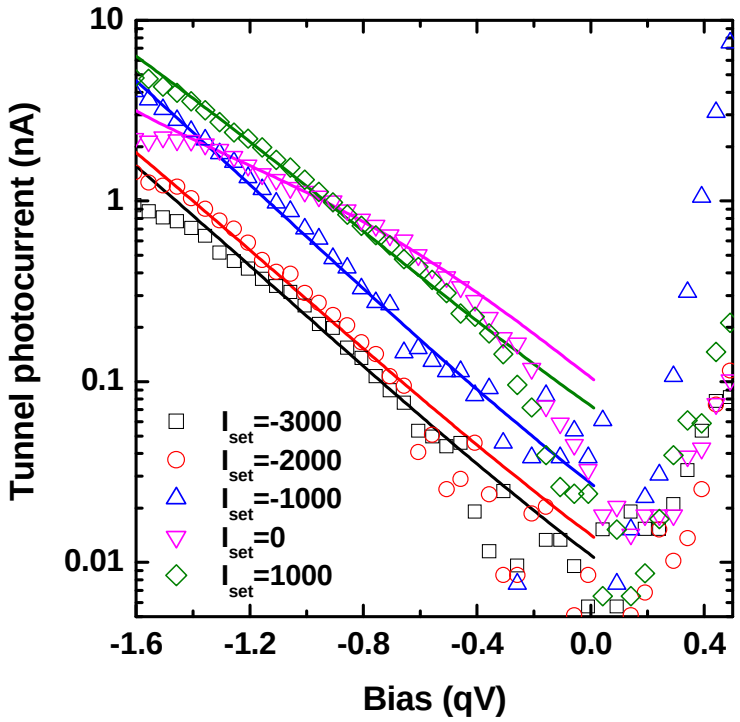


***Fig 5.4:*** *Tunnel photocurrent on Cobalt surfaces: bias dependences for various values of* $I_{set}$

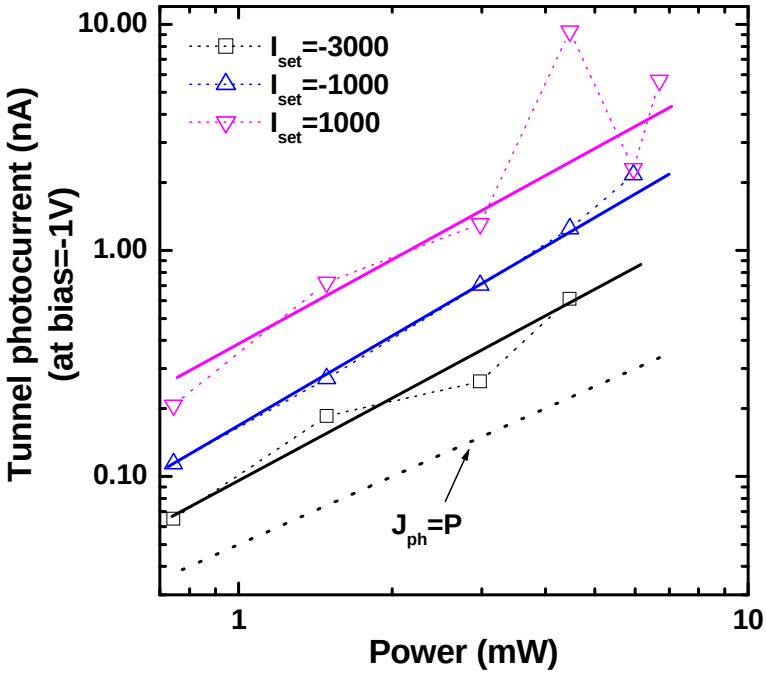


***Fig. 5.5:*** *Power dependence of the tunnel photocurrent at a bias equal to -1 V for selected values of* $I_{set}$*. The dotted line presents a linear dependence of tunnel photocurrent on exciting power. All curves show a power law dependence with an exponent approximately equal to 1.(~ f)*

In summary, Fig. 5.3, 5.4 and 5.5 show that the results of charge injection on Cobalt critically depend on the interfacial layer rather than solely on the tunnel distance. Qualitatively, in order to have a fixed tunnel current as imposed by the feedback loop, the decrease of tunnel current induced by the interfacial layer must be compensated by an increase in contact area. A more detailed understanding of the interface properties, such as tunnel distance and dielectric constant, require a better control of the environment and should be attempted in a future work. After the beginning of the experiments reported here (the first 10 minutes or so) a small number of instabilities still occur on time scales larger than those required for measurements. As such each individual measurement is free of instabilities and can be analysed in more detail using the model of Chapter 2.

*II.3 Discussion*

The interfacial layer can affect the electronic properties of the cantilever surface, for example the surface barrier at equilibrium $\varphi_0$ and the surface recombination velocity.[85,86] As a result, the concentration of photoelectrons in the depletion layer may be different than for Gold and may therefore modify the quantisation in the depletion layer. This may be the reason for the larger value of $f$.[87]

For $f \sim 1$ the metallic density of states shown in Fig. 5.1 does not strongly affect the bias dependences of the tunnel photocurrent with respect to the results obtained for Gold surfaces. The reason is illustrated by the band scheme presented in Fig. 5.6. The injection energy $E_g - (1-f)\varphi_b$ (with respect to the semiconductor bulk Fermi level) is constant and equal to $E_g$ since $f \approx 1$. Thus, as shown in the figure, under application of a bias $V$ to the semiconductor there occurs a rigid shift $qV$ of the metal density of states. For a bias larger than about -1 V (right panel of Fig. 5.6) it is sufficient to consider that injection occurs to an energy-independent density of states since tunnelling occurs into the tail of the majority carrier states.

[85] *It has been found [M. Passlack, M. Hong, R. L. Opita, J. P. Mannaerts, and J. R. Kwo, Appl. Surf. Sci.* ***104/105****, 441 (1996)] that Gallium Oxide can passivate the GaAs surface.*

[86] *Another difference between Gold and Cobalt lies in the larger value of the Cobalt work function, shown in Appendix 3. This should not strongly affect the tunnel current which, as shown by Eq. (2.44), depends on the square root of the work function.*

[87] *We cannot exclude that tunnelling of conduction electrons occurs through surface states resonant with the conduction band. [N. Ishida, K. Sueoka, and R. M. Feenstra, Phys. Rev. B* ***80****, 075320 (2009)]*

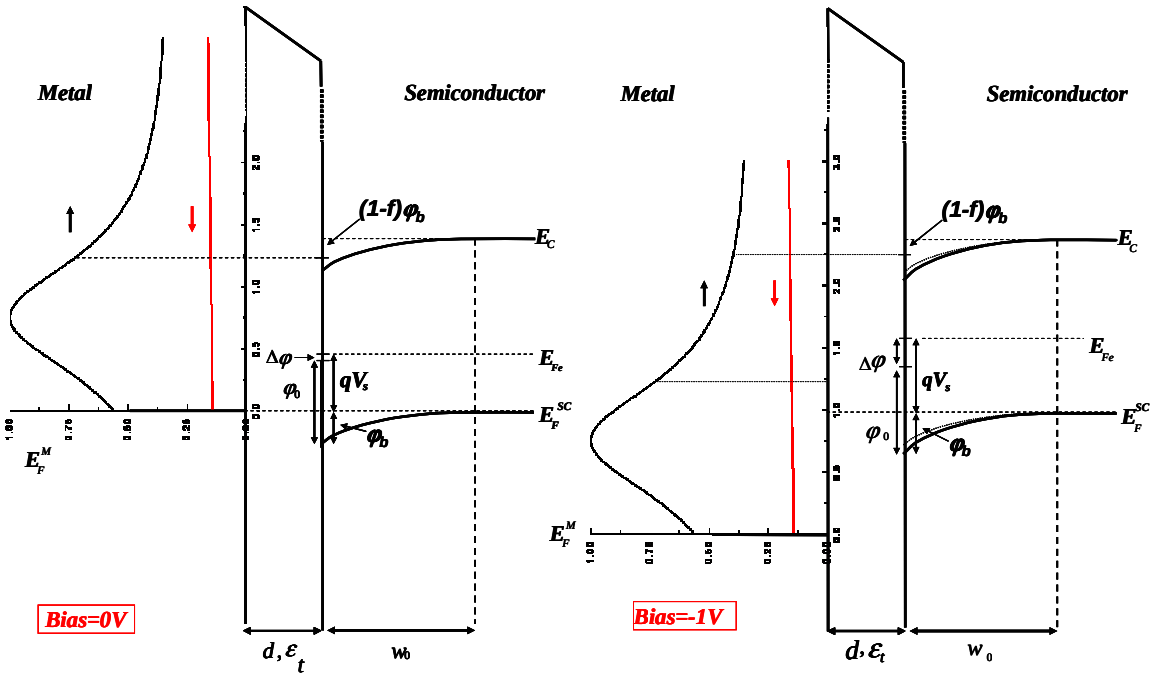


***Fig 5.6:*** *Energy band structures for spin injection into Cobalt. The injection energy $E_g$-(1-f)$\varphi_b$ is shown along with realistic representations of the densities of states of the majority (black) and minority spins (red). The left panel represents the case where no bias is applied, so that the spin-polarised conduction electrons are injected in the top half of the 3d minority spin band. The right panel shows the band scheme for a bias of -1 V applied to the semiconductor.*

The effect of the metallic density of states on the bias dependence of the tunnel current is summarized in Fig. 5.7 which shows the as-measured data and the same data after division by the spin-averaged metallic density of states at the injection energy. This density of states is approximated by a Lorentzian shape of peak energy 0.75 eV and half width 0.6 eV, superimposed on a constant background of amplitude one order of magnitude smaller. It is seen that, as expected from the schema presented in Fig. 5.6, the effect of the metallic density of states is only significant at small bias.

We have compared the bias dependences of the tunnel photocurrent in Fig. 5.4, of the dark current in Fig. 5.3 and of the ideality factor with the model. Unlike Gold, these calculations have been done without performing a correction for the contribution of the non contact part of the surface, since in the case of a relatively thick interfacial layer the contact area must be large in order to ensure that the dark tunnel current be equal to its set value. As suggested by the power dependences of the tunnel photocurrent, we have taken $f = 0.9$.[88] The

[88] *As seen from Fig. 5.5, the exponent of the power dependence of $f_1 \sim 1.1$, is slightly larger than the value $f_2 \sim 0.9$ used for the present analysis. The value of 1.1 cannot be completely explained by quantisation in the depletion layer. Explanations could include tunnelling via surface states or of electrons lying slightly above the bottom of the conduction band in the bulk and will not be considered in detail here. However, the difference $(f_1 - f_2)\ \varphi_b$ between the energies of injection is comparable with kT and quite small.*

values of the parameters used in the calculation are shown in Table 5.1 along with the values used for the spin-dependent results of Sec. IV. Apart from the surface recombination velocity ($S$), all other parameters have constant values identical to those used for Gold. The value used for $S$ is a factor 2 smaller ($S_0$ = 5 x $10^6$ cm/s) in order to qualitatively account for the larger value of $f$. For the dark current we have taken $N_T^d(0) = 4x10^{18}$ m$^{-2}$/eV.

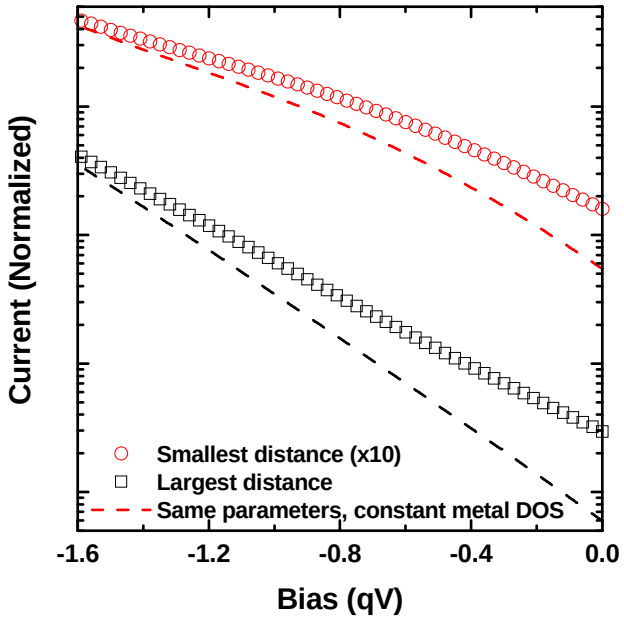


***Fig. 5.7:*** *Effect of the density of states on the bias dependence of the tunnel photocurrent from the conduction band at two different values of $I_{set}$. The dashed lines are calculated by applying a constant DOS (Gold surface), while the dots correspond to a Lorentzian distribution (Co surface), all other parameters being equal.*

The results of the calculations are shown in Fig. 5.3 and 5.4 along with the data. Both for the tunnel photocurrent and for the dark current, the correspondence is very good. The values of the tunnel capacitance $C_m$ and of $\omega$ are almost independent of $I_{\text{set}}$ as expected for mechanical contact. These values approximately correspond to $d$ between 1.2 and 1.5 nm, i. e. larger than for the Gold sample in contact, and $\varepsilon_t \approx 10$. For $I_{set}$ = 0, the smaller values of both $\omega$ and $\varepsilon_0/C_m$ suggest that the thickness of this layer is smaller by about a factor of 2.5. The ideality factor is also accounted for by the model except for $I_{\text{set}}$ = -1000. [89] For $I_{set}$ =0 the large ideality factor for a relatively small tunnel distance can be due to a larger value of the first order corrections ($\alpha_d$) due to the processes which produce a bias dependence of the Schottky barrier. Second order corrections ($\alpha_d'$) due to these processes are quite small.

[89] *Complete interpretation for $I_{set}$= 0 might require adjustment of the surface densities of states. Such interpretation of an isolated result would not be very reliable and was not attempted.*

The value of the dielectric constant suggests that the interfacial layer could be a partial layer of water ($\varepsilon_t \approx 80$) or due to partial oxidation of Cobalt ($\varepsilon_t \approx 12.9$).[90] The thickness of the starting Cobalt layer is evaluated to be about 1 nm, so that formation of 1 nm of Cobalt oxide must leave some unoxidised magnetic Cobalt of about 0.5 nm thickness.

| $I_{set}$ | -3000 | -2000 | -1000 | 0 | 1000 | -1000 (Fig. 5.13) |
|---|---|---|---|---|---|---|
| $\varepsilon_0/C_m$ *(nm)* | 0.15 | 0.145 | 0.16 | 0.065 | 0.12 | 0.074 |
| $\omega$ | 0.059 | 0.057 | 0.062 | 0.025 | 0.047 | 0.033 |
| $n$ | 6.2 | 4.9 | 1.9 | 8.4 | 6.6 | $10 \pm 2$ |
| $\eta$ | 0.3 | 0.21 | 0.21 | 0.21 | 0.15 | 0.18 |
| $\alpha_d$ | 0.14 | 0.01 | 0.01 | 0.085 | 0.01 | 0.085 |
| $\alpha'_d$ $(10^{-3} V^{-1})$ | 0.011 | 0.011 | 0.011 | 0.02 | 0.011 | 0.02 |
| $(\eta-\alpha_d)^{-1}$ | 6.2 | 4.8 | 4.8 | 8 | 6.6 | 10.5 |

***Table 5.1:*** *Values of the parameters used for fitting the tunnel dark current bias dependences of Fig. 5.3 and the tunnel photocurrent of Fig. 5.4 and spin asymmetry dependences of Fig. 5.13. Also shown is the ideality factor (measured at a forward bias larger than 0.2V and the fitting parameters $\eta$, $\alpha_d$, and $\alpha'_d$ as a function of $I_{set}$. Correct fit of the ideality factor implies $n=(\eta-\alpha_d)^{-1}$.*

The tunnel photocurrent bias dependences of Fig. 5.2 were also calculated, as shown in panel c using the same parameter values and $\varepsilon_t \approx 10$. Panel d shows the time dependence of the values of $\varepsilon_0/C_m = d/\varepsilon_t$ found for each scan. It is seen that the increase of $d$ is quite similar to the change of the atomic force and of the tunnel photocurrent at -1.5 V (panel b). The maximum value of $d$ is found to be of the order of 0.7 nm, i.e. comparable with the values obtained in Fig. 5.4. It is concluded that the slow evolution of Fig. 5.2 corresponds to the formation of the interfacial layer.

## *III. Spin-polarisation of injected electrons*

One can anticipate that, for $p^+$ GaAs at room temperature, the average spin polarisation of photoelectrons is of the order of 20%.[91] Evaluation of the effect of diffusion on the spin polarisation has been performed in Appendix A and is illustrated in Fig. A1. This shows that surface recombination can increase the polarisation up to its initial value (50 %) in extreme cases where both the diffusion length and spin diffusion length are larger than the cantilever thickness.

[90] *K. V. Rao, and A. Smakula, J. Appl. Phys.* ***36****, 2031 (1965)*
[91] *K. Zerrouati, F. Fabre, G. Bacquet, J. Bandet, J. Frandon, G. Lampel, D. Paget, Phys. Rev. B* ***37****, 1334 (1988)*

In order to determine the actual spin polarisation of photocarriers created in the cantilever used in the present experiments, we have performed an independent photoluminescence experiment using a conventional system. A circularly-polarised laser beam of energy 1.59 eV and power 3 mW was focused onto the surface of the cantilever. The reflected photoluminescence spectrum was measured with the results summarised in Fig. 5.8. The top panel of this figure shows the spectra of the $\sigma^+$ and $\sigma^-$-polarised components of the luminescence for a fixed helicity of the excitation light. As expected for heavily p-doped GaAs,[92] these spectra exhibit a band-to-band emission peak near $E_G$ = 1.42 eV and a second peak near 1.39 eV due to electron-acceptor recombination. As seen in this figure, the two intensities, $I_{\pm}$, of the components are different and correspond to a luminescence degree of circular polarisation, $(I_+ - I_-)/(I_+ + I_-)$, of approximately 7 % at the luminescence peak. Also shown in the bottom panel of the figure are the spectra of $\mathcal{P} = (I_+ - I_-)/(I_+ + I_-)$ for $\sigma^+$ and $\sigma^-$ polarised excitation. As expected, the polarisations have opposite signs for the two excitation polarisations, with the value of the polarisation only slightly dependent on energy above 1.40 eV. It reaches 10% for an energy larger than 1.45 eV.

For light emission along the z direction, the measured luminescence polarisation, given by Eq. (1.1), is an average over the spin polarisations over the whole thickness of the cantilever and therefore only qualitatively represents the polarisation of injected electrons since this occurs at z = 3μm. As shown in Appendix A, the polarisation at z = 3 μm can be calculated from a resolution of the charge and spin diffusion equations. The values of diffusion length, spin diffusion length and surface recombination velocity are taken from the literature and given in Appendix C. By matching the calculated luminescence polarisation with the measured value, it is possible to extract an estimate for the spin lattice relaxation time, $T_1$ = 0.16 ns. In view of the material dependent correlation time for spin-lattice relaxation, this value is in satisfactory agreement with direct measurements of for $p^+$ doped GaAs, which give $T_1 \approx 0.08$ ns.[93]

[92] *H. D. Chen, M. S. Feng, P. A. Chen, K. C. Lin and J. W. Wu, Jap. J. Appl. Phys.* ***33****, 1920 (1994)*
[93] *K. Zerrouati, F. Fabre, G. Bacquet, J. Bandet, J. Frandon, G. Lampel, D. Paget, Phys. Rev. B* ***37****, 1334 (1988)*

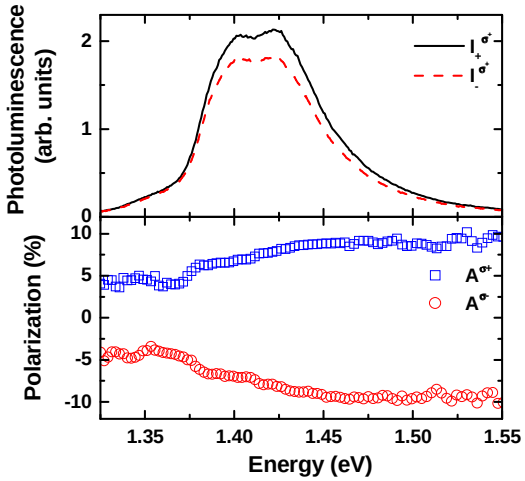


***Fig 5.8:*** *The top panel shows the $\sigma^+$- and $\sigma^-$-polarised components of the luminescence from the cantilever under excitation by a $\sigma^+$-polarised laser at 1.59eV. The bottom panel shows the degree of circular polarisation for $\sigma^+$ and $\sigma^-$ excitations.*

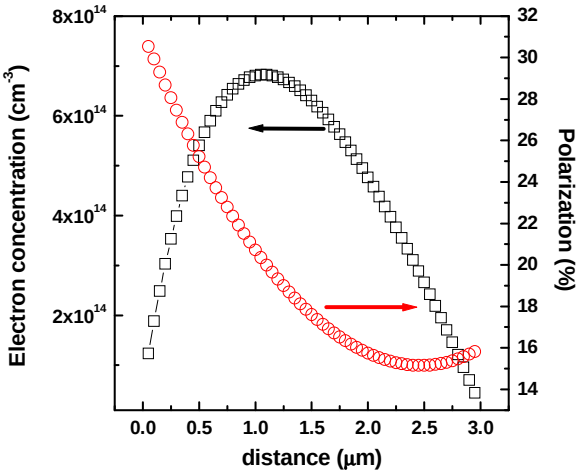


***Fig. 5.9:*** *Calculation of charge concentration and of electronic polarisation as a function of the distance from the photoexcited surface (z = 0).*

Figure 5.9 shows the calculated values of $n_+ + n_-$ and $n_+ - n_-$ (calculated using $T_1$ = 0.16 ns). The concentration and polarisation of the photoelectrons tunnelling from the front face of the cantilever into the metal are $n_+ + n_-$ ($z$ = 3 μm) and $P$ ($z$ = 3 μm), respectively. At the injection face (z = 3 μm) we note that $P \approx 16$ %, from which we expect a spin dependent tunnel effect of the order of several percent. This value will be taken as the polarisation value, defined by the model [Eq. (2.73)], for $\Delta\varphi = 0$ i.e. for a non-reduced surface recombination velocity.

## *IV. Spin-dependent tunnelling*

### *IV.1 Absence of spin dependence for tunnelling into nonmagnetic surfaces*

It is crucial to verify that the tunnel current into nonmagnetic Gold surfaces does not depend on the excitation light helicity as has been previously observed and attributed to helicity-dependent scattering of the light exciting the tip apex.[94]

We have first investigated injection from a silicon tip at the end of an AFM-like Si cantilever into a Gold surface. The tunnel current is found to be very stable. Shown in Fig. 5.10 are 10 black curves showing the asymmetry, $A$, for 1000 individual measurements (as defined in Fig. 3.8) with a red curve showing their average. The averaged asymmetry is less

[94] *R. Jansen, R. Schad, and H. Van Kempen, Journ. Mag. Mag. Mat.* ***198****, 668 (1999)*

than 0.1 %. A similar analysis was performed using GaAs cantilevers on Gold surfaces. Again, as shown in Fig. 5.11 for an average over 100 scans, the residual asymmetry value is less than a fraction of a percent and independent of bias.

In summary, we have observed only very weak parasitic asymmetry signals on non magnetic surfaces which are more than one order of magnitude smaller than previously. This is proof that, although requiring more elaborate technology described in Chapter 3, optical pumping of the rear planar cantilever face enables one to accurately control the geometry of light excitation and therefore to strongly reduce the parasitic signals.

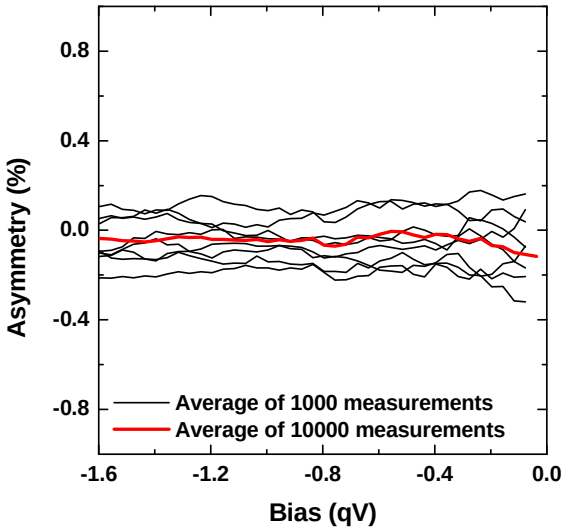


***Fig. 5.10:*** *Injection of photoelectrons from a Si cantilever into a nonmagnetic Gold surface. Since no spin signal is expected, possible asymmetries (as defined by Eq. 2.54) are due to parasitic effects. Each individual curve is averaged over 1000 measurements. No signal is observed, while the noise gives a maximum spin sensitivity better than 0.1 %.*

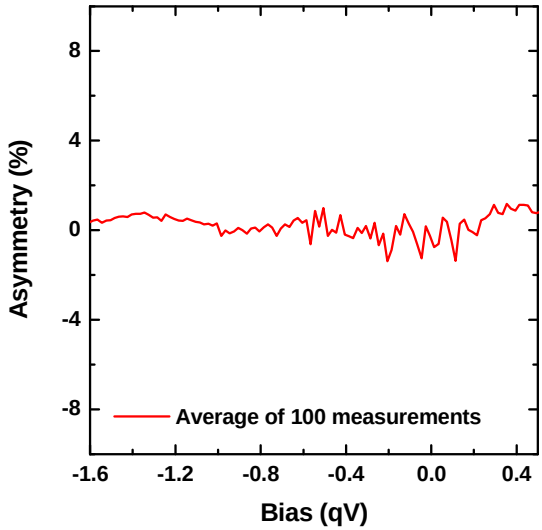


***Fig. 5.11:*** *Very weak asymmetry of the tunnel photocurrent from a GaAs cantilever into a Gold surface.*

### *IV.2 Spin-dependent tunnelling into a Cobalt surface*

We now show the results on spin dependence of the tunnel process, limiting ourselves to $I_{set}$ = -1000 for which the observed instabilities have been found to be the smallest. For other values of $I_{set,}$ it has also been possible to extract spin dependent tunnelling data from individual scans. Since, as shown in Table 5.2, the fitting parameters vary only weakly with $I_{set}$, the results are quite similar to those presented here.

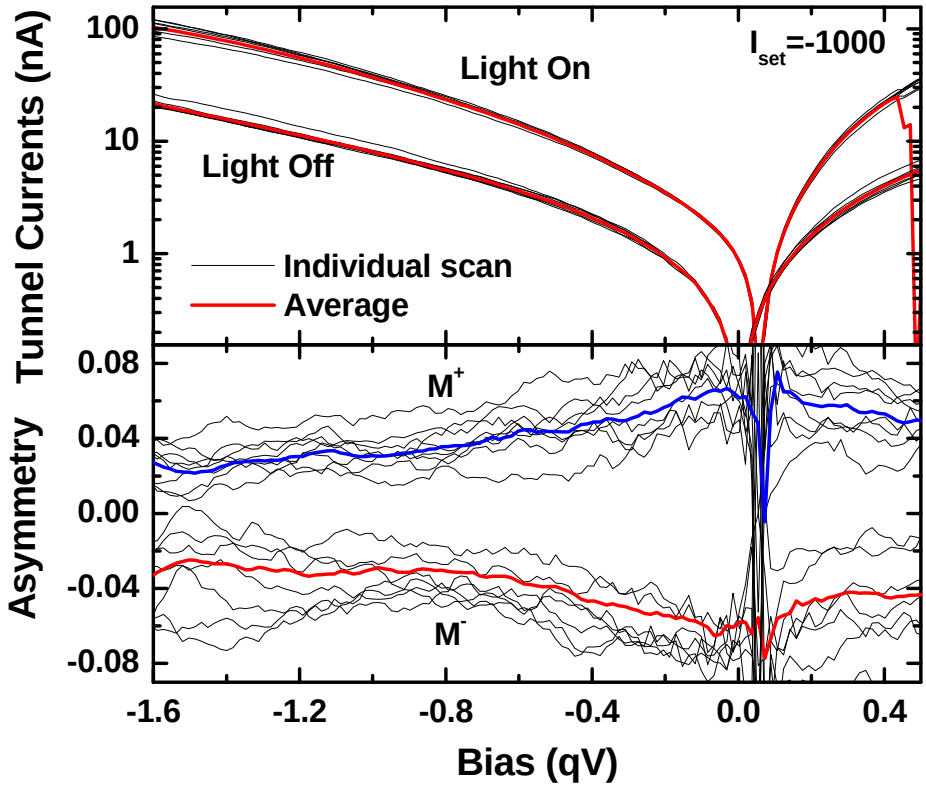


***Fig. 5.12:*** *Spin polarisation of the tunnel photocurrent between a GaAs cantilever and a magnetic Co surface for $I_{set}$ = -1000. The magnetisation of the Co surface is switched from + to - by applying a magnetic field ± B, larger than the coercive field of the sample. As expected, this produces a change of sign of the asymmetry without modifying its bias dependence. Shown in the top panel are the tunnel currents in the dark and under light excitation.*

The top half of Fig. 5.12 presents for reference the bias dependences of the tunnel currents in the dark and under light excitation. Individual scans almost coincide and are quite close to those shown in Fig. 5.4. The bottom half of the figure shows the asymmetry bias dependence after application of a positive magnetic field.($M^+$) Each line shows the results of 10 measurements, as defined in Fig. 3.8. The average of these curves, shown in blue, exhibits a clear signal of about 6 % at zero bias, which decreases with applied bias.[95] The red curve presents the equivalent results obtained after reversing the Cobalt magnetisation via the application of a negative magnetic field. As expected for a spin-dependent tunnel effect, the asymmetry has the same absolute value and bias dependence but an opposite sign.

As seen from Eq. (2.55) and neglecting the asymmetry of the matrix element, the decrease of the asymmetry $A \approx (\delta\rho/\rho)(\delta n_s/n_s)$ as a function of bias can come from the decrease in the asymmetry of the metallic density of states, shown in Fig. 5.1 and Fig. 5.6, or

[95] *The signal-to-noise ratio is smaller at zero bias because of the vanishingly small value of the tunnel photocurrent.*

from that of $\delta n_s / n_s$. Shown in Fig. 5.13 are the averages of dark current (open circles), tunnel photocurrent (open squares, defined as the difference between the light on and light off curves of Fig. 5.12) and asymmetry (open circles).

Tunnel injection concerns states at energies larger than 1.5 eV above the Fermi level, i. e. the high energy tails of the metallic density of states for which $\rho^{min}/\rho^{maj}$ is of the order of 3 or smaller. The relative bias dependence of $\delta\rho/\rho$ is shown in Fig. 5.13 using, as shown in Fig. 5.6, a constant injection energy for the tunnelling electrons, equal to the bandgap. This evaluation, which only depends on the metallic density of states, predicts that $\delta\rho/\rho$ only decreases by about 30 %, whereas the experimentally observed decrease is of a factor of 3.

It is therefore proposed that the spin polarisation $\delta n_s / n_s$ of injected electrons also decreases as a function of bias because of the decreasing surface recombination velocity *S*. This idea has been suggested in Sec. V of Chapter 2: the increase of $\Delta\varphi$ gives rise to a decrease of the concentration of surface states at the electron Fermi level [Eq. (2.73)]. The resulting decrease of *S* induces an increase of the effective lifetime of electrons in the conduction band and therefore to a loss of polarisation by spin-lattice relaxation. From the experimental results and using the bias-induced decrease of $\delta\rho/\rho$, this decrease should be of about a factor 2 over the bias range.

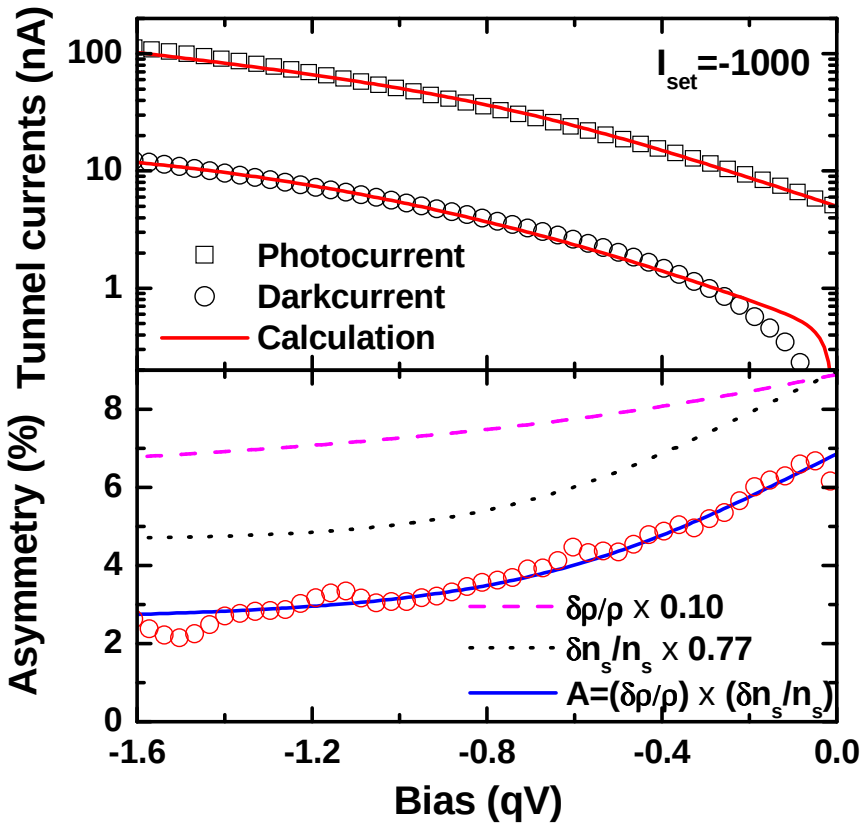


***Fig. 5.13:*** *The top panel shows the averaged bias dependence of the tunnel dark current and tunnel photocurrent of Fig. 5.12, (squares) while the bottom panel (circles) reproduces that of the asymmetry. Calculated values of these quantities are shown by solid lines in the two panels. Also shown in the bottom panel are the normalised contributions of* $\delta n_s / n_s$ *and* $\delta\rho/\rho$ *to the asymmetry bias dependence. It is concluded that the dominant reason for the decrease of the asymmetry under bias is the change of* $\delta n_s / n_s$.

We have calculated the bias dependences of the asymmetry, of the tunnel photocurrent and of the dark current using the model of Chapter 2. As justified in Sec. IV.3 below, for the calculation of the asymmetry bias dependence we only consider here the effect of the decrease of the surface recombination on the polarisation, thus neglecting the spin sensitivity of $S$ [second term of Eq. (2.62)]. Hence

$$\frac{\delta n_s}{n_s} \approx \frac{N_{0s}}{N_0}\frac{v_{ds}}{v_d}\frac{(S+v_d)}{(S+v_{ds})} \qquad (5.1)$$

is not sensitive to the poorly known spin characteristics of the trapping centres. In the same way as for Sec. II above, all parameters are fixed, and the Cobalt density of states is taken as identical to that described in Fig. 5.1.

The values of ω and $\varepsilon_0/C_m$, and the parameters used for the dark current, also shown in Table 5.1, are quite close to those of the curve for $I_{set} = 0$ of Fig. 5.4. The calculation of the spin dependence of the tunnel photocurrent use only one spin-related parameter, the spin diffusion length $L_s$, which is taken to be $L_s = 0.6\ \mu m$ i.e. close to the value

$L\sqrt{\tau_s/\tau} \approx 0.66\,\mu m$ found using the values of $L$ and $\tau$ given in Appendix C and $\tau_s$ obtained above. At large bias for which $S << v_{ds}$ and $S << v_d$ one has $\delta n_s / n_s \approx N_{0s} / N_0$.

The results of the calculations for charge and spin injection are shown in Fig. 5.13 and correspond very well with the experimental results. The predicted ideality factor, shown in Table 5.1, is also close to the measured value within experimental uncertainties. The calculated and measured asymmetry values *at zero bias* are also very close. At low excitation power, the polarisation of injected electrons, $\frac{\delta n_s}{n_s} \approx \frac{N_{0s}}{N_0}\frac{v_{ds}}{v_d} \approx 16\%$ found in Fig. 5.9, gives an asymmetry value $(\delta n_s / n_s)(\delta\rho/\rho)$ of 11% i.e. about a factor of 2 larger than the observed one. This is because, even at zero bias, the surface recombination velocity is reduced for the large excitation power used here so that $\delta n_s / n_s$ is smaller than 16 %.

In summary, the experimental results show the existence of spin dependent tunnelling and strongly suggest that its decrease as a function of bias is due both to the decrease of the spin asymmetry of the metallic density of states and to the decrease of the electronic polarisation induced by the motion of the electron quasi Fermi level. Unambiguous proof of the origin of the bias dependence of the asymmetry would require investigations in a noncontact regime which should give rise to smaller decreases of $\delta n_s / n_s$.

*IV.3 Discussion*

We first justify the fact that spin sensitive surface recombination can be ignored by evaluating the second term of Eq. (2.62). To do so it is necessary to estimate the cross section $\sigma_p$ for hole surface recombination and the spin relaxation time $T_{1s}$ at the surface. Both of these quantities are not well-known but it seems reasonable that $T_{1s}$ is smaller than the value of 0.16 ns used for conduction electrons. A maximum value of $\gamma$ is found by taking for $T_{1s}$≈0.16 ns, and $\sigma_p$ = 2x10$^{-18}$ m$^2$ corresponding to the maximum room temperature value among a wide variety of bulk defects in GaAs.[96] Using the calculated value of the surface hole concentration $p_s$, one finds $\gamma$ < 2 10$^{-3}$. Subsequently, $\delta n_s / n_s$ differs from $N_{0s}\beta_s / N_0\beta$ by less than a few percent, thereby justifying the dropping of the second term in Eq. (2.62).

We now discuss the possible spin-polarised tunnel signal from surface states. As seen from Fig. 5.5, the spin asymmetry $\delta\rho/\rho$ of metallic states at the midgap energy of the semiconductor is larger than for the conduction electrons. However, the small value of $\gamma$

[96] *C. H. Henry and D. V. Lang, Phys. Rev. B* ***15****, 989 (1977)*

obtained here reveals, as seen from Eq. (2.69), only a weak spin polarisation of surface states. This implies that the tunnel current from surface states should also be weakly spin-polarised, so that observation of a large asymmetry is consistent with the dominant role of conduction electrons in the tunnelling process.

Note that the spin dependence of the tunnel matrix element, $\delta K/K$, has been neglected in the analysis of the data. This quantity is not known precisely and could play a role in the value of the asymmetry. Having said this, the good agreement between the calculation and the experimental data at $V$=0 and as a function of $V$ strongly suggest that $\delta K/K << \delta\rho/\rho$. Investigations in the non contact regime for which $\delta n_s / n_s$ should be independent of bias are expected to clarify this point.

## *V. Conclusion*

The results concerning spin-polarised injection into (magnetic) Cobalt surfaces are:

i) Tunnel photocurrent asymmetries of the order of 6% at zero bias are observed in good agreement with the theory. The sign of this asymmetry is reversed when the Cobalt magnetisation is reversed. In contrast, an asymmetry of less than a fraction of percent is observed for spin polarised tunnelling into nonmagnetic Gold surfaces.

ii) The asymmetry is reduced by a factor of about 3 by a bias of -1.6 V. This reduction cannot be entirely due to the decrease of the spin asymmetry of the metal density of states, as estimated by independent spin-polarised inverse photoemission experiments. It is proposed that a significant contribution arises from the decrease of the polarisation of injected electrons. As shown in the model of Chapter 2, application of a bias decreases the surface state concentration at the quasi Fermi level which reduces the surface recombination velocity thereby decreasing the electronic polarisation by spin-lattice relaxation.

iii) The asymmetry was measured in contact so that verification of the above ideas requires further experiments in which the width of the tunnel gap can be varied. Given the difficulties associated with the formation of an interfacial layer, this may require experiments to be performed in ultra-high vacuum or in an inert liquid.

## Summary of Chapter 5.

- The bias dependence of the charge injection between a tipless GaAs cantilever and a Cobalt surface passivated by CO shows that the surface is less inert than for Gold. There forms an interfacial layer (Fig. 5.2) which is likely to be water or Cobalt oxide. Because of this layer the non contact regime cannot be attained.

- A clear spin dependence of the tunnel current is found, which changes its sign if the magnetisation of the Cobalt is reversed : (Fig. 5.13)

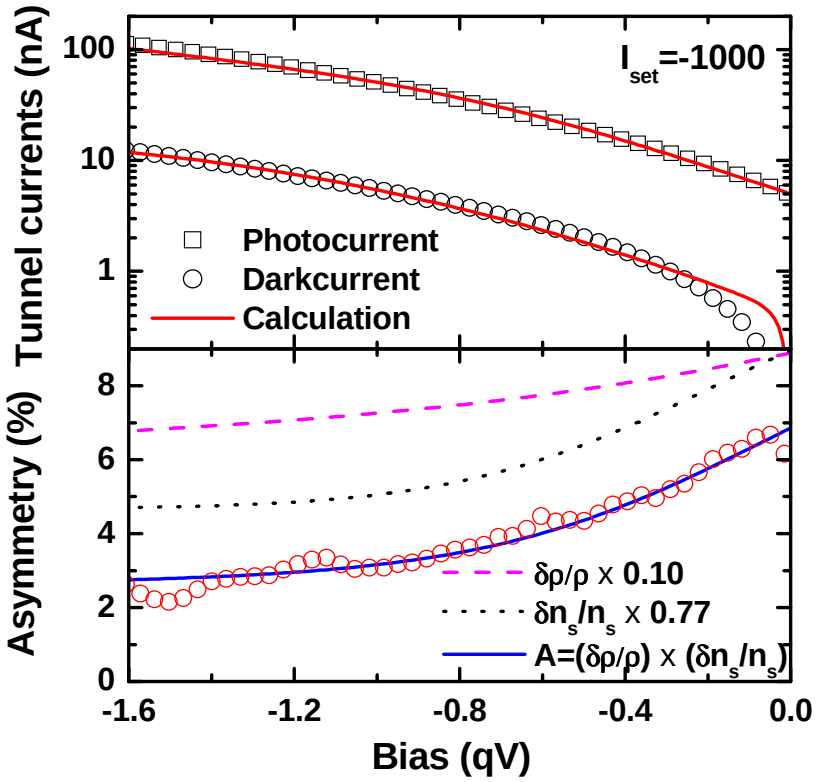


- The decrease with bias of the spin asymmetry is probably not due to the change in polarisation of the metallic density of states but rather due to the decrease in spin polarisation of tunnelling electrons. This caused by the decrease of the surface recombination velocity induced by unpinning of the surface Fermi level.

# Chapter 6: GaAs tips for spin injection

## *I. Introduction*

In previous chapters, I have discussed the tunnel photocurrent and its spin dependence from cantilevers without tips. These results demonstrate that injection of spin polarised electrons from GaAs into metals is possible as revealed by spin-dependent tunnelling into a magnetic metal. In order to achieve magnetic imaging at atomic or nanometric scales, it will be necessary to use an injector with a GaAs tip at the end of the cantilever. A schematic of this injector is shown in Fig. 6.1. The cantilever must be transparent to the light excitation so that its thickness (and therefore its stiffness) can be adjusted without introducing additional light absorption. Ideally the tip must be as sharp as possible for maximum spatial resolution. This type of spin injector has been fabricated by our collaborators at Thales R & T and I have investigated optical pumping in the tip in order to evaluate the electronic concentration and spin polarisation at the apex. The results of this chapter have been published in the Journal of Applied Physics.[97]

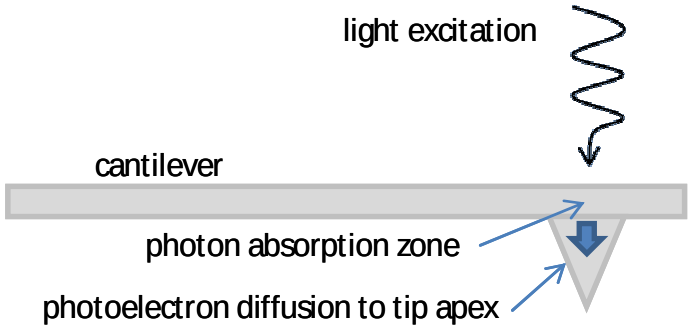


***Fig. 6.1:*** *Principle of a spin injector, composed of a GaAs tip excited by light from its rear and situated at the end of a cantilever which is transparent at the energy of light excitation.*

The main challenge encountered here is that the true electronic spin polarisation inside the tip is difficult to measure via the luminescence polarisation since it is perturbed by total internal reflection from the tip facets. I have therefore determined the spin-lattice relaxation time and bulk recombination time by comparison with planar films of identical doping for which total internal reflection is negligible. The determination of the electron concentration and polarisation at the apex is then obtained by numerically solving the diffusion equations.

The chapter is organised as follows:

---

[97] *D. Vu, R. Ramdani, S. Bansropun, B. Gérard, E. Gil, Y. André, A. C. H. Rowe, D. Paget, J. Appl. Phys.* ***107****, 103101 (2010)*

- In Sec. II, I explain the technology for the fabrication.

- Sec. III shows the results of the photoluminescence investigation of the tip.

-In Sec. IV, I show that the small value of the luminescence polarisation (≈ 1.5 %) is caused by total internal reflection at the tip facets and that this does not modify the electronic spin polarisation. Using a numerical solution of the diffusion equations it is found that, at the apex, this can be as high as the initial polarisation $P_i$ = 50 %.

-In Sec V, I discuss the important parameters for spin injection (tip doping and length).

## *II. GaAs injector fabrication*

### *II.1 Background on tip and cantilever fabrication*

The geometry described in Fig. 6.1 is attractive since it avoids parasitic optical effects caused by front face excitation directly at the apex.[98,99] However, it does require a special fabrication procedure. This process is not compatible with simple tips obtained by cleavage which were used in previous studies[100] and is better adapted to tips defined by anisotropic etching[101] or synthesized by anisotropic crystal growth.[102,103] While micro-cantilevers based on GaAs have been developed for extending the range of applications of Micro Electro Mechanical Systems (MEMS) to the generation and detection of light,[104] these techniques must be extended to the fabrication of cantilevers made of III-V alloys which are transparent to light resonant with the GaAs band gap.

### *II.2 Tip fabrication*

We first describe how a GaAs tip can be grown on a GaAs substrate. In this process the surface of the substrate is coated with a thin layer of $Si_3N_4$ in which holes of typical dimensions 4x4 $\mu m^2$ are defined. This stage is shown in the top graph of Fig. 6.2 (left). The tip is then grown using HVPE (hybrid vapour phase epitaxy). This process involves gaseous GaCl molecules and arsine gas ($AsH_3$) which is thermally decomposed into ($As_2$, $As_4$)

[98] *M. Kuwahara, T. Nakanishi, S. Okumi, M. Yamamoto, M. Miyamoto, N. Yamamoto, K. Yasui, T. Morino, R. Sakai, K. Tamagaki, and K. Yamaguchi, Jap. Journ. Appl. Phys.* ***45****, 6245 (2006)*
[99] *R. Shinohara, K. Yamaguchi, H. Hirota, Y. Suzuki, T. Manago, H. Akinaga, T. Kuroda, and F. Minami, Jpn. J. Appl. Phys.* ***39****, 7093 (2000)*
[100] *M. Bode Rep. Prog. Phys.* ***66****, 523 (2003)*
[101] *K. Yamaguchi and S. Toda, J. Electrochem. Soc.* ***143****, 2616 (1996)*
[102] *R. M. Ramdani, E. Gil, Y. Andre, A. Trassoudaine, D. Castelluci, D. Paget, A. Rowe, and B. Gérard, J. Crystal Growth* ***306****, 111 (2007)*
[103] *G. J. Bauhuis, P. Mulder, H. Van Kempen, J. Cryst. Growth,* ***240****, 104 (2002)*
[104] *N. Iwata, T. Wakayama, and S. Yamada, Sensors and Actuators, A****111****, 26 (2004)*

gaseous molecules when entering the hot wall reactor. The growth reaction for GaAs in an $H_2$ atmosphere is

$$GaCl + \frac{1}{2}As_2 + \frac{1}{2}H_2 \Leftrightarrow GaAs + HCl\ . \qquad (6.1)$$

The attractive features of this growth process are i) no chloride precursors adsorb on the masked surface so that the growth only occurs in the holes.[105] ii) The experimental conditions can be chosen in such a way that growth is governed by surface kinetics.[106] This near equilibrium growth process stops when the GaAs is bounded by the low index facets which exhibit the lowest growth rates. It is possible to adjust the temperature and the ratio of the concentrations of elements III and V so that the tip apex is formed by the intersection of four {110}-oriented facets. The resulting tips are shown in the scanning electron microscope (SEM) images of Fig. 6.2 (middle). These regularly-spaced tips have identical morphologies that are determined by the growth conditions. Also shown in Fig. 6.2 (right) is an enlarged view of a single tip in which the {110} facets are clearly visible. The tip is well-adapted to spin injection since its large base (6 µm) is comparable to the size of a tightly-focussed laser spot. However the radius of curvature of the apex can be up to 10 nm so image resolution will typically be nanometric rather than atomic.

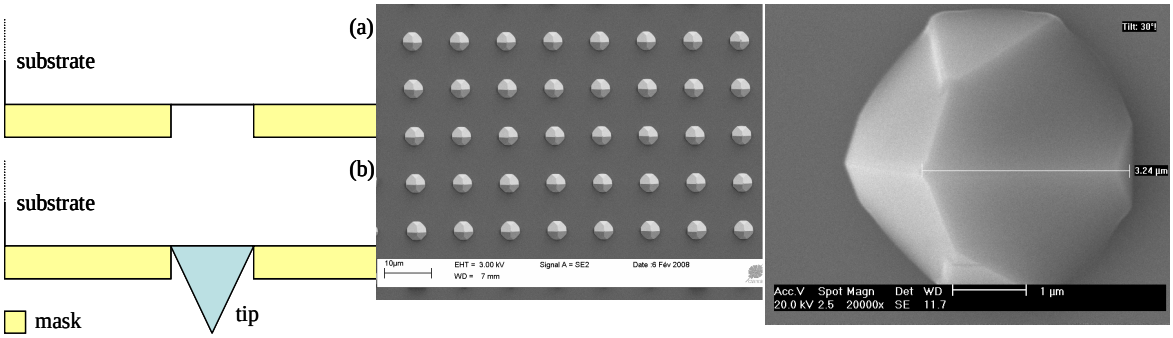


***Fig. 6.2:*** *(Left) Method used for tip growth: in stage (a) the substrate is covered by $Si_3N_4$, with a hole opened in it. In stage (b), the growth of a tip is performed by HVPE. (Middle) a SEM view of multiple tips on a GaAs substrate. (Right) A single tip showing the four {110}-oriented facets which define the apex.*

[105] *E. Gil-Lafon, J. Napierala, D. Castelluci, A. Pimpinelli, R. Cadoret, B. Gérard, J. Crystal Growth* ***222****, 482 (2001)*
[106] *E. Gil-Lafon, J. Napierala, A. Pimpinelli, R. Cadoret, A. Trassoudaine, D. Castelluci, J. Crystal Growth* ***258****, 14 (2003)*

*II.3 Cantilever fabrication*

The spin injector was fabricated in several steps (see Fig. 6.3) on a $p^+$ GaAs substrate about 200µm thick. The tip fabrication process described above constitutes steps (b) and (c). Stage (a) corresponds to the epitaxial growth of the future cantilever. We use $Ga_{0.51}In_{0.49}P$, lattice-matched to GaAs, of band gap larger than 1.8 eV at 300K i.e. transparent for the light excitation of 1.59 eV. The thickness of this layer is 5µm. Since the tip growth is well-controlled only on GaAs, a very thin layer (100 nm thickness) is deposited prior to tip growth.

The last fabrication stage consists of building the cantilever and the body of the structure to support it. This was performed at Thales R & T and is carried out first by depositing a protective dielectric layer into which holes are photolithographic defined, and then by removing the underlying material using inductively coupled plasma (ICP) dry etching process. This procedure has been used twice. In stage (d) the cantilever side faces are defined by a front side etch. In stage (e) the cantilever structure is defined by a back side etch. The ICP process used here gives a typical etch rate of 5-8 µm/min and provides an anisotropic vertical profile over 150-160 µm. A selective wet etchant is then used to etch the final 20-30 µm so that the final surface finish is mirror-like. This promotes a well defined spin polarisation direction normal to this surface and permits a reflected laser beam to be used in an AFM-like setup to monitor the tip-surface force.

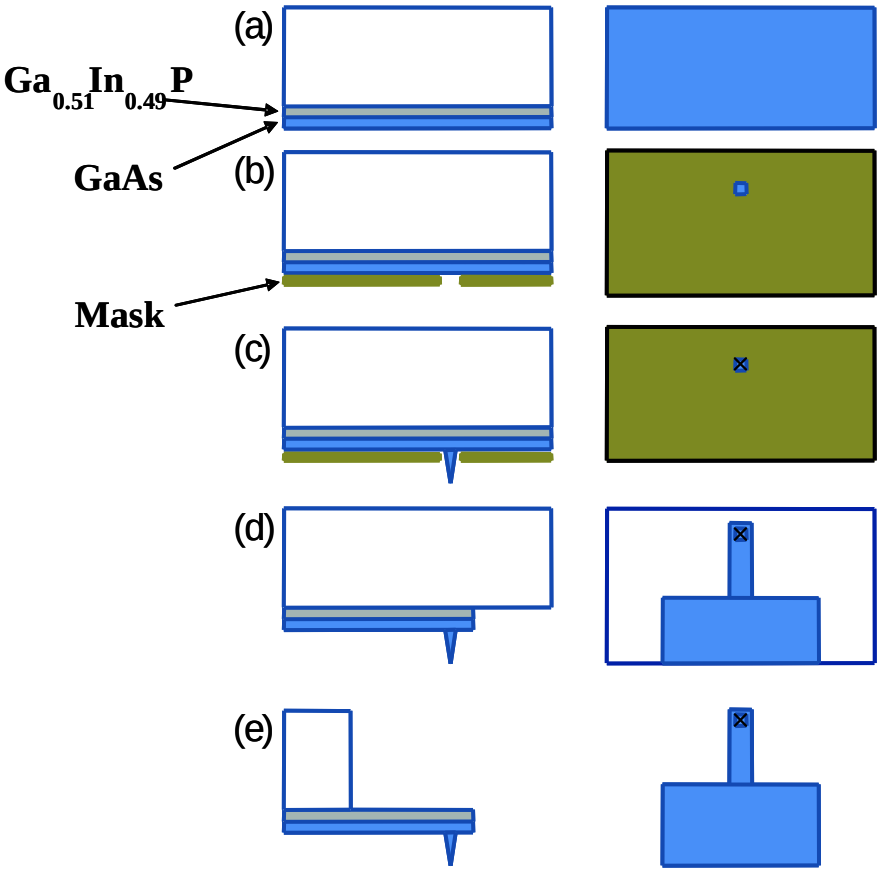


***Fig. 6.3:*** *Injector fabrication process showing side and top views:*
*a) growth of the GaInAs (grey) layer corresponding to the future cantilever and of a thin GaAs layer (blue)*
*b) Deposition of a $Si_3N_4$ layer with a hole to define the tip position*
*c) Tip growth*
*d) Definition of the cantilever by etching from the front surface*
*e) Release of the cantilever by deep vertical etching from the back*

Fig. 6.4 shows a SEM image of spin injectors fabricated using this procedure. On the same GaAs block there are three cantilevers with different lengths or shapes i.e. different stiffnesses. For a rectangular beam of thickness $h$, length $l$ and width $b$, the stiffness is given by the standard equation:

$$k = (3E/12)b(h/l)^3 \qquad (6.2)$$

Here $E$ = 7.9x10$^{10}$ N/m$^2$ is the Young's modulus of $Ga_{0.51}In_{0.49}P$.

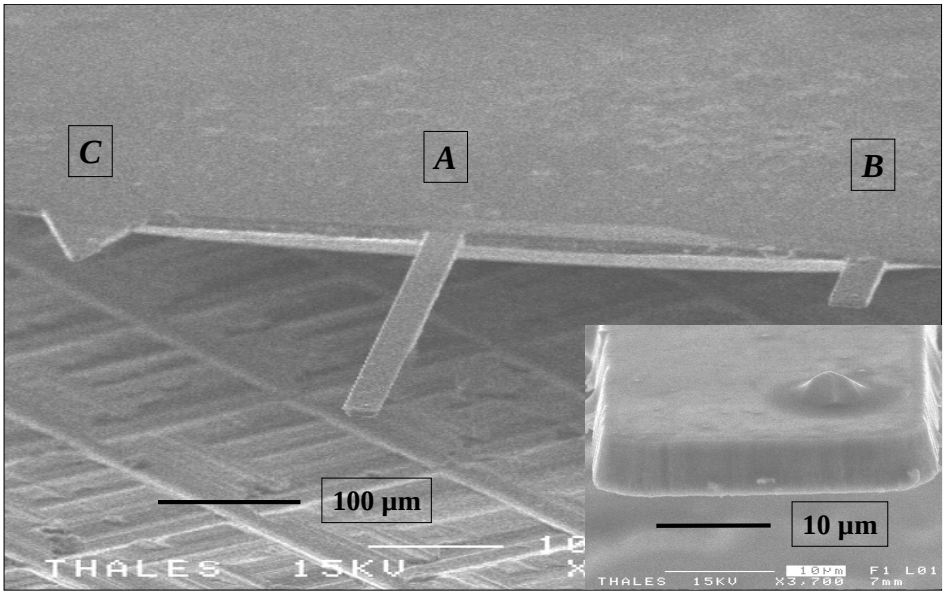


***Fig. 6.4:*** *SEM picture of the GaAs block showing 3 cantilevers of distinct lengths and shapes. The inset shows the end of cantilever B with the tip.*

The cantilever A, of length 400 µm and width 30 µm, has a stiffness of 1.1 N/m and is well-adapted to the control of the tip-sample force using the reflected laser beam in a contact AFM-like configuration. Cantilever B has a smaller length of 100 µm and a stiffness of 74 N/m so that control of the tip-sample distance using the tunnel current is possible. Also available, for measurements where an increased stiffness is required, is the triangular cantilever C of width 100µm at its base. Also shown (inset) is the end of the cantilever B exhibiting, with a slight misalignment, a GaAs tip of height 3 µm and base dimension 6 µm.

## *III. Optical investigation of the GaAs spin injector properties*

### *III.1 Principles*

Injection of the photoelectrons from the tip apex occurs after creation near the tip rear surface followed by diffusion to the apex. In this case three optical effects, as described in Fig. 6.5, could perturb the electronic spin polarisation in the tip.

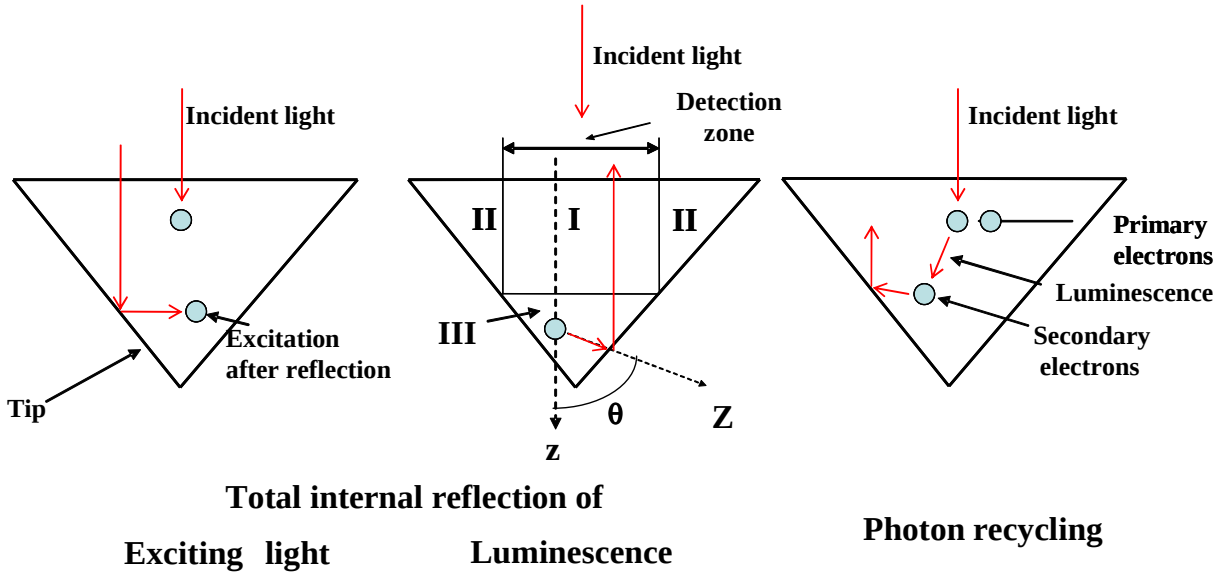


***Fig. 6.5**: Total internal reflection in a tip. The left and centre panels illustrate total internal reflection of the exciting light and of the luminescence, respectively. The right panel shows generation of a secondary electron by re-absorption of a luminescence photon.*

a. Total internal reflection of the excitation light: as shown in the left panel of Fig. 6.5 the tip geometry makes it possible to generate photoelectrons after total internal reflection at the tip surface. Because of the modification of the light helicity after reflection, these electrons can be considered to be unpolarised and thus reduce the overall polarisation. For a laser focussed to a size smaller than that of the tip base, these electrons are mostly generated near the apex, at which the light intensity is attenuated by a factor of the order of $\exp(-\alpha d)$. Here $\alpha$ is the absorption coefficient and $d$ is the base to apex tip height. Since the detected luminescence mostly comes from the other side of the tip this type of effect is not easily revealed optically.

b. Total internal reflection of the luminescence: light collected after reflection from the tip sides can also reduce the circular polarisation of the detected luminescence (centre panel of Fig. 6.5). The polarisation of light emitted at an angle $\theta$ with respect to the $z$ direction is decreased by a factor $\cos(\theta)$. Furthermore, total reflection at the tip surface changes the circular polarisation, so that it is not a bad approximation, for a qualitative estimate, to consider the detected photons unpolarised.

c. Photon recycling: generation of secondary electrons by the re-absorption of emitted photons, known as photon recycling,[107,108] (right panel, Fig. 6.5) could play a significant role in decreasing the luminescence and its polarisation for two reasons. The *initial* polarisation of

[107] *P. Asbeck, J. Appl. Phys.* ***48****, 820 (1977)*
[108] *T. Kuriyama, T. Kamiya, and H. Yanai, Jap. J. Appl. Phys.* ***16****, 465 (1977)*

secondary electrons is $P_i^2 = 0.25$ smaller than the spin polarisation of the recombining electrons. Taking account of the losses by spin relaxation, the steady-state spin polarisation of secondary electrons is very small. As a result photon recycling produces a spin dilution which decreases the overall polarisation of photoelectrons in the tip. In addition, light impinging on the rear tip surface at an incidence angle larger than $\beta_r \approx \arcsin(1/n) \approx 16°$ , where $n$ is the refractive index, undergoes a total reflection and can generate secondary electrons. Thus only a small fraction $(\beta_r/180)^2 \approx 0.8$ % of the emitted luminescence is detectable from the tip rear surface, while the rest of the luminescence can be reabsorbed to create spin-unpolarised secondary photoelectrons.

*III.2 Experimental setup and procedure*

The polarised photoluminescence (PL) properties of the GaAs spin injector B (also seen in the inset of Fig. 6.4) have been analysed using a microluminescence system situated at the Institut d'Optique théorique et Appliquée (IOTA) which was adapted for polarised luminescence studies. This setup is described in Fig. 6.6.[109] The excitation light from a laser at 1.59 eV is focussed at the rear of the tip by a microscope objective with a numerical aperture of 0.25 and a working distance of 5 mm. The resulting laser spot has a diameter of the order of 2µm, i.e. smaller than the base of the tip. The PL and the reflected laser beam are collected by the same objective. A non-polarizing cube beam splitter and a lens enable one to focus the light emission onto a CCD camera. Suitable filters are used to separate the PL from the laser light so that PL images with a spatial resolution slightly less than 1µm are obtained. A second beam splitter is used to send part of the PL to a 50 µm diameter optical fibre connected to the entrance slit of a monochromator. The PL spectra are analysed by a combination of polarisers and quarter-wave plates which can modulate the both the polarisation of the exciting laser and of the PL.

[109] *E. Schwoob, H. Benisty, C. Weisbuch, C. Cuisin, E. Derouin, O. Drisse, G. H. Duan, L. Legouézigou, O. Legouézigou, and F. Pommereau, Optics Express,* ***12****, 1569 (2004)*

a. Alignment of the excitation laser on the tip

As shown in the inset of Fig. 6.4, the tip base is approximately 6 μm large and it is slightly misaligned with respect to the end of a cantilever. Since the tip is excited from the rear and is therefore not directly visible in the image, the control of the laser spot at the tip requires a particular procedure which relies on the presence of a 0.1 μm GaAs layer on top of the cantilever (see step (a) of Fig. 6.3).

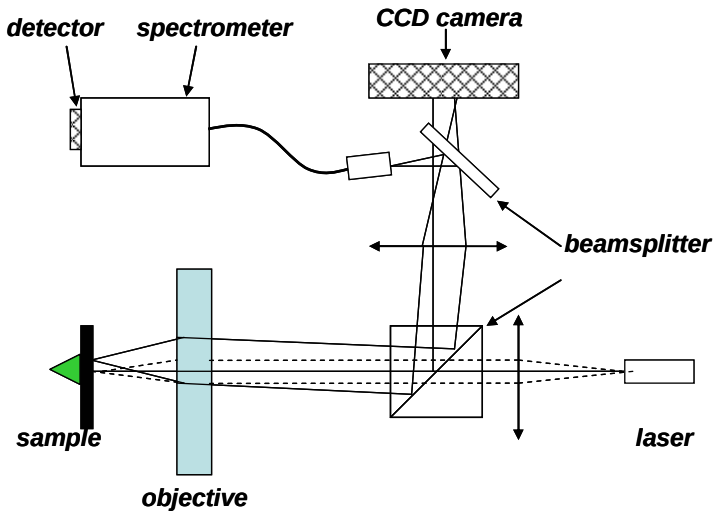


***Fig. 6.6:*** *Experimental setup for spectroscopy and imaging of the tip luminescence. The light excitation is focussed on the rear of the tip by a microscope objective while the luminescence is collected by the same objective. The luminescence is imaged on a CCD camera while a fibre coupled spectrometer enables one to monitor the spectrum of a given area in the image.*

Panel (a) of Fig. 6.7 shows the image taken in the case of a misalignment, when the tip is not directly photoexcited. The PL image and the false colour image are displayed on the left and the schematic interpretation is shown on the right. The emitted photons can be guided inside the thin GaAs layer until they reach the edge of the cantilever or the tip. The edges and rear of the tip are consequently clearly visible in the image so that it is easy to correctly align the laser with the centre of the tip. In the images of the lower panel (b), taken after alignment, the tip emission is clearly visible and its shape coincides with that of the tip. The excitation spot is apparent as a more intense spot close to the tip centre. Taking as a reference the width of the cantilever (30 μm), the rear diameter of the tip is estimated to be around 6 μm.

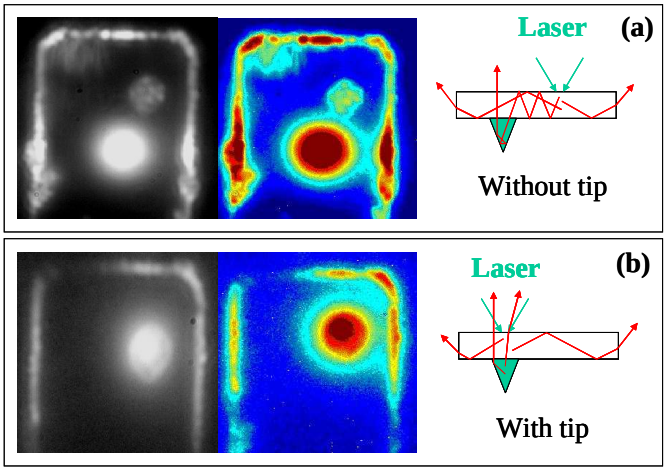


***Fig. 6.7**: Spatial images of the luminescence emitted by the cantilever and tip. In case (a) the laser spot does not coincide with the tip. Both the tip and the edges of the cantilever are however visible since light is guided through the thin GaAs layer. Using this contrast the laser spot can be aligned with the tip center (b). The tip is viewed from the rear of the cantilever so that the image is reversed from the electron microscope view of Fig. 6.4.*

b. Thermal effects

Since heat generated by the laser can only be removed from the tip through the cantilever it must be verified that the sample is not heated by light excitation. This is particularly important since a rise in temperature will tend to decrease the electron spin relaxation time[110] which in turn will reduce the electronic spin polarisation**.** One would like however to have the largest possible photo-assisted tunnel current and as such, a reasonable operating power for an eventual device is the highest excitation power yielding a negligible temperature increase. Fig. 6.8 presents the PL spectra of the tip for three different power densities $P$ = 100, 10 and 1 kWcm$^{-2}$.

[110] *K. Zerrouati, F. Fabre, G. Bacquet, J. Bandet, J. Frandon, G. Lampel, D. Paget, Phys. Rev. B **37**, 1334 (1988)*

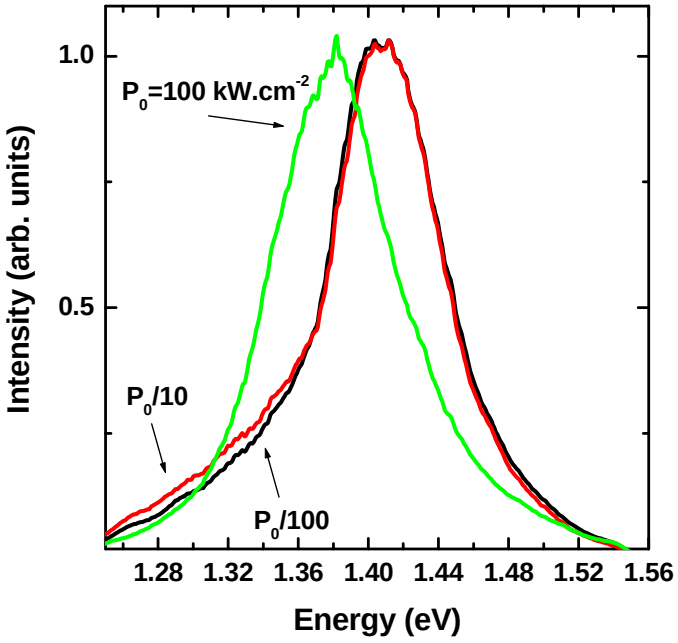


***Fig. 6.8:*** *Tip PL spectra at different excitation powers. The luminescence red shift observed at the maximum power reveals an increase of the tip temperature.*

At a laser power density $P$ = 100 kWcm$^{-2}$, the peak of the PL spectrum is shifted to 1.38 eV. This 40 meV shift corresponds to a reduction of the band gap as a result of an increase in the lattice temperature via Joule heating. Via the Varshni equation[111] the temperature is found to be $T = 390\ K$. This observation is in agreement with a simple estimate of the temperature made using the thermal conductivity of GaAs ($K$=0.55 Wcm$^{-1}$°C$^{-1}$). The optical pumping geometry is shown in Fig. 6.9 where it can be seen that the laser is approximately completely absorbed in a cylinder of 2μm in diameter (i.e. the diameter of the excitation spot) and 1 μm in height (i.e. the penetration depth). The difference in temperature between the absorption zone and the ambient temperature is given by the heat transfer equation,

$$\Delta T = \frac{Pl}{KS}, \qquad (6.3)$$

where $\Delta T$ is temperature difference, $P$ is the excitation power, $S$ and $l$ are the width and thickness of the medium through which the heat transfers. Applying Eq. (6.3) it is found that the tip is heated up to 72°C above ambient when excited by a power density of P = 100 kWcm$^{-2}$. For all results presented below, the light excitation power was sufficiently low so as to avoid heating.

[111] *Y. P. Varshni, Physica (Utrecht)* ***39****, 149 (1967)*

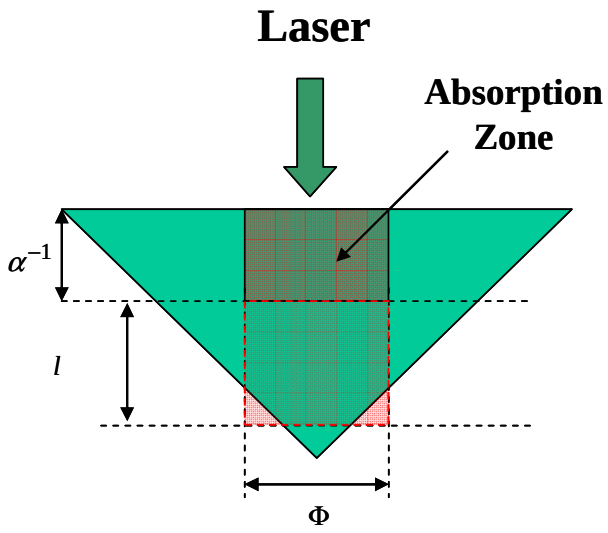


***Fig 6.9**:* Effective excitation geometry for *simulation of the heat transfer process.*

*III.3 Results*

The PL spectrum is shown in the bottom panel of Fig. 6.10. The middle panel shows the polarisation spectra, defined by Eq. (1.1), for a $\sigma^+$ and a $\sigma^-$ excitation helicity. Eq. (1.1) indicates that the two spectra should be identical and of opposite sign. In practice this is not the case as the difference between the two curves is superimposed on a significant signal due to residual birefringence of the objective or of the beam splitter. Since this birefringence affects the two curves in the same way, it is eliminated in the difference spectrum $0.5(P^+-P^-)$. This spectrum is shown in the top panel of Fig. 6.10, which reveals a maximum light polarisation (~ 1.5 %) much smaller than that typical expected for $p^+$ GaAs. It will be seen in the following section that this is due to the geometry related optical effects described above. Importantly, it will be seen that this reduced PL polarisation does not reflect the electronic spin polarisation inside the tip, particularly at the tip apex from which tunnelling will occur.

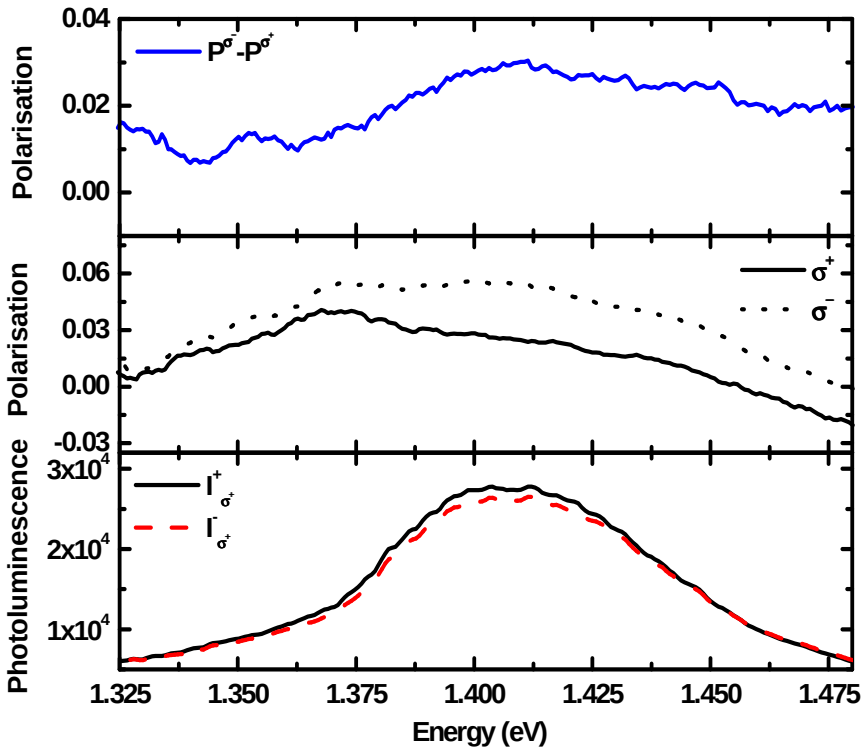


***Fig. 6.10:*** *PL of the GaAs tip. The bottom panel shows the tip PL for a laser beam focussed at the tip centre. The middle panel shows the polarisation spectra for a $\sigma^+$ and a $\sigma^-$ light excitation. The difference between the two curves is due to parasitic birefringence effects in the setup. The top panel shows the half difference between these two spectra with a resulting PL polarisation of 1.5 %.*

## *IV. Evaluation of the electronic concentration and polarisation at the tip apex*

The evaluation of the spin polarisation at the apex is not trivial for three reasons:

- As shown in Eq. (1.1), optical measurements give only an averaged value of the electronic polarisation over the tip.

- This value is modified by the total internal reflection effects discussed above.

- Determination of the acceptor concentration which affects the stationary spin is difficult since acceptor incorporation rates is larger for the (110) tip facets than for the (001) rear facet.[112]

In this section, the photoelectron spin polarisation and concentration at the tip apex are estimated by comparison with a series of planar, p-doped GaAs films of variable acceptor concentrations with thickness $d$ = 3 µm. For these films, grown on semi-insulating substrates in the same HVPE reactor as the tips, the optical parasitic effects discussed in Sec. III are negligible. Their acceptor concentrations $N_A$, measured by Hall-effect, are indicated in Table

[112] *P.R. Berger, S.N.G. Chu, R.A. Logan, E.Byrne, D. Coblentz, J. Lee, N.T. Ha and N.K. Dutta, J. Appl. Phys.* ***73****, 4095 (1993)*

6.1. Their hole-mobilities, also shown in the table, decrease upon increasing $N_A$ and have typical values for $p^+$ GaAs.[113] Note the case of sample J, grown in conditions identical to those of the tip.

| Sample | Doping ($cm^{-3}$) | Hole mobility ($cm^2/Vs$) |
|---|---|---|
| C | $1.9x10^{17}$ | 204 |
| M | $2.7x10^{17}$ | 176 |
| **J** | **$8x10^{17}$** | **139** |
| H | $1.2x10^{18}$ | 113 |
| F | $4x10^{18}$ | 82 |
| D | $1.1x10^{19}$ | 58 |

***Table 6.1****: Doping level and mobility of a series of epitaxial p-GaAs films of thickness 3µm, grown for comparison in the same reactor as the tips. Sample J was grown with the same dopant concentration inside the reactor as the tip.*

The following procedure is used to interpret the experimental results:

i) The doping level $N_A$ is estimated by comparing the tip luminescence spectrum with the spectra of planar films.

ii) The bulk quantities $T_1$ and $\tau$ are taken equal to those of a planar film of identical doping level, determined from the luminescence polarisation.

iii) The electron concentration and polarisation at the tip apex are then estimated by numerically solving the charge and spin diffusion equations [Eq. (A.3) and Eq. (A.4)].

iv) The same numerical treatment allows us to estimate the importance of the effects of total internal reflection illustrated in Fig. 6.5.

*IV.1 Determination of the tip doping from the luminescence spectrum*

The spectra of selected planar samples are shown in Fig. 6.11. For relatively pure samples the spectrum is dominated by band-to-band transitions, with a maximum near the direct band gap $E_g$ = 1.42 eV. For a large acceptor concentration, band-to-acceptor recombination becomes predominant. This effect is known as effective band-gap shrinkage[114,115] and results in a shift of the PL peak to lower energies for increasing doping densities. Comparing the luminescence of the tip and the reference samples, the tip spectrum does not coincide with that of sample J but with that of sample D, for which the doping level

[113] *J. R. Lowney and H. S. Bennett, J. Appl. Phys.* ***69****, 7102 (1991)*
[114] *M. S. Feng, C. S. Ares Fang and H. D. Chen, Mat. Chem. Phys.* ***42****, 143 (1995)*
[115] *H. D. Chen, M. S. Feng, P. A. Chen, K. C. Lin and J. W. Wu, Jpn. J. Appl. Phys.* ***33****, 1920 (1994)*

is higher by one order of magnitude. There is a good correspondence between the spectra of the two samples except for a relatively weak low energy tail in the tip spectrum which could be due to deep acceptors. A possible candidate is the Ga antisite acceptor.[116] These results are summarized in the bottom panel of Fig. 6.12 which shows the peak energy as a function of acceptor concentration for the films together with the corresponding value for the tip. This analysis allows us to conclude that the Zinc doping of the tip is in the high $10^{18}$ $cm^{-3}$ range.

In the top panel of Fig. 6.12, the dependence of the luminescence polarisation as a function of the concentration for all planar samples is displayed. This polarisation increases with decreasing doping level and reaches 16 % for sample C. The 10.5 % found for sample D is much larger than that measured in the tip (~ 1.5 %).

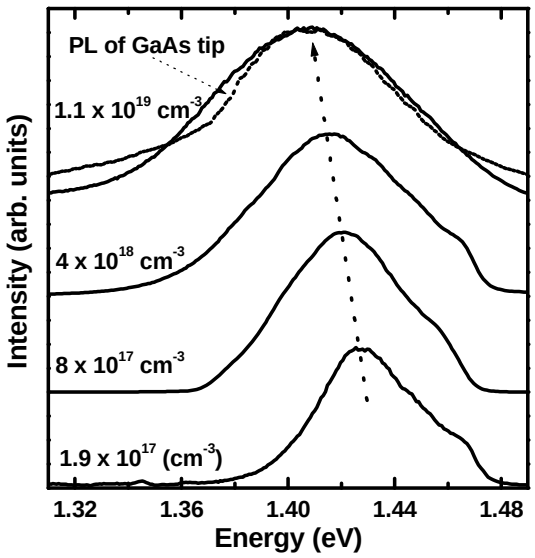


***Fig. 6.11****: Spectra of planar GaAs samples compared to those of the GaAs tip. The red shift of the luminescence as a function of doping reveals the band gap shrinkage. The spectrum of the GaAs tip is close to that of sample D doped at 1.1 x $10^{19}$ $cm^{-3}$.*

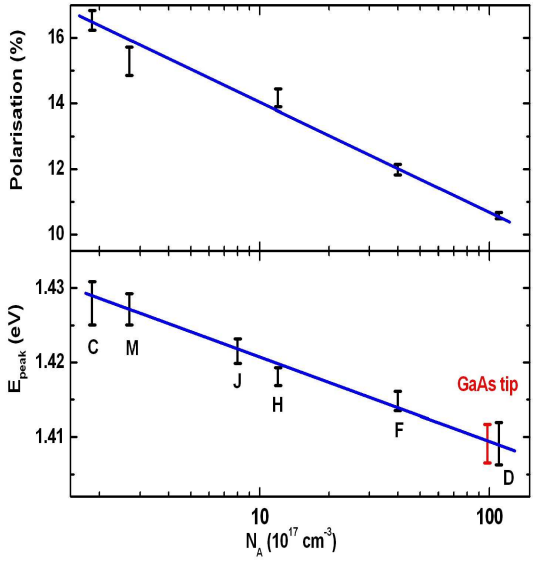


***Fig. 6.12:*** *The bottom panel shows the luminescence peak energy as a function of doping. From the comparison of the values obtained for planar films and for the tip, the tip doping level is estimated to be in the high $10^{18}$ $cm^{-3}$ range. The top panel shows the luminescence polarisation for the films as a function of doping level.*

### *IV.2 Determination of spin-lattice relaxation time and bulk recombination time*

Having determined that sample *D* is the planar film of doping closest to that of the tip, one could think of jointly determining the spin-lattice relaxation time $T_1$ and the bulk electron lifetime $\tau$ from the Hanle linewidth.[117] However, for doping levels in the $10^{19}$ $cm^{-3}$ range, the Hanle linewidth is large and requires the use of very large magnetic fields. Instead

[116] *M. Mihara, M. Mannoh, K. Shinozaki, S. Naritsuka, and M. Ishii, Jap. J. Appl. Phys.* ***25****, L611 (1986)*
[117] *K. Zerrouati, F. Fabre, G. Bacquet, J. Bandet, J. Frandon, G. Lampel, and D. Paget, Phys. Rev. B****37****,1334 (1988)*

the values of $\tau$ found in the literature are used. Although $\tau$ probably depends on the material quality, it is found that the results depend only weakly on the exact value. This is because, in these large surface-to-volume ratio samples, $\tau$ is determined primarily by surface recombination.

*IV.3 Calculation of electron concentration and spin polarisation at the tip apex*

In the planar samples, total internal reflection is negligible and the PL polarisation is calculated numerically using Eq. (1.1), Eq. (A.3) and Eq. (A.4) for several values of $T_1$. The estimated value of $T_1$ is then the one which yields a PL polarisation close to the measured one. For this calculation the light excitation power is fixed at 1 mW focussed over a diameter of 1.5 µm with other parameter values given in Appendix C and Table 6.2. Also shown in this table are the values obtained for $T_1$ and for the electron concentration and spin polarisation at the front surface.

The electron concentration and polarisation at the apex of a conical tip of height 3 µm and base radius 3 µm were then calculated using the same values of the bulk parameters $T_1$, τ, *D* and *L* as for the film. The surface recombination at the tip sides was taken to be identical to that of the planar film, while that of the rear surface, passivated by the $Ga_{0.51}In_{0.49}P$ layer, was taken to be zero. The electron concentration and polarisation at the apex are also shown in Table 6.2 for the tip.

| **Sample** | **Doping ($cm^{-3}$)** | **$\tau$ (ns)** | ***S* (cm/s)** | ***D* ($cm^2/s$)** | ***L* (µm)** | **$T_1$ (ns)** | **$L_s$ (µm)** | **$P_{inj}$ (%)** | **$n_{inj}$ ($cm^{-3}$)** |
|---|---|---|---|---|---|---|---|---|---|
| **D** | $1.1x10^{19}$ | 0.6 | $10^7$ | 25 | 1.2 | 0.17 | 0.57 | 25.8 | $6.1x10^{14}$ |
| **tip** | $10^{19}$ | 0.6 | $10^7$ | 25 | 1.2 | 0.17 | 0.57 | 43.7 | $6.6x10^{12}$ |

***Table 6.2**: Values of parameters which depend on the electron concentration and spin polarisation in the tip and in the planar sample D of similar doping. As shown in Appendix C, the values of τ, S and D are taken from the literature. $T_1$ is found from the luminescence polarisation of sample D.*

The insets of Fig. 6.13 show the geometrical configuration as well as calculated spatial distributions of both the concentration and polarisation. Fig. 6.13 also presents the dependence of the electron concentration and spin polarisation as a function of distance along the excitation direction for the tip and for sample D (denoted plate). In the top panel, at distance z = 0, the concentration is more than one order of magnitude larger than that of the film larger because of the passivating layer. Conversely, since the conical shape enhances the effect of surface recombination, the electronic concentration inside the tip decreases more rapidly than for the film, and at the tip apex is smaller than that at the front face of the film by

about one order of magnitude. Comparison of the spin polarisations of the film and of the tip reveals that the more efficient surface recombination in the tip yields a smaller effective lifetime and therefore a larger spin polarisation. Near the rear surface, the spin polarisation at the film is larger than that of the tip, while near the opposite surface (or near the apex) the tip polarisation is larger. Also noteworthy is the fact that the polarisation increases with decreasing distance to the apex. This effect is due to direct creation of electrons by light absorption near the apex. Since these electrons are created near the surface their effective lifetime is strongly reduced and their polarisation, 44 %, is close to the initial polarisation $P_i$ = 50 %. Although their concentration is small, the concentration of electrons having diffused from elsewhere to the apex is also small because of the reduced diffusion length (see Chapter 7).

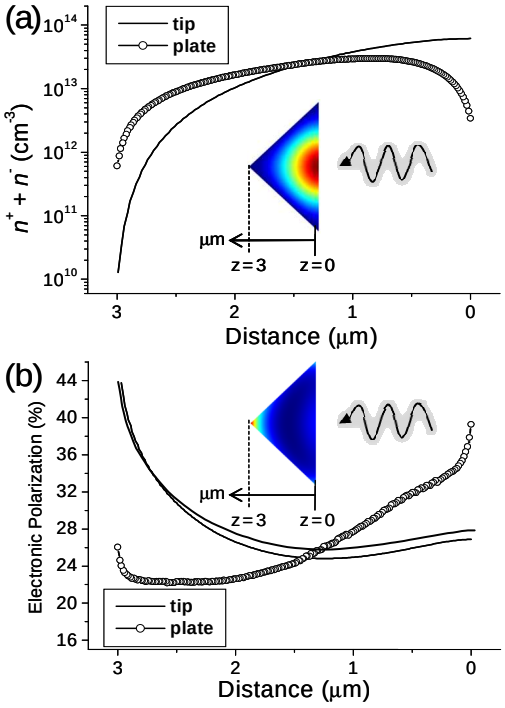


***Fig. 6.13:*** *The top panel shows the calculated concentration along the excitation axis for the tip and for the planar sample D of similar doping. The bottom panel shows the electronic polarisation for the same two cases. Also shown are images of the electronic concentration and polarisation in the tip.*

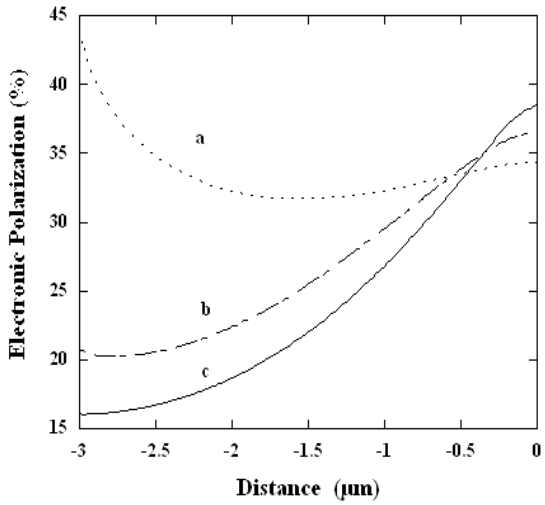


***Fig. 6.14:*** *Effect of the absorption coefficient on the distance dependence of the polarisation in a conical tip. Curve a reproduces the results shown in Fig. 6.13 for the actual value $\alpha = 10^4 cm^{-1}$. Curves b and c correspond to $\alpha = 3x\ 10^4\ cm^{-1}$ and $\alpha = 10^5 cm^{-1}$ respectively. The lack of a polarisation increase with increasing absolute distance for the larger absorption coefficients indicates that the large polarisation near the apex is due to direct absorption of photons near the apex.*

A simple way to verify this hypothesis is to slightly increase the absorption coefficient which will exponentially increase the concentration of electrons created near the tip apex without greatly changing the concentration of those created near the rear face. This analysis is shown in Fig. 6.14 for an acceptor doping level of $10^{19}$ $cm^{-3}$. Curve a, with the actual value $\alpha = 10^4$ $cm^{-1}$, reproduces the data of Fig. 6.13, while curves b and c correspond to $\alpha = 3x\ 10^4$ $cm^{-1}$ and $\alpha = 10^5$ $cm^{-1}$, respectively. For $\alpha = 3x10^4$ $cm^{-1}$ at which the concentration of directly created electrons becomes negligible, the polarisation rise is no longer observed. A further increase of $\alpha$ only brings minor changes to the spin polarisation.

Using these calculations, the PL polarisation of the tip is estimated, using Eq. (1.1), to be 17%, much larger than the observed value (~1.5 %). This estimate ignores the effect of total internal reflection which the following subsection discusses more quantitatively.

*IV.4 Evaluation of the effects of total internal reflection:*

In this subsection, we show that the strong difference between the measured PL polarisation and the estimated one is due to effects of total internal reflection. Since accurate calculations require tedious numerical analysis, the present approach is semi-quantitative, and relies on simplifying physical hypotheses. We discuss successively the three mechanisms described in Fig. 6.5.

a. Total internal reflection of the exciting light

Since a significant number of photons reach the tip apex it is anticipated that, in addition to directly creating carriers in this zone, a comparable number of carriers are created near the apex after total internal reflection (see the left panel of Fig. 6.5). Since this process strongly changes the helicity of the light it can be assumed that photoelectrons created after reflection are weakly-polarised. It is therefore estimated that the actual spin polarisation at the apex should be the average between the values of Curves a and c of Fig. 6.14 which yields a result of the order of 30 %. This is too high to explain the low measured polarisation. The presence of a significant light power near the tip apex will, however, have consequences for the figure of merit of the injector as discussed in Sec. V below.

b. Photon recycling:

The relevance of photon recycling is estimated by assuming that all emitted photons generate secondary electrons. The total number of incident photons per unit time, given by integration over the tip volume:

$$\Phi_0 = \int_{tip} (g_+ + g_-)\varphi(x,y)\alpha e^{-\alpha z} dv \ , \tag{6.4}$$

generates a number of secondary photons per second given by

$$\Phi_1 = \tau_r^{-1} \int_{tip} (n_+ + n_-) dv \, , \tag{6.5}$$

where $\tau_r$ is the radiative lifetime, taken here to be equal to the bulk recombination lifetime $\tau$. Assuming that, after multiple reflections, the initial creation rate of secondary electrons is uniform in space, the total number of secondary electrons $\int_{tip} (n_{2+} + n_{2-}) dv$ is obtained by replacing the first term of Eq. (A.3) by $\Phi_1 / V$ where *V* is the tip volume. The fraction of detected secondary photons with respect to the incident photon flux is given by

$$\eta = \int_{tip} (n_{2+} + n_{2-}) e^{-\alpha_l z} dv \, / \int_{tip} (n_{1+} + n_{1-}) e^{-\alpha_l z} dv \tag{6.6}$$

This factor is smaller than unity because of non-radiative surface recombination. Taking account of multiple generation stages the relative increase of the electronic concentration due to photon recycling is $\eta + \eta^2 + \eta^3 + \ldots = \eta/(1-\eta)$. Assuming that the polarisation of the secondary photons is very small compare to initial polarisation value, the degree of circular polarisation then should be multiplied by a factor $1/[1+\eta/(1-\eta)] = 1-\eta$. Numerically evaluation of this, using the parameters defined in Table 6.2, yields $1-\eta = 0.9$. The decrease of the spin polarisation of photoelectrons inside the tip due to photon recycling effects is therefore unable to interpret the measured weak degree of circular polarisation of the emitted light.

c. Total internal reflexion of the luminescence.

In this experiment the PL is collected by a multi mode optical fibre of diameter 50 µm. As a result, we measure the PL coming from a surface area on the back of the tip whose diameter is about 1µm. In order to be detected, photons must escape from the rear surface at a distance less than 0.5 µm from the centre and at an angle smaller than the collection angle $\beta$;

$$\beta = \arcsin(NA) \approx 14^o \, , \tag{6.7}$$

where NA = 0.25 is the numerical aperture of the microscope objective. Then the angle of incidence inside the tip which can be monitored is

$$\beta' = \arcsin\left(\frac{\sin(\beta)}{n}\right) \approx 10^o \, , \tag{6.8}$$

where $n = 3.3$ is the optical index of GaAs.

The reasoning to be exposed below is semi-quantitative. As shown in the middle panel of Fig. 6.5, the tip can be separated in 3 different zones.

-In zone I, which is a cylinder for which the base is defined by the zone of photon detection, only the fraction $(\beta'/180)^2 \approx 3\text{x}10^{-3}$ of photons reach the surface under an angle of incidence smaller than $\beta'$ and are detected. Some of the remaining photons can be detected after a double reflection near the tip apex, but because of absorption their number is attenuated by a factor $\exp(-\alpha d)$ where $d$ is the tip height. Here these photons will be neglected.

-Zone II corresponds to the tip volume outside the cylinder from which essentially no photons are measured because they impinge the surface outside of the detection zone.

-Zone III corresponds to the part of the tip near the apex. Some of the photons are emitted towards the rear of the tip at an angle smaller than $\beta'$. Their number is small with respect to the corresponding number from zone I and will be neglected. Most photons emitted at an angle at an angle θ larger than $90^\circ$ (see Fig. 6.5) will eventually leave the detection zone I+III and will not be detected. We finally consider photons emitted at an angle θ up to $90^\circ$ that is, in a direction towards the tip apex. In the same way as for a usual catadioptric structure which enhances light emission, it is assumed that most of these photons can be detected after single or double reflection at the tip surface. Such photons have, at emission, a reduced circular polarisation, given by

$$\left|P_\theta\right| = \left|P_i\right| P \cos(\theta) \tag{6.9}$$

Including the polarisation perturbation caused by reflection, most of photons monitored in zone III can be considered as unpolarised. Hence, the overall degree of circular polarisation is significantly reduced. Using Eqs. (A.3) (A.4) and (1.1) we have evaluated the magnitude of the polarisation dilution by integration over zone III. The overall degree of circular polarisation of the luminescence is estimated to be 0.6 %, even smaller than the observed value. The reason is that the number of photons emitted from zone III, although small, must be compared to the number of photons emitted from zone I, multiplied by a small factor $(\beta'/180)^2 \approx 3\text{x}10^{-3}$. It is therefore concluded that the weak circular polarisation of the luminescence is due to total internal reflection of the luminescence near the apex.

It is of utmost importance to note that this does not affect the electron spin polarisation inside the tip (i.e. it is merely a limitation of the optical detection scheme). As a result the predicted 44 % spin polarisation of electrons near the tip apex is very high and may be close to the initial polarisation. Total internal reflection of the laser may reduce this to

about 30% but the value is still significantly larger than that obtained on the planar samples or on bulk GaAs in the stationary regime. These large polarisations are the result of efficient surface recombination for the tip geometry which limits the value of $\tau$.

## V. Discussion

### V.1 Effect of acceptor doping level

It is clear that the tip discussed in the preceding section is not optimal for injection because of its low electronic concentration at the apex. Since this low value is caused by the small value of the diffusion length, it is necessary to increase this length by decreasing the acceptor concentration. It is also seen in Fig. 6.12 that, for films, the reduction of the doping level induces an increase of the PL polarisation.

For planar films of smaller doping level than sample D above, we have reproduced the same calculations as in the preceding section. As shown in Appendix C, $\tau$, $S$, and $D$ are taken from the literature and $T_1$ is determined so as to interpret the value of the luminescence polarisation given in Fig. 6.12. We have also performed the calculations of spin polarisation and electron concentration at the apex of tips of smaller doping, even though such tips have not yet been fabricated. The results are summarized in Table 6.3 below.

| Sample | Doping ($cm^{-3}$) | $\tau$ (ns) | $S$ (cm/s) | $D$ ($cm^2/s$) | $L$ (µm) | $T_1$ (ns) | $L_s$ (µm) | $P_{inj}$ (%) | $n_{inj}$ ($cm^{-3}$) |
|---|---|---|---|---|---|---|---|---|---|
| **D** | $1.1x10^{19}$ | 0.6 | $10^7$ | 25 | 1.2 | 0.17 | 0.57 | 25.8 | $6.1x10^{14}$ |
| **tip** | $10^{19}$ | 0.6 | $10^7$ | 25 | 1.2 | 0.17 | 0.57 | **43.7** | **$6.6x10^{12}$** |
| **H** | $1.2x10^{18}$ | 2.6 | $7x10^6$ | 37 | 3.1 | 0.34 | 1.05 | 32.6 | $8.2x10^{14}$ |
| **H-like tip** | $10^{18}$ | 2.6 | $7x10^6$ | 37 | 3.1 | 0.34 | 1.05 | **41.5** | **$2.9x10^{13}$** |
| **C** | $1.9x10^{17}$ | 19 | $5x10^6$ | 75 | 11.9 | 0.25 | 1.4 | 35.4 | $1.3x10^{15}$ |
| **C-like tip** | $10^{17}$ | 19 | $5x10^6$ | 75 | 11.9 | 0.25 | 1.4 | **40.9** | **$1.4x10^{14}$** |

***Table 6.3:*** *The first two lines reproduce Table 5.2 and show the values of important parameters for planar films and for tips of similar doping, as well as the estimated spin-lattice relaxation time, concentration and polarisation of electrons at the front of planar samples, or at the apex of tips. The rest of the table extends the evaluations to grown planar films of smaller doping levels and to yet-to-be-fabricated tips doped identically.*

When the doping level decreases both the diffusion length and the spin diffusion length are found to increase. However, unlike the diffusion length, the spin diffusion length stays smaller than the tip length (3 µm). Also shown in Table 6.3 are the values of $T_1$ which yield the experimentally-observed luminescence polarisation. $T_1$ is approximately constant independent of doping, suggesting that, as shown by Zerrouati et al,[118] spin-lattice relaxation

[118] *K. Zerrouati, F. Fabre, G. Bacquet, J. Bandet, J. Frandon, G. Lampel and D. Paget, Phys. Rev. B **37**, 1334 (1988)*

occurs through the D'yakonov Perel' process. Although the value obtained here is a factor of 4 larger than that reported by Zerrouati and co-authors, this can be considered as a satisfactory agreement in view of the material dependence of $T_1$.

The values of electron concentration and polarisation at the apex, shown in Table 6.3, suggest the following comments:

Firstly, the electron concentration at the apex increases with decreasing doping level, reaching a significant value of several $10^{14}$ $cm^{-3}$ for $N_A = 10^{17} cm^{-3}$.

Secondly, the electronic spin polarisation at the apex weakly depends on doping and stays close to the initial polarisation 0.5, even for the weak doping level for which the spin diffusion length $L_s$ is much smaller than $d$. In the same way as in Sec. IV, we have determined the effect on polarisation of direct creation near the tip apex. Shown in Fig. 6.15 are the dependences of the polarisation as a function of distance. For the D-like tip already fabricated, the curve reproduces the results of the bottom panel of Fig. 6.13. As shown in the figure, the polarisation increase due to electrons created near the apex can be estimated by extrapolating the curve at small distance. For the C-like tip electrons created near the tip apex weakly increase the polarisation at the apex, (from 36% to 40.9% as seen in Fig. 6.15) so that the majority of electrons which reach the apex have been created near the tip rear. The modification of the polarisation caused by total internal reflection of the laser, discussed in Subsec.IV.3.a, is also quite small.

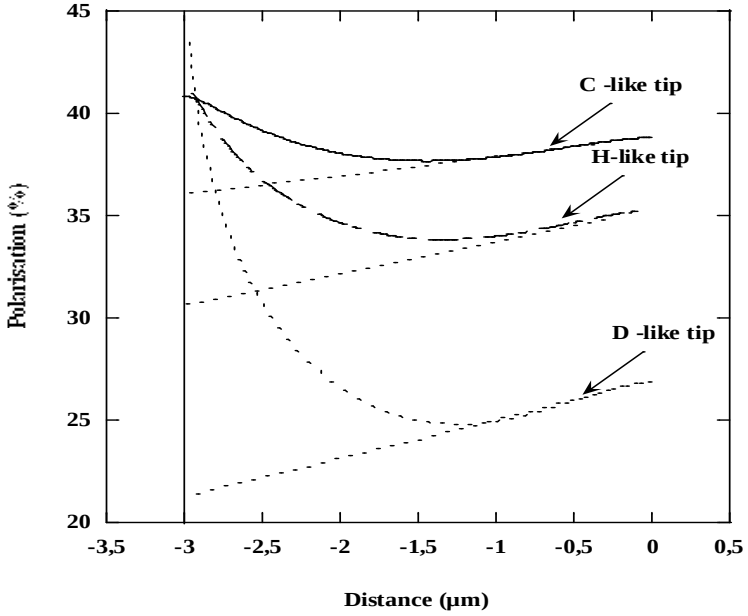


***Fig. 6.15:*** *Dependence of the polarisation as a function of distance for three tip doping densities. For the fabricated, D-like tip doped in the high $10^{18} cm^{-3}$ range, the polarisation increases near the apex because of direct creation of photoelectrons near the apex. For H-like and C-like tips doped in the $10^{18} cm^{-3}$ and $10^{17} cm^{-3}$ range, respectively, this increases is less apparent. For the smallest doping level, the majority of electrons are created near the rear of the tip followed by diffusion to the apex.*

*V.2 Optimal separation of the zones of light absorption and of injection*

As discussed in the introduction the choice of the transmission geometry for the injector aims at minimizing the light field at the tip apex, which has been shown to yield parasitic effects of nonmagnetic origin in tunnelling measurements. It has been shown in the preceding subsection that in the case of a C-like tip (i.e. for a doping level in the $10^{17}cm^{-3}$ range and a tip height of 3 µm), the creation zone lies to the rear of the apex so that tunnel injection can occur only after diffusive transport to the apex. Smaller values of *d* yield a more intense light field at the apex which, as discussed above, produces a spin dilution effect due to total internal reflection of the laser. On the other hand, for larger values of *d* strong losses by surface recombination should decrease the injected current. For these reasons, there should be an optimum in the tip height *d*. In the present subsection, we consider the optimal tip doping level $N_A = 10^{17}cm^{-3}$ corresponding to the C-like tip and discuss the optimum tip height.

Fig. 6.16 shows the dependence of the electron concentration and polarisation at the apex as a function of tip height. As expected from the diffusion equations, the electron concentration is largest for a height comparable with the absorption length $1/\alpha \approx 1$ µm, for which both the absorption is large and the losses by surface recombination during diffusion are reduced. Under the same conditions, as seen in the middle panel of Fig. 6.16, the polarisation decreases monotonically with tip length. Based on this it would seem that the optimal tip length is very short, of the order of 1 µm. However, this would imply an intense light field near the tip apex leading to spin dilution.

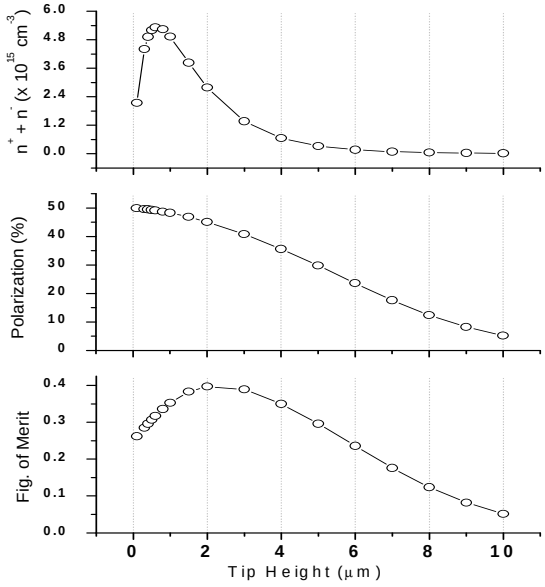


***Fig. 6.16:*** *Effect of tip height for a doping level of $10^{17}cm^{-3}$. The top panel shows the electron concentration and the middle panel shows the spin polarisation at the apex. The bottom panel shows a figure of merit defined in Eq. (6.12), which includes the excitation light present near the tip apex.*

A simple figure of merit for the injector can be proposed, taking into account the fact that light absorption at the apex produces after reflection at the tip faces a concentration $n_0 \approx \xi(n_+ + n_-)\exp(-\alpha d)$ of unpolarised electrons, which is added to the value of $n_+ + n_-$ shown in Fig. 6.16. The quantity $\xi$ depends on the tip geometry, on the diameter of the laser spot and on the diffusion length. For tunnel injection into a magnetic surface, the variation $\delta I_t = I_{t+} - I_{t-}$ of the tunnel photocurrent under modulation of the light helicity is given by

$$I_{t+} - I_{t-} = K(n_+ - n_-) \tag{6.10}$$

where *K* is a constant depending on the surface electronic states. Fluctuations in this current, which limit the measurement sensitivity, are proportional to the total injected current and given by

$$\delta(I_{t+} - I_{t-}) = K(n_+ + n_-)[1 + \xi\exp(-\alpha d)] \tag{6.11}$$

so that the figure of merit, given by $F = (I_{t+} - I_{t-})/\delta(I_{t+} - I_{t-})$, is equal to

$$F = \frac{n_+ - n_-}{n_+ + n_-}[1 + \xi\exp(-\alpha d)]^{-1}. \tag{6.12}$$

It is found that *F* does not strongly depend on the value of $\xi$. Taking $\xi$ = 1, the variation of *F* with tip height is shown in the bottom panel of Fig. 6.16. The proposed figure of merit does not strongly depend on tip length and reaches its maximum for $d \approx 3$ µm. This value corresponds with the actual value of the tip height as fabricated.

## *VI. Conclusion*

In the present chapter, I have presented the fabrication procedure for a local GaAs spin injector. The main results of the investigation of its properties using luminescence and numerical analysis of the diffusion and spin diffusion inside the tip are the following:

- The spin polarisation of photoelectrons at the apex is close to the initial polarisation of 50 %. For the tip of height smaller than the spin diffusion length this large polarisation is caused by the enhanced geometrical effect of surface recombination which strongly decreases the effective photoelectron lifetime. For the same reason the photoelectron concentration at the apex can be relatively small, in particular if the diffusion length is small. It is found that for a doping level in the low $10^{17}$cm$^{-3}$ range the electron concentration at the apex is satisfactory.

-The optimum length is found by taking account of the light field near the apex. It is found that the optimum tip length at a doping level in the $10^{17}$ $cm^{-3}$ range is of the order of 3 µm for which the spin polarisation at the apex is around 40 %.

A key question for imaging applications is the value of the spatial resolution which is expected for these tips. Given the typical radii of curvature for the fabricated tips, the spatial resolution will likely be of several nm. This may allow for magnetic imaging well below the resolution possible with a magnetic force microscope, but will not yield the atomic resolution usually expected of scanning tunnelling microscopes. An alternative process, tip growth using anisotropic etching can yield tips of increased sharpness[119] and this type of tip should be considered in future.

[119] *V. Cambel, D. Gregušová, and R. Kúdela, J. of Appl. Phys.* ***94****, 4643 (2003)*

## Summary of Chapter 6.

- Spin injectors composed of GaAs tips at the end of transparent cantilevers, fabricated by the Spinject consortium, have been tested.

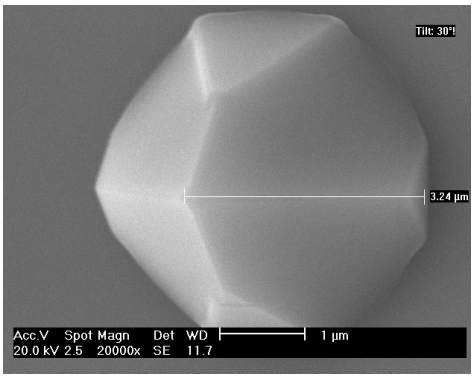


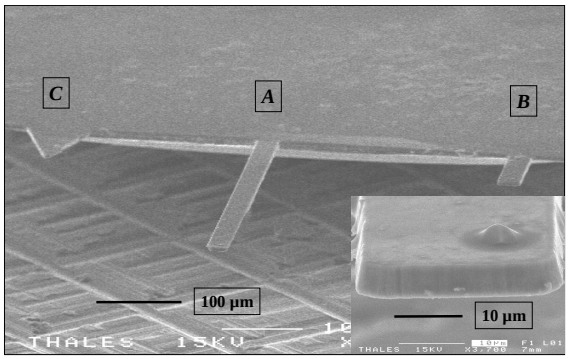


- Photoluminescence and numerical modelling have shown that for a moderately doped tip, of optimal length 3µm, one can expect photoelectron densities of the order of $10^{15}$ $cm^{-3}$ at the apex, of polarisation larger than 40%.

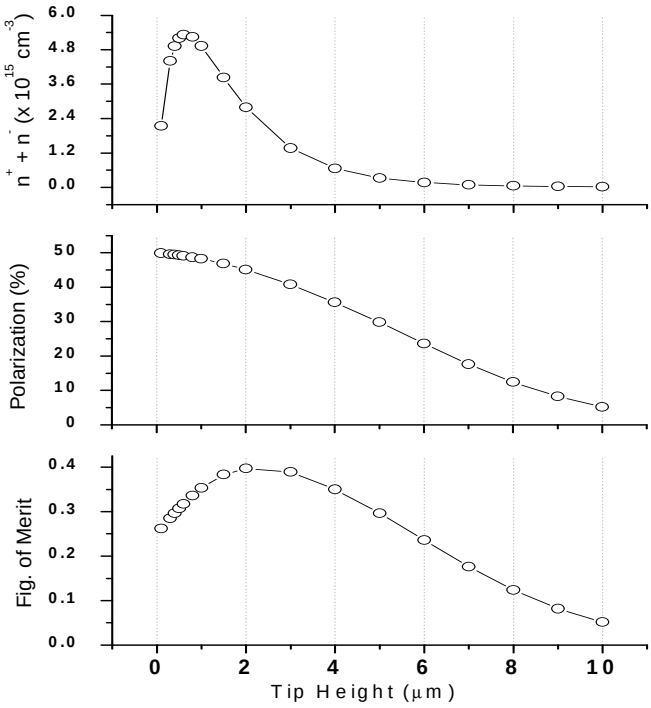


- Surface recombination plays a key role for increasing the photoelectron polarisation.

# Chapter 7: Microluminescence investigation of charge and spin transport

## *I. Introduction*

The present chapter is devoted to the investigation of diffusion and spin diffusion by polarised photoluminescence imaging in substrate-less GaAs thin films. I have undertaken this investigation in order to determine diffusion and spin diffusion lengths which must be accounted for in the design of GaAs tips to ensure a significant spin polarisation at the apex. Intrinsic values of the diffusion and spin diffusion lengths are obtained in a passivated sample in which the surface recombination can be neglected. The equivalent lengths in naturally oxidised samples are strongly reduced by surface recombination. The films were fabricated at the *Institut d'Electronique et de Microélectronique du Nord* using the technology previously described in Chapter 3 for tipless cantilever fabrication. The photoluminescence microscopy method is a powerful and simple technique for jointly imaging charge and spin transport in a wide variety of systems.

This chapter is structured as follows:

-In Sec. II, I review the various imaging techniques for spin or charge transport.

-Sec. III contains the experimental details. It is pointed out that the microluminescence technique applied here to investigate electron transport is identical to the one used in the previous chapter for investigating optical properties of GaAs tips.

-Sec. IV summarises the results obtained on passivated samples while Sec. V contains the study on naturally oxidized GaAs thin films.

## *II. Background*

Optical imaging of charge and spin transport has already been performed by several groups. Three main techniques have been used, which I describe here.

*II.1 Luminescence imaging*[120]

In this experiment, one investigates transport by measuring the image of the luminescence as a function of an applied lateral electric field *E*. Since only the intensity of the luminescence is monitored, only the charge transport is analysed.

The sample is a double heterostructure GaInP/GaAs(0.1μm)/GaInP with a doping level of the GaAs layer of ~$5x10^{18}$ $cm^{-3}$. An incident electron beam at 20 keV is generated by a scanning electron microscope and the applied is an electric field that drifts the minority carriers and hence distorts the luminescence. The luminescence images are observed by an optical microscope connected to a CCD. These images are shown in Fig 7.1 for different electric fields.

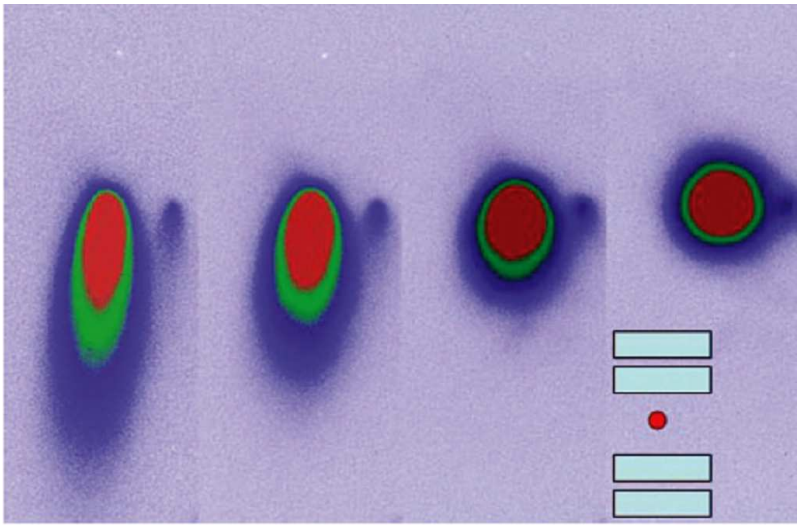

***Fig. 7.1:*** *Cathodoluminescence images (dimensions of each image 87x187 $\mu m^2$) corresponding to electric fields at the centre of 512, 314, 130, and 0 V/cm, respectively).*

While the electron concentration in this two dimensional system is described by a Bessel function (see Appendix C), the concentration at large distance from the centre $x >> 5L$ is approximated by a decaying exponential function, $I = e^{C \cdot x}$ where

$$C = \left(\frac{e}{2kT}\right)E + \sqrt{\left(\frac{e}{2kT}\right)^2 E^2 + \frac{1}{L^2}} \qquad (7.1)$$

Line scans through the centre of the luminescence spot are shown in Fig. 7.2 on a linear scale (a) and on a log-linear scale (b). In (b), the slope is the value of *C*. If the local electric field is accurately known, the diffusion length can be determined directly.

[120] *D. R. Luber, F. M. Bradley, N. M. Haegel, M. C. Talmadge, M. P. Coleman and T. D. Boone, Appl. Phys. Lett.* ***88****, 163509 (2006)*

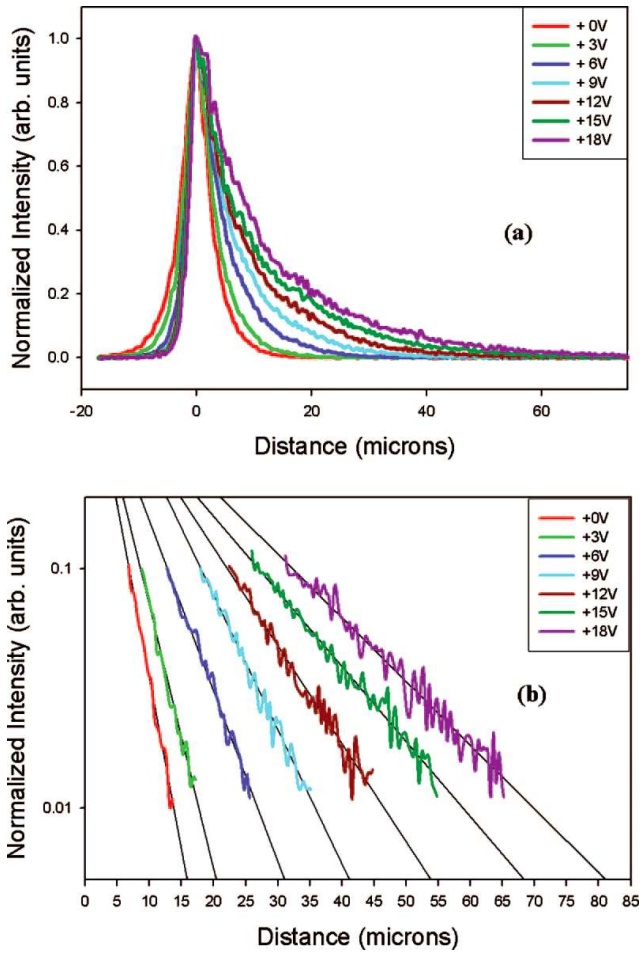


***Fig. 7.2:*** *Cross section of the cathodoluminescence images showing a linear plot (top panel) and a logarithmic plot ( bottom panel). These cross sections enable to determine the diffusion length and mobility of minority carriers.*

The results give a diffusion length of 3.6 µm and a minority carrier mobility of 1150 $cm^2/Vs$ which, for this heavily doped p-type material, agrees with other experimental results and calculations.[121] Time and spatially resolved experiments yield both the diffusion length and the minority carrier lifetime. From this a direct estimate of the diffusion coefficient is possible.[122] Fig. 7.3 shows the luminescence spatial distribution of a GaAs double heterostructure as a function of time after the pump probe. Clearly visible is the Gaussian broadening of the electron packet under diffusion.

[121] *H. S. Bennett, J. Appl. Phys.* ***92****, 4475 (2002)*
[122] *D. J. Wolford, G. D. Gilliland, T. F. Kuech, J. A. Bradley and H. P. Hjalmarson, Phys. Rev. B* ***47****, 15601 (1993)*

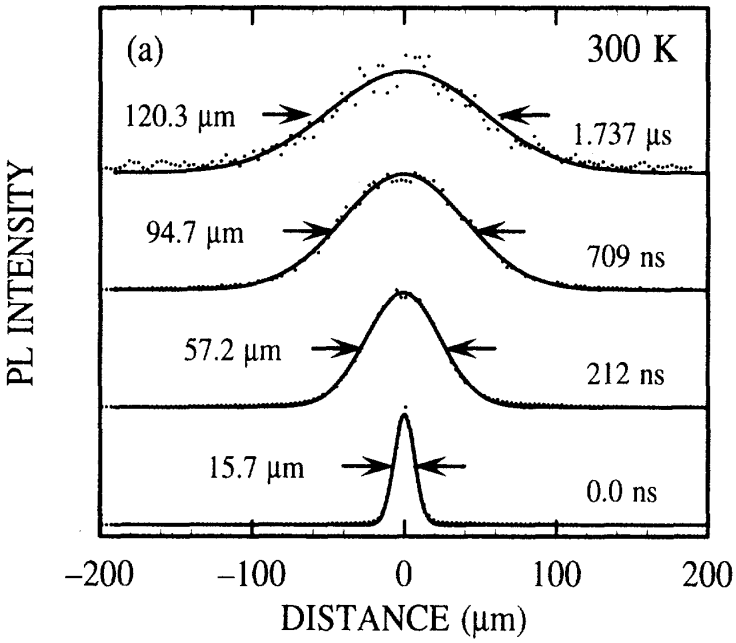


***Fig. 7.3:*** *Time and spatially resolved luminescence distribution showing the diffusion of electrons in a GaAs double heterostructure.*[122]

*II.2 Kerr and Faraday imaging*

Kerr[123] and Faraday[124] effects have been used for imaging spin transport. Both of these methods consist in monitoring the rotation of the linear polarisation of a probe beam which is directly related to the spin component along the incident axis. These techniques do not give any information on charge transport but only on spin transport. While Kerr microscopy monitors the reflected beam, in the Faraday Effect the transmitted light is analysed.

As an example, we describe here the experiments of Crooker and Smith,[123] who have used time resolved Kerr microscopy to investigate spin transport. A 1 μm silicon-doped (n-type) GaAs epilayer grown by MBE on [001]-oriented semi-insulating GaAs substrate is measured at low temperature. A lateral electrical bias is applied in the [110] direction. A steady-state source of electron spin-polarised along [001] direction is injected by a circularly-polarised pump laser beam laser focused to a 4 μm spot and a linearly polarised probe beam is then used to acquire the two dimensional image of the electron spin.

The circular polarisation of the pump beam is modulated from left to right, and the rotation of the polarisation of the probe beam after reflection from the sample surface is monitored. The inset of Fig. 7.4 presents the response as a function of probe energy at a

[123] *S. A. Crooker and D. L. Smith, Phys. Rev. Lett.* ***94****, 236601 (2005)*
[124] *J. M. Kikkawa and D. D. Awschalom, Nature,* ***397****, 139 (1999)*

distance of 30 μm far from the exciting spot. This energy is tuned to the maximum signal, which directly gives the spin of conduction electrons at this point in the image. Fig. 7.4 shows the image obtained by scanning the probe beam over a 70 x 140 μm area. Again, since the experiment is resolved in time and space, an estimate of the diffusion constant is possible.

The spin diffusion and drift are observed in Fig 7.4(b) in which an electric field of 10 V/cm is applied. Line scans at different bias values are shown in Fig 7.4(c). Using an independently measured electron spin lifetime the authors deduce a spin diffusion constant $D_s$ ~ 3 and 15 $cm^2/s$ for $n_e = 1 \times 10^{16}$ and $5 \times 10^{16}$ $cm^{-3}$, respectively, in accord with the charge diffusion constants.

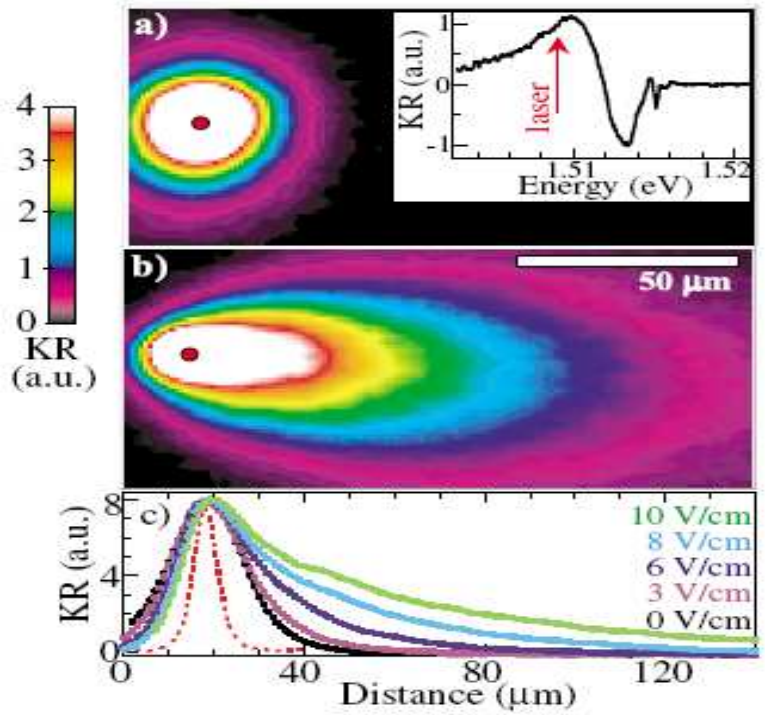


***Fig. 7.4:*** *Investigation of spin transport using Kerr effect. The top panel shows the image of the spin concentration, the middle one represents the modification of this image by application of an electric field. The bottom panel shows line scans across the image for several values of the bias.*

### *II.3 Spin gratings*[125]

Cameron et al. have reported an elegant method for optical investigation of electron and spin diffusion in multiple quantum well semiconductors.[7] In this technique, two crossed-linear polarisation beams are intersected so that, as shown in Fig. 7.5, their interference generates a spatial modulation of the light *polarisation* across the excitation region. As a result, an electron gas of uniform density with spatially modulated spin is created. The spatial

[125] *A. R. Cameron, P. Riblet and A. Miller, Phys. Rev.Lett.* ***76****, 4793 (1996)*

modulation period of the polarised excitation shown in Fig. 7.5(a) and of the electron spin concentration are determined by the light wavelength and by the angle between the two excitation beams.

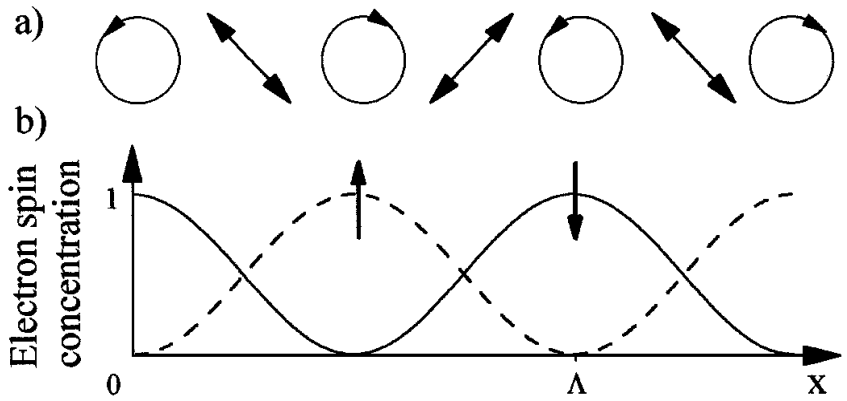


***Fig. 7.5:*** *(a) Polarisation modulation produced by the interference of two orthogonally polarised light beams. (b) Concentration modulation of spin polarised electrons created by the polarisation modulation.*

The spin grating decay occurs both through spin relaxation and through lateral spin diffusion within the quantum well. Its total rate is given by

$$\Gamma = \frac{4\pi^2 D_e}{\Lambda^2} + \frac{1}{\tau_s}, \tag{7.2}$$

where $D_s$ is the spin diffusion coefficient, $\tau_s$ is the electron spin relaxation time and $\Lambda$ is the grating spacing. For a concentration grating created by laser beams of identical linear polarisations, the same expression is obtained by replacing $D_s$ and $\tau_s$ by the charge diffusion coefficient and the minority carrier lifetime.

Since the spin grating results in a diffraction of a probe beam, monitoring the time dependence of this diffraction determines $\Gamma$. The electron spin relaxation time $\tau_s$ can be determined from time-resolved measurements of the diffracted beam as shown in the inset of Fig. 7.6 (a). Repeat measurements of $\Gamma$ with different incident beam alignments (i.e. variation of $\Lambda$) permit the determination of both the lifetime and the diffusion constant. The left panel of Fig. 7.6 presents the measured diffracted signal decay rate for a 5 μm concentration amplitude grating (black circles) compared with corresponding electron spin grating (white circles) when the estimated excess carrier density was of the order of $10^{16}$ $cm^{-3}$. The time decay constants were found to be 120 ps and 13 ps for the charge and spin. The decay rates are then measured as a function of the grating spacing and the results are shown in the right panel of this figure. The electron diffusion coefficient deduced from the gradients is in good agreement with previous studies.

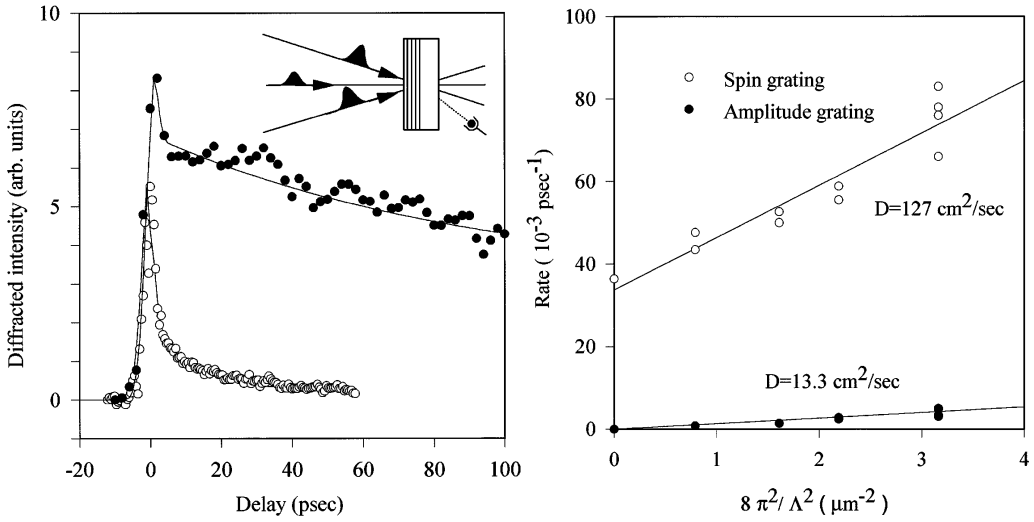


***Fig. 7.6:*** *(Left) Diffracted delayed signal for a 5 μm concentration amplitude grating (black circles) and spin grating (white circles). (Right) Measured decay rate of amplitude and spin grating as a function of grating spacing. The gradients deduces the diffusion coefficient which obeys Eq. 7.2*

## *III. Experimental*

### *III.1 Principle*

In the present photoluminescence experiment, we consider thin $p^+$ GaAs layers where a spin-polarised population of electrons is created by a tightly-focussed steady-state circularly-polarised light excitation. Electron transport and spin transport are investigated using the analysis of images of $I_+ + I_-$ and $I_+ - I_-$, where $I_+$ and $I_-$ are the $\sigma^+$ and $\sigma^-$ polarised components of the luminescence intensity (PL). This analysis gives the spatial dependence of the concentrations $n_\pm$ of photoelectrons of spin ± along the direction z of light excitation since, provided the concentration of photocreated holes is smaller than the acceptor concentration, one has

$$I_+ + I_- = K(n_+ + n_-) \qquad \text{and} \qquad I_+ - I_- = KP_i(n_+ - n_-)\,. \tag{7.3}$$

The constant *K* only depends on the ratios of the radiative to nonradiative lifetimes and on the parameters of the luminescence detection.

Because of diffusion, the luminescence is detected well beyond the extension of the laser beam and by monitoring its decay as a function of distance one can determine the diffusion length. In the same way, the monitoring of $I_+ - I_-$ gives access to the spin diffusion length. The principle of the present experiment is thus analogous to the one described in Sec.

II.1, with the noteworthy exception that the images give independent access to charge and spin diffusion. Note that the *spatially-averaged* electronic polarisation

$$<P>= P_i^{-1}\ (<I_+>-<I_->)/(<I_+>+<I_->) \tag{7.4}$$

is equal to $P_i\tau_s/\tau$ since diffusion does not introduce an additional spin relaxation mechanism. Thus one should have

$$< P >= P_i\left(L_s / L\right)^2 \tag{7.5}$$

which is a simple relation between independently measured quantities.

For these investigations we have used a system analogous to the one described in Fig. 6.6. This system, shown in Fig. 7.7, was subsequently built in my laboratory by adapting a Nikon optical microscope. It uses the same CCD and excitation source as that used in the experiments reported in Chapter 6. The samples are excited with a 50 μW elliptically polarised laser ($P_{las}$ = 70 %) centred at 780 nm and focussed through a x100 microscope objective to a Gaussian spot of half width, $w$ = 0.9 μm. An image of the sample under excitation by the laser is shown in Fig. 7.8. The shape of the GaAs thin film is exactly the same as the one used for injection in Chapters 4 and 5, with the exception that the cantilever is not overhanging the substrate and that here the laser is focussed at the centre (see Fig. 7.8).

Investigations of the PL spectra are important in order to verify that light at the laser energy has been appropriately rejected and to confirm that any local heating of the sample by the focussed laser beam is negligible. Here, the PL spectra are obtained via a 50 μm diameter optical fibre whose diameter corresponds to a spot of size 0.5 μm on the images.

The samples studied here are 3 μm thick *p*+ doped GaAs thin film patches deposited onto SiC substrates. The lateral dimensions of each patch, 400 μm x 400 μm, are sufficiently large that edge effects can be neglected. Two distinct samples were analysed. In one case ($N_A$ = $10^{18}$ $cm^{-3}$) the two surfaces are covered with the native oxide and in the other ($N_A$ = 1.5 x $10^{17}$ $cm^{-3}$) they are terminated with 50 nm thick layers of $Ga_{0.51}In_{0.49}P$. The main effect of the different surface terminations is to modify the surface recombination velocity from $S$ = $10^7$ cm/s for the oxidised sample[126] to approximately $S$ = $10^3$ cm/s for the "passivated" sample.[127] The resulting modification of the effect of surface recombination on diffusion length has been discussed in Appendix A and is summarised by Eq. (A.37).

[126] *H. Ito and T. Ishibashi, Jap. J. Appl. Phys.* ***33****, 88 (1994)*
[127] *J. M. Olson, R. K. Ahrenkiel, D. J. Dunlavy, B. Keyes and A. E. Kibbler, Appl. Phys. Lett.* ***55****, 1208 (1989)*

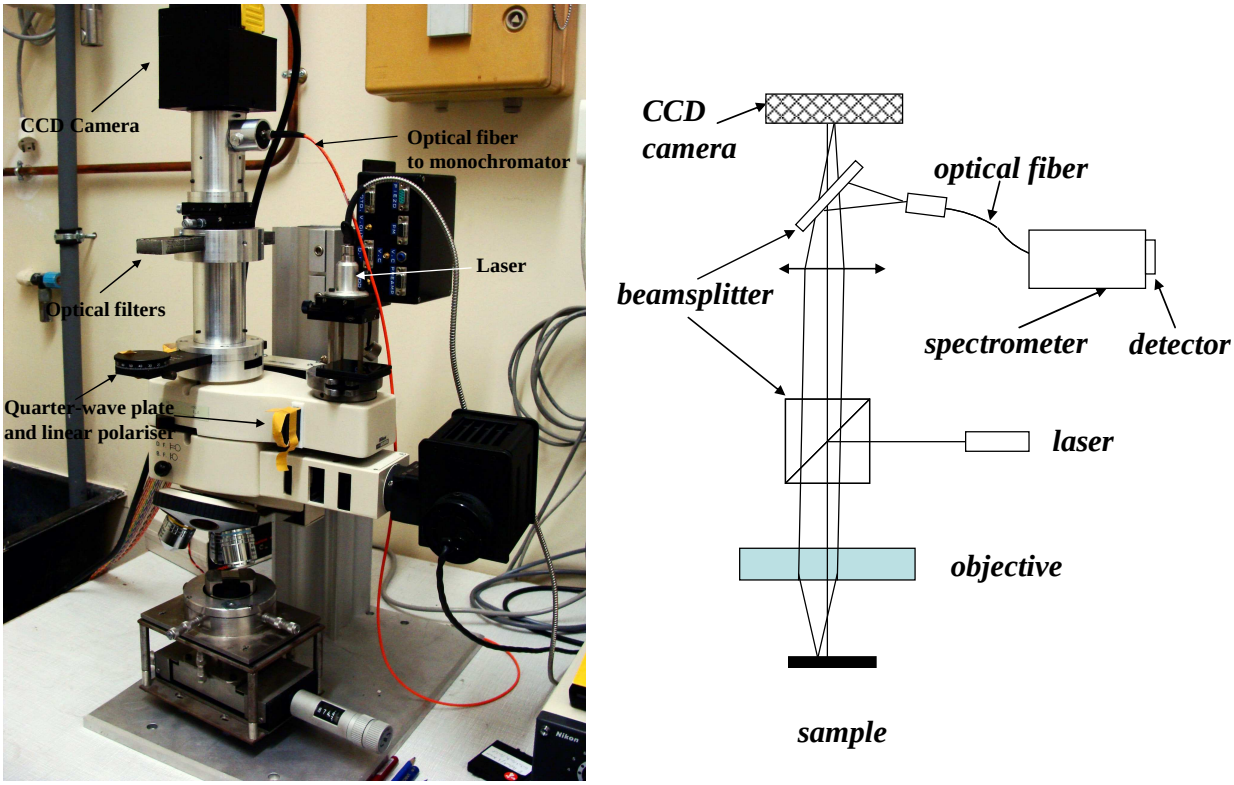


***Fig. 7.7:*** *Experimental setup used for investigating charge and spin transport using luminescence imaging. The right panel shows the functional scheme of the experiment, identical to that used in Fig. 6.6.*

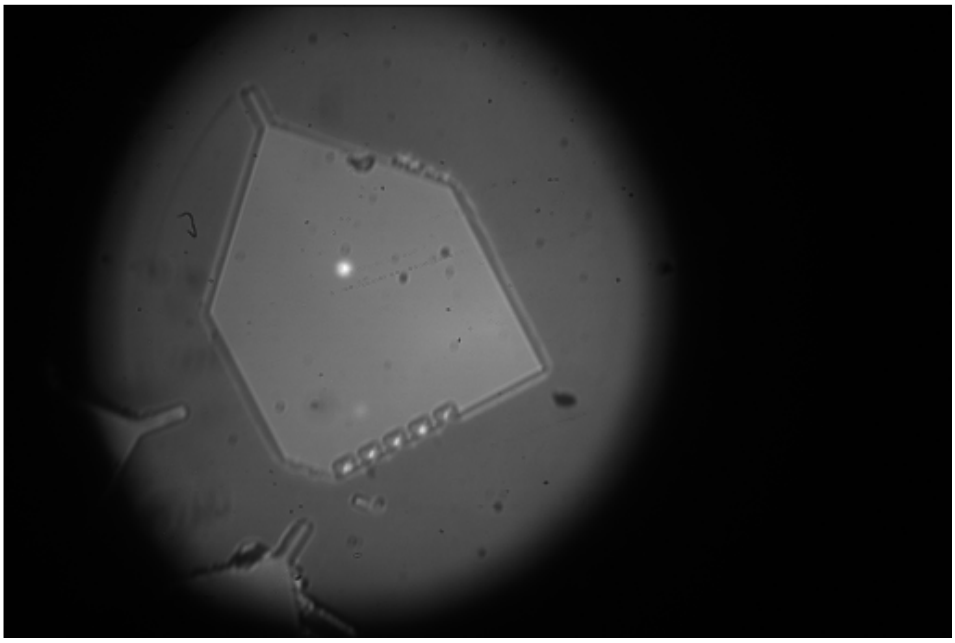

***Fig. 7.8****: A white light image of the GaAs thin film with the laser spot shown in the centre.*

*III.2 Experimental procedure*

Several potential experimental limitations must be addressed. Firstly, correct and accurate subtraction of the dark current image must be performed since a precise determination of the diffusion length requires the measurement of the luminescence decay over the largest dynamic range possible. Incorrect determination of the dark current image will strongly affect the low intensity pixels in the luminescence image. Here, the dark image is taken at approximately the same time as the luminescence image, with the same exposure time but with the shutter closed. Secondly, for measurements near the excitation spot, vertical diffusion over a distance larger than the effective depth of field of the microscope objective results in a defocused luminescence spot. This may induce systematic errors in the estimated diffusion length. It is therefore important to use thin layers of thickness $d \leq l$ x $n$ where $l$ is the objective depth of field and $n$ is the refractive index of the semiconductor. Since one has here $l \sim 0.4$ μm and the samples are 3 μm thick, this source of spatial broadening should be limited. Thirdly, it is necessary to characterise and eliminate the residual birefringence in the optical path. The birefringence of the objective is responsible for an incomplete circular polarisation of the laser ($P_{las}$ = 70 %). Since the signal due to this birefringence is independent of the excitation light polarisation, two series of images (intensity and polarisation), taken for $\sigma^+$-and $\sigma^-$ polarised excitations, can be combined to eliminate the residual birefringence in the measured luminescence polarisation. The resulting four images, denoted $\sigma^{++}$, $\sigma^{+-}$, $\sigma^{--}$ and $\sigma^{-+}$ are combined to form a sum image ($I_s = [\sigma^{++} + \sigma^{+-} + \sigma^{--} + \sigma^{-+}]/2$) and a difference image ($I_d = [\sigma^{++} - \sigma^{+-} + \sigma^{--} - \sigma^{-+}]/2$). These images are defined as

$$I_s = [\sigma^{++} + \sigma^{+-} + \sigma^{--} + \sigma^{-+}]/2 \approx 2K(n_+ + n_-)$$
$$I_d = [\sigma^{++} - \sigma^{+-} + \sigma^{--} - \sigma^{-+}]/2 \approx 2KP_i(n_+ - n_-) \quad (7.6)$$

and will be taken, according to the above equations, as images of the quantities $n_+ + n_-$ and $n_+ - n_-$, respectively.

## *IV. Passivated sample*

For a passivated sample where $S$ is very small, as shown in Eq. (A.37), the value obtained for $L$ is the *intrinsic* charge diffusion length. The sum and the difference images are shown in panels a and b of Fig. 7.9 respectively. Panels c and d show respectively the angular averaged profiles (open circles) of the decay of $I_s$ and $I_d$ for the passivated sample with radial distance, from an origin corresponding to the centre of the PL spot. In the case of $I_s$ the spot

extends over more than 100 μm laterally, far larger than *w*, the width of the laser spot (see dotted line for laser profile). This is the result of diffusion of photoelectrons described by Eq. (A.3).

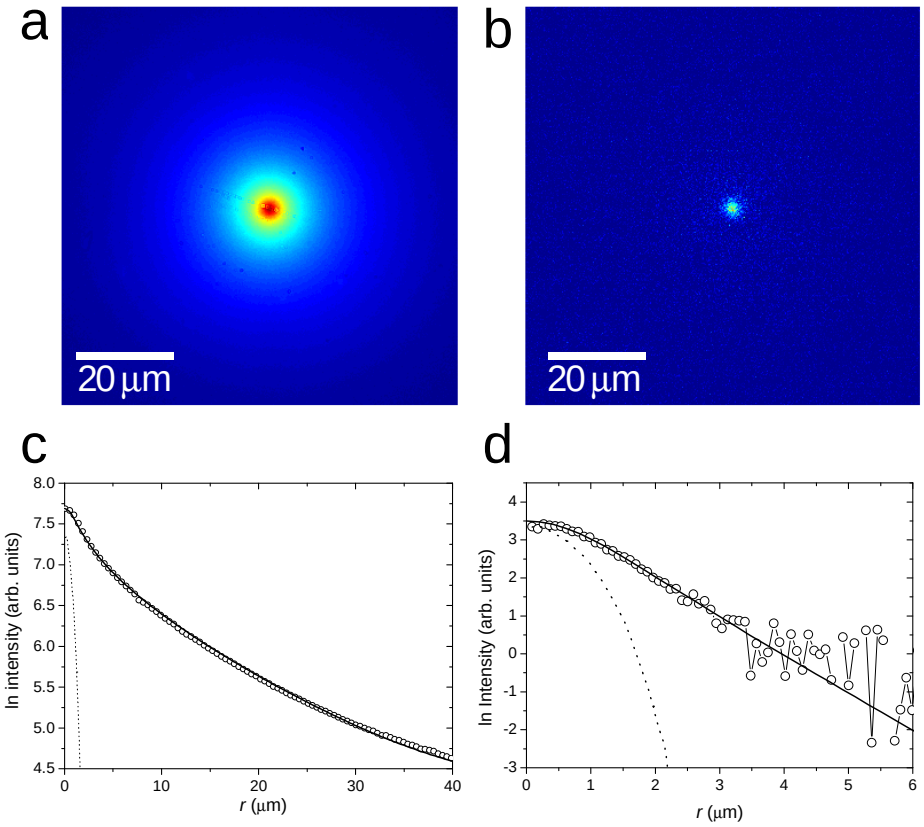


***Fig.7.9:*** *(a) The sum image, $I_s$, obtained on the passivated GaAs patch for a 50 μW excitation focused to a Gaussian spot of half width 0.9 μm. (b) The difference image, $I_d$, obtained under the same conditions. (c) The angular average profile of $I_s$ plotted against r (open circles). The laser excitation profile is also shown (dotted line). The solid line is obtained by convolving the excitation function with a Bessel function $K_0(r/L)$ with L = 21.3 μm. (d) $L_s$ is obtained by fitting the angular averaged profile of $I_d$ (open circles) with a numerical solution of Eq. (1b) with $L_s$ = 1.2 μm. Note that the lateral extent of laser excitation profile (dotted line) is smaller than the profile and so does not limit the measurement of $L_s$.*

The PL spectra obtained at the centre of these images are shown in Fig. 7.10. The sum spectrum shows both band-to-band and band-to-acceptor components for the GaAs PL at intensities well above the remnant laser line (not visible on this scale). Indeed the laser intensity at the centre of the PL image is more than a factor of 1000 weaker than the PL intensity, and drops off even further at large distances from the spot centre. The difference spectrum shows a small and negligible laser component since the laser is strongly polarised. The ratio of the *integrated* difference spectra and of the *integrated* sum spectra between 1.4 eV and 1.5 eV yields a polarisation of 0.8 % in reasonable agreement with that obtained at the centre of the difference to sum profiles in Figs. 7.9c and 7.9d (1.2 %). In addition to confirming that the images in Fig. 7.9 contain no significant contribution from the laser, the

spectrometer is also useful in measuring the local sample temperature. In the experiments reported here heating is negligible.

We now examine the shapes of the luminescence and polarisation spatial decays in more detail. As shown in Eq. (A.29), if $L >> \ell$, the diffusion is two dimensional and one has $n_+ + n \approx K_0(r/L)$, using a modified Bessel function of the second kind. The solid black curve in Fig. 7.9c is obtained using a convolution of $K_0(r/L)$ with the shape of the laser spot. Here the only fitting parameter is $L$. For $L$ = 21.3 μm, the fit perfectly accounts for the data. This value is less than a factor of 2 larger than the approximate estimate of Appendix C. Note that for $r >> L$ the function $K_0(r/L)$ becomes exp $(r/L)$. However, since the data only extend out to about $r$ = 50 μm, the exponential behavior is not clearly observed.

For $I_d$ (Fig. 7.9d) the decay with $r$ is far more rapid, reflecting the fact that $\tau_s << \tau$ and thus $L_s = \sqrt{D_s \tau} << L$. Note however that the lateral extent of the laser (dotted curve) is still inferior to that of the difference signal meaning that the laser spot size does not limit the measurement of $L_s$. It is no longer possible to fit a convolved Bessel function to this data since the lateral extent of the spot is comparable to $\ell$ and the diffusion is therefore only quasi-2D. Therefore Eq. (A4) has been solved numerically using a commercial finite element method. For $L_s$ = 1.2 μm, the solid black curve in Fig. 7.9d is obtained, in excellent agreement with the data. This quantity is the *intrinsic* spin diffusion length and is quite comparable to the estimate of 1.4 μm given in Table 6.3 for a similar doping.

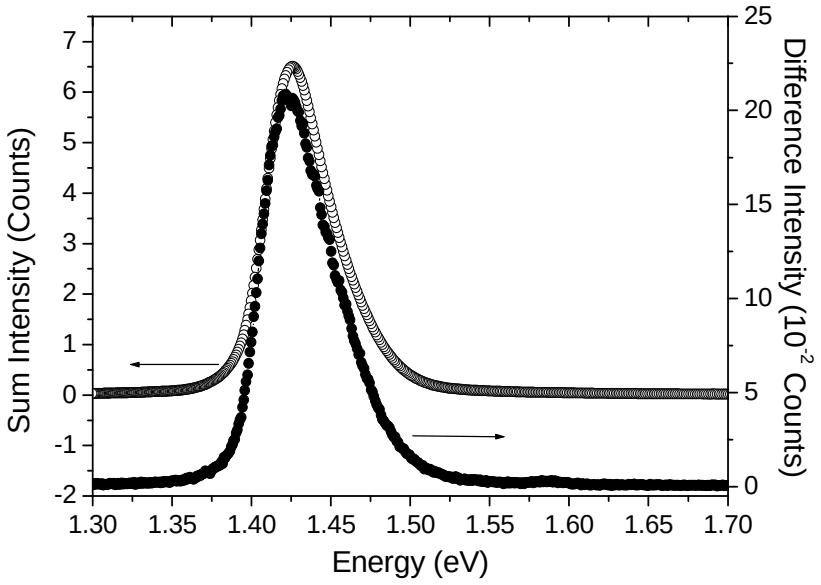


***Fig.7.10:*** *Sum (open circles) and difference (closed circles) spectra obtained on the passivated sample at the center of the PL images $I_s$ and $I_d$ respectively. The spectrally averaged polarisation between 1.4 eV and 1.5 eV is in good agreement with that measured at center of the images in Fig.7.9. The inset shows a white light image of the GaAs patch on SiC with the laser spot close to the center.*

Finally, according to Eq. (7.5), the spatially averaged polarisation <*P*> should be $< P >= P_i \frac{\tau_s}{\tau} = P_i \left( \frac{L_s}{L} \right)^2 = 0.11\%$ using the measured values of $L$ and $L_s$. Taking account of a slight depolarisation of the laser in the objective, (70 % rate of circular polarisation) the polarisation calculated from the spatial averages of $I_d$ and $I_s$ (Figs. 7.9 (a) and 7.9 (b)) is <*P*> = 0.16 %. The intrinsic values obtained for $L$ and $L_s$ are thus in very good agreement with the spatially-averaged luminescence polarisation.

It is interesting to note that the polarisation ($P_c \approx 3\%$) at the centre of the image is much larger than <*P*>. This is the result of carrier diffusion that reduces the residence time at the spot centre (i.e. the lifetime at the center) to $1/\tau^* = 1/\tau + D_e/l^2$ where $l$ is the extension of the laser spot. Since $\tau \sim 10$ ns and $D_e \sim 2.5 \times 10^9$ μm$^2$/s for GaAs of this doping level, $\tau^* \sim \tau/30$ one finds $P_c \sim 30 <P>$ as observed.

## *V. Naturally oxidised sample*

The same experiment is carried out on the oxidised sample, with the angular averaged profiles for $I_s$ and $I_d$ shown in Figs. 7.11 (a) and 7.11 (b) respectively (open circles). In both cases the lateral extent of the PL is now comparable with $d$ but still larger than $w$ (dotted line). Consequently, numerical resolution of diffusion and spin diffusion equations [(A.3) and (A.4)] is again required as both the charge and spin diffusion are only quasi-2D.

Fixing $L$ and $L_s$ at their intrinsic values obtained on the passivated sample, and using $S = 10^7$ cm/s in the boundary conditions, the solid curves with closed circles are obtained. The similarity between these curves and those obtained with effective diffusion lengths, as well as with the data, clearly demonstrate that surface recombination is primarily responsible for the sharp reductions in both $L$ and $L_s$. The difference in doping densities of the two samples plays only a secondary role.

It is also possible to estimate *effective* diffusion and spin diffusion lengths by taking a small recombination velocity and by taking account of surface recombination by an effective lifetime $\tau_e$ ff and therefore effective values of diffusion length $L_{eff}$ and spin diffusion length $L_{s,eff}$. One finds $L_{eff} = 1.3$ μm and $L_{s,eff} = 0.8$ μm (see solid curves in Figs.7.11 (a) and 7.11(b)). Using a 2D approach, Eq. (A.38) predicts $L_{eff} = L_{s,eff} \approx \ell/\pi \sim 0.95$ μm which is in satisfactory agreement with the measured values. With these values, and using Eq. (7.5), <*P*> = 15 % is expected, which compares favourably with the value obtained from the ratio the integrated intensities of $I_d$ to $I_s$ (12.1 %).

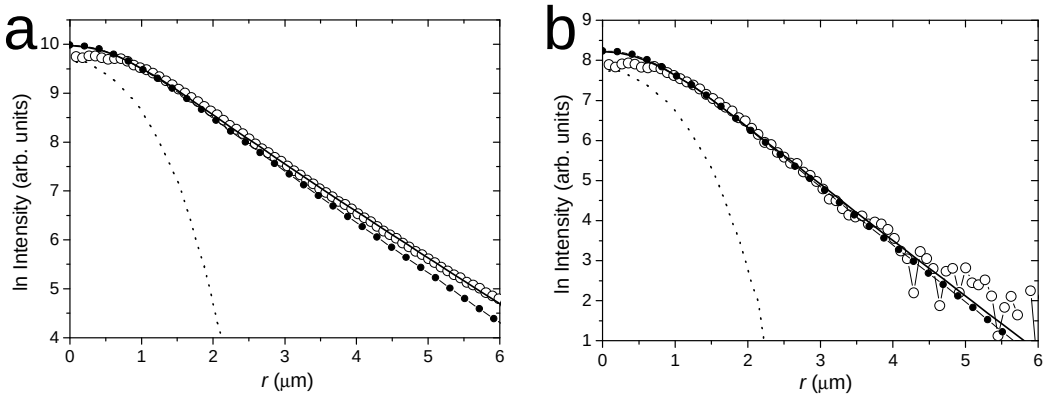


***Fig. 7.11:*** *(a) Angular averaged profile of $I_s$ obtained on the naturally oxidized sample (open circles). A numerical resolution of Eq. (A.3) with $S = 10^3$ cm/s and $L_{eff} = 1.3$ μm yields the solid line. Close agreement is obtained (closed circles) with the curve corresponding to a fixed value of L (= 21.3 μm, the intrinsic value measured on the passivated sample) and $S = 10^7$ cm/s. This demonstrates that the sharp reduction in the effective charge diffusion length is due to increased surface recombination. (b) The same is true for $I_d$ where $L_{s,eff}$ is reduced to 0.8 μm. In both cases the lateral extent of the laser (dotted lines) is smaller than that of the luminescence profile.*

## *VI. Conclusion and perspectives*

The effective values of the diffusion and spin diffusion lengths obtained here are summarised in Table 7.1. The fact that these values strongly depend on surface recombination proves that bulk quantities are only accessible for passivated surfaces.

| ***Sample*** | ***Doping*** ($cm^{-3}$) | ***L (μm)*** | ***$L_s$ (μm)*** |
|---|---|---|---|
| **Passivated** | $1.5 \times 10^{17}$ | 21.3 | 1.2 |
| **oxidised** | $10^{18}$ | 1.3 | 0.8 |

***Table 7.1:*** *Measured charge and spin diffusion lengths for passivated and naturally oxidized GaAs thin films.*

The present technique can, more generally be used to investigate:

-Charge and spin transport as a function of temperature and doping.

-Precession effects in transverse magnetic fields (Hanle effect). This would permit the experimental determination of the minority carrier lifetime and the spin lifetime. Combined with the diffusion lengths, a simple determination of the charge ($D = L^2/\tau$) and spin ($D_s = L_s^2/\tau_s$) diffusion coefficients is then possible. Investigations of the recently reported "spin drag" phenomena[128] (in which $D \neq D_s$) would then be possible.

-The effect on spin diffusion of the electrostatic coupling with holes (ambipolar spin diffusion).

-Spin transport by combining optical injection with electrical detection. This would permit the investigation of materials other than GaAs deposited onto a GaAs substrate.

-Investigating optical pumping in Silicon.

[128] *J. M. Kikkawa and D. D. Awschalom, Nature, **397**, 139 (1999)*

# Chapter 8: Conclusion and future work

Among the work of presented in this thesis, there are four principal results:

-Charge injection into nonmagnetic surfaces has been investigated and analysed using a new model which described photoassisted tunnelling from an optically pumped semiconductor into a metallic surface. At large tunnel distances the exponential variation in the tunnel photocurrent with applied bias dependence results from a bias dependent tunnel barrier height. At small distances the variation is due to bias induced changes in the surface recombination velocity.

-Spin dependent tunnel injection into magnetic metals from an optically pumped semiconductor has been tentatively observed and modelled using an extension of the model developed for charge injection. Spin asymmetries in the tunnel photocurrent up to 6 % are measured which compares with less than 0.1 % observed on (nonmagnetic) Gold surfaces. A slight decrease in the asymmetry with increasing bias has been interpreted as being due to the decrease of the photoelectron spin polarisation caused by the decrease of surface recombination velocity.

-GaAs tip spin injectors fabricated on transparent III-V cantilevers have been investigated by measuring their optical properties using microluminescence. Desirable features of future optimised spin injectors have been suggested and discussed.

-Imaging of charge and spin transport has been developed, using a novel luminescence microscopy technique, simpler than other imaging techniques used in the past. Here it was used to measure the effect of an increase in surface recombination velocity from $10^3$ cm/s to $10^7$ cm/s on the charge and spin diffusion lengths. A reduction from 21 μm to 1.3 μm and from 1.2 μm to 0.8 μm is observed, respectively. The implications of the strong decrease in diffusion length for devices with free, oxidized surfaces (such as tip injectors) are discussed.

The results obtained here on tunnelling charge and spin injection open up a number of possibilities for imaging and spectroscopy of nanomagnetism. Currently a number of groups worldwide have succeeded in measuring atomically resolved images of magnetism using ferromagnetic tip scanning tunnelling microscopy. Imaging with an optically pumped GaAs tip has a number of potential advantages over the existing method; since the spin density in the GaAs is small there is no magnetic interaction between the tip and surface meaning that soft magnetic materials can be imaged. Optical components can be used to switch the polarisation of the photoelectrons in the GaAs far more rapidly than is possible with

ferromagnetic tip whose magnetisation must be reversed by an external magnetic field. This can be used to advantage to simply separate the magnetic and topological dependence of the tunnel current.

There are a number of issues to overcome before spin polarised scanning tunnelling microscopy and spectroscopy can be attempted with optically pumped GaAs tips. In Chapter 5 it was shown that the bias dependence of the spin dependent tunnel effect is not related to the spectroscopy of the metal density of states but rather depends on the bias dependence of the photoelectron spin polarisation. In order to obtain spectroscopic information on the magnetic band structure by varying the bias, it is necessary to increase the tunnel distance so that the surface recombination velocity only weakly depends on bias. Secondly, while the investigation of injection into cobalt and gold surfaces has been possible despite the observed instabilities, these instabilities are expected to be larger for injection from a GaAs tip because of the small contact area. Improvement of the stability will be important to obtain reliable images of nanomagnetism. Potential solutions to these challenges may include:

- tunnelling in ultra-high vacuum using atomically clean tips and surfaces
- tunnelling in electrochemical conditions on in-situ prepared magnetic surfaces
- tunnelling on ex-situ prepared magnetic surfaces in a protective hydrophobic liquid with chemically passivated tip and magnetic surfaces. Our group has already developed novel chemical passivation methods for GaAs surfaces.[129] This option most closely resembles the conditions under which the results were obtained here.

It would also be interesting for quantitative investigations to measure the spin polarisation of injected electrons. To this end one can think of injecting the electrons into a p-type semiconducting surface whose resulting band-to-band cathodoluminescence polarisation can be measured. This semiconductor must have a bandgap larger than that of GaAs in order not to be directly excited by the laser light. Another possibility would be to inject high energy electrons (up to 1 keV) from the cantilever into a substrate on which a magnetic layer acting as a spin filter is evaporated and to measure the asymmetry of the current detected in the substrate after ballistic transport across the metal. This experiment is similar to others performed in our group, but gives in addition the possibility for spatial imaging.[130] Since the energy of electrons is larger than the vacuum level these experiments should not be affected by the surface chemistry.

[129] *V.L. Berkovits, D. Paget, A.N. Karpenko, V.P. Ulin, and O.E. Tereshchenko, Appl. Phys. Lett.* ***90****, 022104 (2007)*
[130] *N. Rougemaille, D. Lamine, G. Lampel, Y. Lassailly, and J. Peretti, Phys. Rev. B* ***77****, 094409 (2008)*

# Appendix A: Charge and spin diffusion of electrons in GaAs

Since charge and spin diffusion plays a role in several chapters of this thesis, I have summarized here the main notions on these diffusions, relying on the diffusion equations which define the concentrations $n_{\pm}$ of electrons of spin ±1/2 at equilibrium. The general case of three-dimensional charge and spin diffusion is considered in Chapter 6 for diffusion in a GaAs tip and in Chapter 7 for diffusion in a thin GaAs film of thickness comparable to the diffusion length. Under circularly-polarised light, the charge diffusion equation is

$$(g_+ + g_-)\varphi(x,y)\alpha e^{-\alpha z} - \frac{(n_+ + n_-)}{\tau} + D\Delta(n_+ + n_-) = 0 \qquad \text{(A.1)}$$

where z is the direction of light excitation. The first term describes creation of photelectrons by light absorption. Here $\alpha$ is the absorption coefficient at the energy of excitation, $\varphi(x,y)$ describes the lateral dependence of the light excitation intensity, and $g_{\pm}$, proportional to the light excitation power, define the respective creation rates of + or – electronic spins. The second term, where $\tau$ is the *bulk* photo-electron lifetime, describes losses of photoelectrons by recombination. The third term, where *D* is the diffusion constant and $\Delta$ is the Laplacian operator, describes the diffusion of charge. The similar equation for the difference $n_+ - n_-$ is

$$(g_+ - g_-)\varphi(x,y)\alpha e^{-\alpha z} - \frac{(n_+ - n_-)}{\tau_s} + D\Delta(n_+ - n_-) = 0 \qquad \text{(A.2)}$$

Here $\tau_s$ is the overall spin lifetime, given by $\tau_s = (1/\tau + 1/T_1)^{-1}$, where $T_1$ is the spin-lattice relaxation time. The quantities $g_+$ and $g_-$ are such that the initial polarisation $\frac{g_+ - g_-}{g_+ + g_-}$ is equal to $\pm 0.5$ for a $\sigma^{\mp}$ helicity of the incident light. These equations can also be written

$$(g_+ + g_-)\tau\varphi(x,y)\alpha e^{-\alpha z} - (n_+ + n_-) + L^2\Delta(n_+ + n_-) = 0 \qquad \text{(A.3)}$$

$$(g_+ - g_-)\tau_s\varphi(x,y)\alpha e^{-\alpha z} - (n_+ - n_-) + L_s^2 D\Delta(n_+ - n_-) = 0 \qquad \text{(A.4)}$$

where the diffusion length and the spin diffusion length are defined respectively by

$$L = \sqrt{D\tau} \qquad L_s = \sqrt{D\tau_s} \qquad \text{(A.5)}$$

These equations are solved using the surface boundary conditions

$$-D\frac{\partial(n_+ \pm n_-)}{\partial\vec{u}} = S(n_+ \pm n_-).\vec{u} \qquad \text{(A.6)}$$

where $\vec{u}$ is the surface normal and *S* is the surface recombination velocity.

Here the charge and spin diffusion are considered using a unipolar approximation[131] in which the hole diffusion does not slow down the electron and spin diffusion. Such approximation is valid for sufficiently small values of the electron concentrations, and will be considered here. As a result the diffusion constants are considered as independent on the electronic and hole charges.

In this thesis, apart from chapter 7, charge and spin diffusion play a role in three situations of reduced dimensionality which I describe here separately.

## *I. One dimensional charge diffusion across a GaAs film (Chapter 2)*

We consider here charge and spin diffusion after creation at the rear of a GaAs film, and before tunnel injection into a metallic or magnetic surface. Because of the one dimensional nature of the system and since the light is focussed to a spot larger than the diffusion length and the thickness of the film, the lateral dimensions do not play a role so that $\varphi(x,y)$=1. The boundary conditions for this diffusion are

$$D\frac{\partial n}{\partial z}\bigg|_0 = S' n_{Z=0} \qquad D\frac{\partial n}{\partial z}\bigg|_{l-W} = -Sn_0 \tag{A.7}$$

Here *S'*, $n_{Z=0}$ and *S*, $n_0$ are the surface recombination velocities and photoelectron concentrations at the rear surface and at the onset of the depletion region, correspondingly. *l* is the thickness of semiconductor film and *W* is the larger of the depletion zone.

In the case of a planar sample of thickness $\ell$ the general solution of Eq. (A.3) is

$$n_+ + n_- = Ae^{-z/L} + Be^{z/L} + \frac{(g_+ + g_-)\alpha\tau}{1-(\alpha L)^2}e^{-\alpha z} \tag{A.8}$$

where A and B, are obtained from the boundary conditions. The concentration at $z=\ell$, which is of particular interest for injection, is

$$(n_+ + n_-)(\ell) = (g_+ + g_-)\, f(L)/(\alpha D) \tag{A.9}$$

where

$$f(L) = \frac{(\alpha L)^2}{(\alpha L)^2 - 1}\,\frac{\mu(SL/D + \alpha L) - \nu(1 + \alpha SL^2/D)}{\frac{(S+S')L}{D}Ch(\ell/L) + (1 + SS'L^2/D^2)Sh(\ell/L)} \tag{A.10}$$

is a positive quantity where *S* is the recombination velocity of the surface under light excitation and *S'* is that of the opposite surface and $\mu$ and $\upsilon$ are given by

$$\mu = 1 - e^{-\alpha\ell}Ch(\ell/L) \qquad \nu = e^{-\alpha\ell}Sh(\ell/L) \tag{A.11}$$

[131] *R. A. Smith, Semiconductors, Second Edition, Cambridge University Press, Cambridge, 1978.*

Thus, the electronic concentration $n_0$ at $z=\ell$ is given by

$$n_0 = \beta\, N_0 \tag{A.12}$$

where

$$\beta = \left(1 + S/v_d\right)^{-1} \tag{A.13}$$

$$N_0 = \frac{g\alpha\tau}{(\alpha L)^2 - 1}\,\frac{\mu\alpha L - \upsilon + (S'L/D)\left[\mu - \upsilon\alpha L\right]}{(S'L/D)Ch(\ell/L) + Sh(\ell/L)} \tag{A.14}$$

and

$$v_d = \frac{D}{L}\,\frac{(S'L/D)Ch(\ell/L) + Sh(\ell/L)}{Ch(\ell/L) + (S'L/D)Sh(\ell/L)} \tag{A.15}$$

For an unpassivated rear surface, one has both $S'L/D >> Th(\ell/L)$ and $S'L/D >> \left[Th(\ell/L)\right]^{-1}$ so that one finds

$$v_d \approx \frac{D}{L}\left[Th(\ell/L)\right]^{-1} \tag{A.16}$$

Further assuming that $\alpha L >> 1$ and neglecting for a large value of $\alpha\ell$ the light absorption at the front surface, so that $\mu \approx 1$ and $\upsilon = 0$, one finds

$$N_0 \approx \frac{g\tau}{LSh(\ell/L)} \tag{A.17}$$

Finally, the photocurrent is given by

$$J_p = qn_0S = q\beta N_0 S \tag{A.18}$$

## *II. One dimensional spin diffusion across a GaAs film*

*II.1 Spin independent surface recombination (Chapter II)*

The spin diffusion equation (A.4) is obtained from the charge diffusion equation (A.3) by replacing $\tau$ by $\tau_s$, and $g_+ + g_-$ by $g_+ - g_-$. The treatment of the preceding section can be repeated for the spin to define the spin quantities for $N_{os}$, $\beta_s$ and $v_{ds}$ equivalent to $N_o$, $\beta$ and $v_d$ respectively. Assuming first that the surface recombination velocity does not depend on spin, the quantity $(n_+ - n_-)(\ell)$ is given by

$$(n_+ - n_-)(\ell) = (g_+ - g_-)\, f(L_s)/\alpha D \tag{A.19}$$

and the spin polarisation of the injected electrons is equal to $P_i\, f(L_s)/f(L)$. Assuming that the two sides of the film have infinite recombination velocities (both larger than $D/L$, $D/L_s$ and $\alpha D$), one finds

$$f(L) \approx \frac{(\alpha L)^2}{(\alpha L)^2 - 1} \quad \frac{\mu - \nu\alpha L}{Sh(\ell / L)} \tag{A.20}$$

Shown in Fig. A.1 is the dependence of $f(L)$ as a function of $L$, normalized to unity for large values of $L$. Here $\ell$ is taken as the unit length. The three Curves correspond to three values of the absorption coefficient, respectively such that $\alpha\ell$ <<1, $\alpha\ell$ =1, and $\alpha\ell$ >>1. $f$ is an increasing function of $L$, a fact which is also true for arbitrary values of the surface recombination velocities. Since $L_s$<$L$, this implies that polarisation value is smaller than $P_i$. It is seen in Curve c, for which $\alpha\ell$ <<1, that $f(L)$ increases nearly linearly with $L$ up to about $\ell/3$. In this case $\left[(n_+ - n_-)/(n_+ - n_-)\right](\ell) = 0.5L_s / L \approx 0.5\sqrt{\tau_s / \tau}$ . This result is not true for larger values of $\alpha$ but the polarisation value is not strongly dependent on $\alpha$. Finally, for $L$ and $L_s$ larger than about $\ell$, $f(L)$ weakly depends on $L$ so that the polarisation is close to $P_i$. It is concluded that, in the limit case of large recombination velocities and diffusion lengths, the injected electrons have a polarisation close to the initial polarisation 50%, i. e. much larger than given by Eq. (1.1).

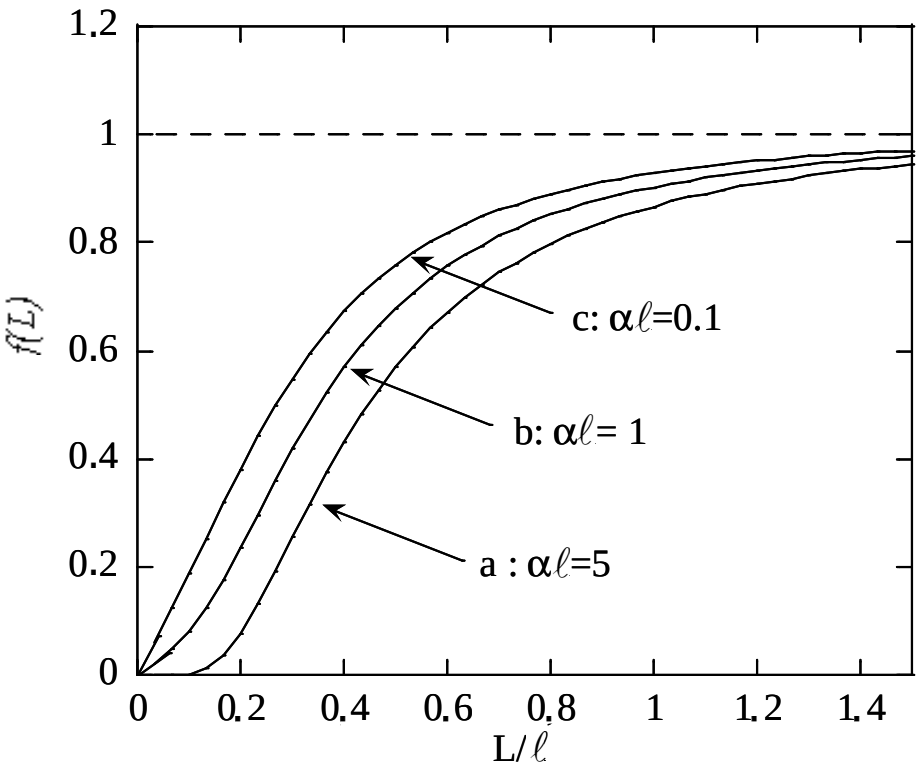


***Fig A.1:*** *Variation of the function f(L) defined by Eq. (A20), for several values of the absorption coefficient. The spin polarisation in the plane of injection is equal to 0.5 $f(L_s)/f(L)$. The unit length is the thickness $\ell$ of the film.*

*II.2 Spin-dependent surface recombination (Chapter II)*

As seen in Chapter 2, because of the distinct positions of the quasi Fermi levels for spins + and –, the values of the recombination velocities for the two spins differ, so that the boundary condition for the spin diffusion equation at the surface of tunnel injection becomes

$$D\frac{\partial(n_{\pm})}{\partial z} = -S_{\pm}n_{\pm} \tag{A.21}$$

which gives to first order

$$D\left.\frac{\partial \delta n}{\partial z}\right|_{z=\ell} = -S\delta n - n\delta S/2 \tag{A.22}$$

where $\delta$ denotes the difference between two identical quantities for + and – spins. One obtains, in the same way as in the preceding section

$$\delta n_0 = N_{os}\beta_s - (1-\beta_s)\frac{n_0}{2}\frac{\delta S}{S} \tag{A.23}$$

$$\delta J_p/q = S\delta n_0 = N_{os}\beta_s S - (1-\beta_s)\frac{n_0}{2}\delta S \tag{A.24}$$

Here

$$\beta_s = (1+S/v_{ds})^{-1} \tag{A.25}$$

and within the approximation of the preceding subsection

$$v_{ds} \approx \frac{D}{L}\left[Th(\ell/L)\right]^{-1} \tag{A.26}$$

$$N_{0s} \approx \frac{(g_+ - g_-)\tau_s}{L_s Sh(\ell/L_s)} \tag{A.27}$$

So that

$$\frac{N_{0s}}{N_0} \approx \frac{(g_+ - g_-)}{(g_+ + g_-)}\sqrt{\frac{\tau_s}{\tau}}\frac{Sh(\ell/L)}{Sh(\ell/L_s)} \tag{A.28}$$

## *III. Lateral diffusion in a GaAs film (Chapter 7)*

We consider here the case where photo-carriers are created in a thin GaAs film by a tightly focussed flux of photons which has a profile $\varphi(x,y)$ in the surface plane. In the general case, calculation of the charge and spin concentration at a given point in the film requires numerical resolution of the diffusion and spin diffusion equations. We discuss here two cases where analytical approaches can be given. These calculations will be performed out

of the zone of light excitation. In this case, the source terms of Eq. (A.3) and (A.4) are zero and these equations are Helmholtz equations of the type $\Psi+k^2\Delta\Psi=0$.[132]

*III.1 planar diffusion*

If the distance *r* to the excitation spot is larger than the film thickness, the general solution is a Bessel function of the complex argument r/ik. The general expression for isotropic solutions, imposing a zero concentration at infinite distance is

$$n_+ + n_- \div K_0(r/L) \tag{A.29}$$

$$n_+ - n_- \div K_0(r/L_s) \tag{A.30}$$

where $K_0$(x) is the modified Bessel function of the second kind. At x>>1 this function can be approximated by an exponential.

*III.2 Separation of the variables*

Considering for illustration purposes the charge diffusion equation, we look for a solution of the type

$$n \approx f_1(r) f_2(z) \tag{A.31}$$

Eq. (A.3) becomes, out of the excitation light spot,

$$\frac{1}{rf_1(r)}\frac{\partial}{\partial r}\left(r\frac{\partial f_1(r)}{\partial r}\right)+\frac{\partial^2 f_2(z)}{f_2(z)\partial z^2}-\frac{1}{L^2}=0 \tag{A.32}$$

which can only be fulfilled if the first and second terms, which depend on distinct variables, are separately constant, of the form

$$\frac{1}{rf_1(r)}\frac{\partial}{\partial r}\left(r\frac{\partial f_1(r)}{\partial r}\right)=\frac{1}{L^2}+\varpi^2 \tag{A.33}$$

$$\frac{\partial^2 f_2(z)}{f_2(z)\partial z^2}=-\varpi^2 \tag{A.34}$$

where $\varpi^{-1}$ is a length, determined by the boundary conditions, and given by

$$\varpi L tg\left(\varpi\frac{\ell}{2}\right)=\frac{SL}{D} \tag{A.35}$$

The solution of Eq. (A.34) is

$$f_2(z)=\cos(\varpi z) \tag{A.36}$$

Finally, the function $f_1(r)$ is the solution of a 2 dimensional Helmholtz equation, given by Eq. (A.29), where the diffusion length *L* is replaced by its effective value $L_{eff}$

[132] *E. Belorizky, « Outils mathématiques » Chapter 10, Grenoble Sciences, (2006)*

$$\frac{1}{L_{eff}^2} = \frac{1}{L^2} + \varpi^2 \qquad \text{(A.37)}$$

While $L$ is a bulk quantity, $L_{eff}$ depends on the surface recombination velocity via Eq. (A.35). In the extreme case of a passivated film, for which $\varpi\ell << 1$, one finds in agreement with standard models that the surface recombination is equivalent to a bulk recombination time $\ell/2S$.[133]

$$\frac{D}{L_{eff}^2} = \frac{1}{\tau} + 2S/\ell \qquad \text{(A.37)}$$

In the opposite case of an unpassivated film, Eq. (A.34) can only be fulfilled for $\varpi\ell \approx \pi$, so that

$$\frac{1}{L_{eff}^2} = \frac{1}{L^2} + \frac{\pi^2}{\ell^2} \approx \frac{\pi^2}{\ell^2} \qquad \text{(A.38)}$$

The hypothesis of separability of the variables, illustrated by Eq. (A.30), is a strong hypothesis. It implies that when the distance to the centre increases, the distribution of carriers as a function of depth does not change its shape but only its overall magnitude. Its validity has been verified for the case of Chapter 7 using a numerical resolution of the diffusion equation.

[133] *R. Ahrenkiel, Minority Carrier lifetime in III-V Semiconductors, vol. 39, Semiconductors and Semimetals, Academic Press (1993)*

# Appendix B: Charge and spin recombination currents

The calculation of the charge recombination velocity via midgap states leads to the expression of the surface recombination current used in Eq. (2.34).[134] In this appendix, we recall the principles of the calculation and extend it to the calculation of the spin recombination current. Fig. B1 shows, for near midgap states extending between energies $\varepsilon$ and $\varepsilon+\delta\varepsilon$, the rates of capture and emission events for electrons of $\pm$ spin and holes. Also shown are the spin populations.

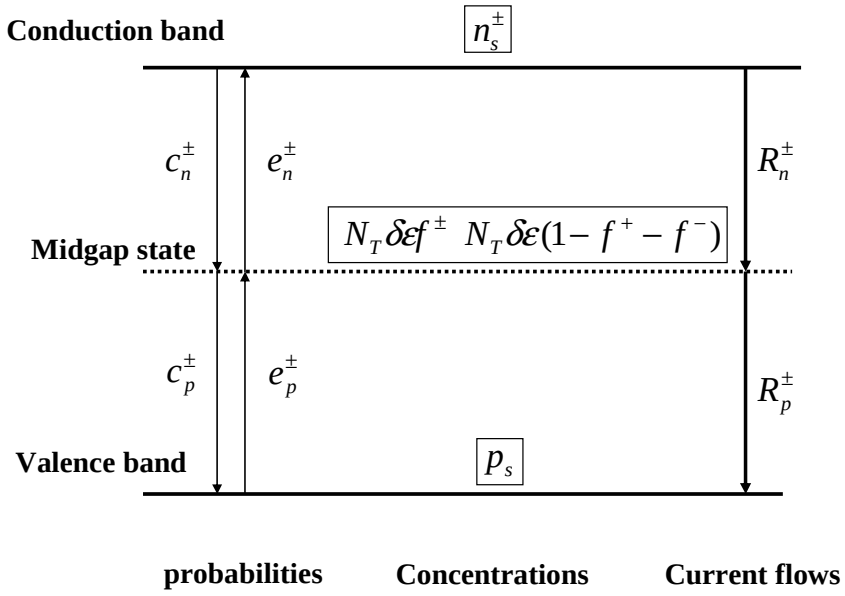


***Fig. B1:*** *Scheme for calculating charge and spin recombination currents*

Defining $\sigma_n$ and $\sigma_p$ as the cross sections for electron and hole recombination at traps, and $v_n$ and $v_p$ as the electron and hole velocities, one has

$$c_n^{\pm} = \sigma_n v_n n_s^{\pm} N_T \delta\varepsilon\left[1-\left(f^{+}+f^{-}\right)\right] \tag{B.1}$$

$$e_n^{\pm} = c'_n N_T \delta\varepsilon f^{\pm} \tag{B.2}$$

At equilibrium, one has

$$f^{+}+f^{-} = f_0 = \frac{1}{1+\exp[(E_T-E_F)/kT]} \tag{B.3}$$

$$n_s^{+}+n_s^{-} = n_0 = N_c \exp[E_C - E_F/kT] \tag{B.4}$$

where $E_F$ is the Fermi energy $E_T$ is the energy of the traps and $N_C$ is the reduced density of states in the conduction band. Since $e_n^{+}+e_n^{-} = c_n^{+}+c_n^{-}$ we obtain

[134] *R. A. Smith, Semiconductors, Second Edition, Cambridge University Press, Cambridge, 1978.*

$$c_n^{'} = \sigma_n v_n n_0 (1 - f_0) / f_0 = \sigma_n v_n n_{ts} \tag{B.5}$$

where

$$n_{ts} = N_c \exp[(E_C - E_T)/kT] \tag{B.6}$$

In the same way, one has

$$c_p^{\pm} = \sigma_p v_p N_T \delta\varepsilon f^{\pm} \tag{B.7}$$

$$e_p^{\pm} = \sigma_p v_p p_{ts} N_T \delta\varepsilon \left[1 - \left(f^{+} + f^{-}\right)\right] \tag{B.8}$$

where, in the same way as in Eq. (B.6),

$$p_{ts} = N_v \exp[(E_T - E_v)/kT] \tag{B.9}$$

The total frequencies of recombination events are given by

$$R_n^{\pm} = c_n^{\pm} - e_n^{\pm} = \sigma_n v_n N_T \delta\varepsilon \left\{\left[1 - \left(f^{+} + f^{-}\right)\right] n_s^{\pm} - f^{\pm} n_{ts}\right\} \tag{B.10}$$

$$R_p^{\pm} = c_p^{\pm} - e_p^{\pm} = \sigma_p v_p N_T \delta\varepsilon \left\{f^{\pm} p_s - \left[1 - \left(f^{+} + f^{-}\right)\right] p_{ts}\right\} \tag{B.11}$$

The expressions of $f^{+}$ and $f^{-}$ are finally obtained by writing, in steady state, the conservation of charge and spin currents

$$[R_n^{+} + R_n^{-}] = [R_p^{+} + R_p^{-}] \tag{B.12}$$

$$[R_n^{+} - R_n^{-}] - [R_p^{+} - R_p^{-}] - \frac{N_T \delta\varepsilon}{T_1^s}\left(f^{+} - f^{-}\right) = 0 \tag{B.13}$$

where $T_{1s}$ is the spin relaxation time of electrons at surface centres. One finds

$$f^{+} + f^{-} = \frac{\sigma_n v_n \left(n_s^{+} + n_s^{-}\right) + \sigma_p v_p p_{ts}}{\sigma_p v_p (p_s + p_{ts}) + \sigma_n v_n \left(n_s^{+} + n_s^{-} + n_{ts}\right)} \tag{B.14}$$

$$f^{+} - f^{-} = \frac{\sigma_n v_n}{\sigma_p v_p p_s + 1/T_1^s} \frac{\left(\sigma_n v_n n_{ts} + \sigma_p v_p p\right)\left(n_s^{+} - n_s^{-}\right) - \left(\sigma_n v_n n_{ts} + \sigma_p v_p p_{ts}\right) n_{ts}}{\sigma_p v_p (p_s + p_{ts}) + \sigma_n v_n \left(n_s^{+} + n_s^{-} + n_{ts}\right)} \tag{B.15}$$

$$R_n^{+} + R_n^{-} = R_p^{+} + R_p^{-} = \frac{\sigma_n v_n \sigma_p v_p \left[\left(n_s^{+} + n_s^{-}\right) p_s - n_{ts} p_{ts}\right]}{\sigma_p v_p (p_s + p_{ts}) + \sigma_n v_n \left(n_s^{+} + n_s^{-} + n_{ts}\right)} \tag{B.16}$$

After integration over surface states situated between the hole and electron quasi Fermi levels at the surface, and taking account of $n_{ts} p_{ts} = n_i^2$ where $n_i$ is the intrinsic electron concentration, Eq. (B.16) gives the usual Stevenson-Keyes expression for the surface recombination velocity.[135] The expressions for $R_n^{+} - R_n^{-}$ and $R_p^{+} - R_p^{-}$ are not given here since they will not be used. Eq. (B.14-B.16) can be simplified by assuming, as is generally performed[135] that

[135] *C. H. Henry, R. A. Logan, and F. R. Merritt, J. Appl. Phys.* ***49****, 3530 , (1978)*

$$n_{ts} << \left(n_s^+ + n_s^-\right)$$

$$p_{ts} << p_s$$

$$\sigma_p v_p p_s << \sigma_n v_n \left(n_s^+ + n_s^-\right)$$

One finds, using $P_s = \frac{n_s^+ - n_s^-}{n_s^+ + n_s^-} = \frac{\delta n_s}{n_s}$,

$$\boxed{R_n^+ + R_n^- = R_p^+ + R_p^- \approx \sigma_p v_p \left[n_s p_s - n_i^2\right] n_s^{-1}}$$

$$f^+ + f^- \approx 1 \tag{B.17}$$

$$f^+ - f^- \approx \frac{\sigma_p v_p p_s}{\sigma_p v_p p_s + 1/T_1^s} P_s + \frac{\sigma_n v_n n_{ts}}{\sigma_p v_p p_s + 1/T_1^s}(1 - P_s) \tag{B.18}$$

Assuming finally that

$$\sigma_p v_p p_s >> \sigma_n v_n n_{ts} \tag{B.19}$$

One finds

$$f^+ - f^- \approx \frac{\sigma_p v_p p_s}{\sigma_p v_p p_s + 1/T_1^s} P_s \tag{B.20}$$

# Appendix C: Values of parameters used in the calculations

*C.1 Diffusion constant, diffusion length, surface recombination and diffusion velocity*

The electron mobility $\mu_e$ is found from Ref. (136). The diffusion constant D is obtained using the Einstein relation. The bulk electron lifetime $\tau$ is found using Ref. (137). We then obtain the diffusion length $L = \sqrt{D\tau}$. The surface recombination velocity has been estimated in Ref. (138) and is of the order of the thermal velocity $10^5$ m/sec. The values of these quantities for several acceptor doping levels $N_A$ are given in Table C.1 below.

| ***Doping level $N_A$ ($m^{-3}$)*** | ***Mobility $\mu_e$ ($m^2$/Vsec)*** | ***Diffusion constant D ($m^2$/sec)*** | ***Electron lifetime $\tau$ (nsec)*** | ***Diffusion length L (μm)*** | ***Surface recombination velocity (m/s)*** |
|---|---|---|---|---|---|
| $10^{23}$ | 0.3 | 75 x$10^{-4}$ | 19 | 11.9 | 5x$10^4$ |
| $10^{24}$ | 0.15 | 37 x$10^{-4}$ | 2.6 | 3.1 | 7x$10^4$ |
| $10^{25}$ | 0.1 | 25 x$10^{-4}$ | 0.6 | 1.2 | $10^5$ |

***Table C.1****: Values of bulk parameters for GaAs as a function of doping level.*

From these values and using a film thickness of $\ell = 3\mu m$, we calculate a diffusion velocity $v_d$, given by Eq. (A.15) of 1.6 x $10^3$ m/sec for $N_A$ =$10^{24}$ $m^{-3}$.

*C.2 Density and distribution of midgap surface states*

The energy dependence $D(\Delta\varphi)$ of the density of surface states will be approximated by a Gaussian profile of width $\sigma$, estimated to 0.20 eV.[139] A parabolic shape will be taken in order to model the tails of the conduction and valence band densities of states. The resulting normalised shape is shown in Fig .C1. The density of surface states at midgap $N_T(0)$ has been found of several $10^{17}eV^{-1}m^{-2}$ or larger than $10^{18}eV^{-1}m^{-2}$.[139, 140] The analysis in Chapters 4 and 5 will use $N_T(0)$ =6x$10^{18}eV^{-1}m^{-2}$.

[136] *J. R. Lowney and H. S. Bennett, J. Appl. Phys.* ***69****, 7102 (1991)*
[137] *R. J. Nelson and R. G. Sobers, Appl. Phys.* ***49****, 6103 (1978)*
[138] *H. Ito, and T. Ishibashi, Jpn. J. Appl. Phys.* ***33****, 88 (1994)*
[139] *Ş. Karataş, and Ş. Altındal, Mat. Sci and Eng.* ***B 122****, 133 (2005)*
[140] *E. W. Kreutz, Phys. Stat. Sol.* ***56****, 687 (1979)*

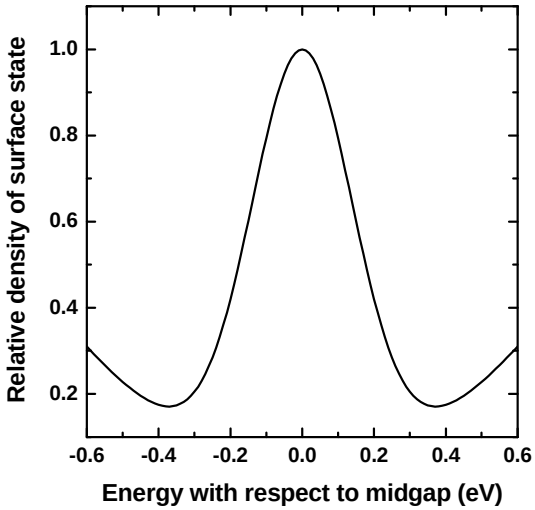


***Fig C.1:*** *Shape of the density of surface states taken in the models.*

*C.3 Work functions (gold, cobalt, cobalt covered by CO, GaAs)*

The work functions for clean gold and cobalt surfaces are 5.1 eV and 5 eV.

Adsorption of carbon monoxide on Co is known to increase the work function to about 6 eV.[141]

The affinity of GaAs depends on the surface stoichiometry and chemistry. We shall take a standard value of 4 eV.

Note that the work function or conduction band position as well as the effective mass crucially depend on the presence or absence of a surface oxide,[142] which can modify the values of the work function. However, the calculated currents depend on the square root of the work function and should not be strongly affected by this uncertainty.

*C.4 Value of $N_0$*

$N_0$ is given by Eq. (A.14). Taking an absorption coefficient $\alpha = 10^4 \text{cm}^{-1}$, an excitation light power of 5mW focussed to a diameter of 20µm, and using the above values of diffusion length and surface recombination velocity for $N_A = 10^{18}$ cm$^{-3}$, we find $N_0 = 2\text{x}10^{22}$ m$^{-3}$.

*C.5 Other parameters*

The dielectric constant of GaAs is equal to 12. The calculated saturation current $J_0 = A^{**}T^2 \exp(-\varphi_0 / kT)$ using the average effective mass of holes in GaAs is $6\text{x}10^{10}$ A/m$^2$.[143]

[141] *S. Ishi, Y. Ohno and B. Vuswanathan, Surf. Sci* ***161****, 349 (1985)*
[142] *T. S. Lay, M. Hong, J. Kwo, J. P. Mannaerts, W. H. Hung, D. J. Huang Sol. State Electron.* ***45****, 1679 (2001)*
[143] *E. H. Rhoderick "Metal-semiconductor contacts " Clarendon (Oxford) 1978.*